Doctoral Dissertation
Doctoral Program in Civil and Environmental Engineering
(34th Cycle)

Modelling of water balance and crop growth based on Earth Observation and re-analysis data

By

Matteo Rolle

******

Supervisor(s):

Prof. Stefania Tamea
Prof. Pierluigi Claps

Doctoral Examination Committee:

Prof. Serena Ceola, Università di Bologna
Prof. Christian Massari, CNR-IRPI Perugia
Prof. Michel Le Page, CESBIO-Université Toulouse III, Paul Sabatier
Prof. Chiara Corbari, Politecnico di Milano
Prof. Roberto Revelli, Politecnico di Torino

Politecnico di Torino
2022

Declaration

I hereby declare that the contents and organization of this dissertation constitute my own original work and does not compromise in any way the rights of third parties, including those relating to the security of personal data.

Matteo Rolle
2022

"Thousands Have Lived Without Love,
Not One Without Water"

Wystan Hugh Auden

ADAM: *"82% of human blood is water… Have the water wars started yet?*
Or is it still about the oil?"
EVE: *"Yeah, they're already starting. "*
ADAM: *"They only figure it out when it's too late, don't they?"*

Jim Jarmusch – Only Lovers Left Alive

"Water is patient, Adelaide. Water just waits.
Wears down the clifftops. The mountains. The whole of the world.
Water always wins."

Doctor Who – The Water of Mars

Acknowledgments

My doctoral years have been like an intense and exciting climb. The trail has not always been straight, but great achievements and interesting challenges also came from adversities. I will remember my PhD activity as the best experiences of the last turbulent, incredible, unpredictable years.

First of all, I would like to acknowledge my supervisors, Prof. Stefania Tamea and Prof. Pierluigi Claps, for sharing with me their unique knowledge and experience. No goal can be achieved without the right guide along the way, and I am hugely grateful for your patience, constant support, enthusiasm and encouragement. I'm glad and honored for the opportunity of this PhD.

I am grateful to Prof. Mehrez Zribi for hosting me three months at the CESBIO research center. This was one of the greatest experiences of my life and a trilling period, full of interesting knowledge and amazing people. Thank you for your kindness and support, and for teaching me so many interesting things about remote sensing.

I also wish to acknowledge the reviewers of this thesis, Prof. Christian Massari and Prof. Serena Ceola, for their precious feedbacks which allowed to strengthen my dissertation.

I would like to thank all the colleagues and friends that I met along the journey. Most of them shared with me joys and sorrows from the beginning of this adventure, I've been very lucky to meet you down the road! Thank you to Marta for all the support she gave me during my first months; to Emna for the unique help and kindness when I was in France; to Melissa, Elisa, Luca, Benedetta, Francesca, Silvia for putting up with me in the office and to all the shiny people from the "BAD" offices.

I'm happy and grateful that even during the most difficult times of my PhD, during the worst months of the pandemic, I had with me the best roommate and friend of the world, who helped me to keep my enthusiasm and serenity. Thank you Simona for the *coinquilini* time!

Special thanks go to my family, who always supported me and which I missed a lot during the difficult separation times due to the pandemic emergency. And I'd like to share all my love to my nephew Leonardo, the *biggest* joy that year 2020 gave to me. I'm trying so hard also for you!

Abstract

Agriculture is not only one of the most ancient economic assets known to man: it also has enormous importance as the most valuable human activity which ensures global food security. Optimal vegetative growth, and therefore crop production, is heavily dependent on the hydro-climatic variables necessary to fulfill the evapotranspirative requirement of plants. According to FAO, more than 1.2 billion people live in regions where water scarcity is a serious threat to agriculture. Therefore, assessment of agricultural water requirements is essential in order to develop effective water-related policies in a globalized world with unprecedented population growth and unevenly distributed water resources. Irrigated areas have almost doubled in the last 50 years and account for 20% of global croplands; they currently consume 70% of freshwater withdrawn for human purposes. Furthermore, rainfed agriculture provides 60% of total food production and is highly dependent on meteorological factors. The assessment of climate-driven changes of crop water requirements and water stress periods is very important in order to highlight future weaknesses of food security. The impact of climate change on food production has become an extremely important issue and is dealt with an increasing number of studies; a cross-sectoral approach must therefore be adopted to effectively address its effect on agriculture, adopting appropriate adaptation strategies across local, regional and global scales.

In recent years, the spread of Earth Observation (EO) data has radically changed the range of technologies currently available to manage agriculture. The possibility to retrieve near real-time information of crop health status and localized criticalities has improved the quality of intensive farming, especially in terms of resource use. Satellites are widely used for the acquisition of large-scale data and modern sensors can reach very high spatial, temporal and spectral resolutions. Nowadays, reanalysis climate datasets offer new possibilities for hydrological modelling, working at relatively high spatio-temporal resolutions.

This thesis aims to exploit the potential of the EO-based data to strengthen the scientific knowledge of how climate variability impacts the water requirements of global agriculture, by (i) developing a model to assess the comprehensive daily crop irrigation requirement (i.e. the ideal input of water needed to avoid water stress); (ii) to assess the climate-driven crop water requirements from 1970 to 2019, highlighting significant trends of irrigation requirements and water stress periods on rainfed croplands; (iii) to combine several satellite measurements to retrieve high-resolution information on actual sowing periods and crop growth, to limit some of the main uncertainties related to crop modelling. In order to achieve this, a hydrological soil-water balance model was developed to model the climate-

driven evapotranspirative requirements using the daily hydro-climatic data from ERA5, the reanalysis dataset provided by the European Centre for Medium-Range Weather Forecasts. The model was tested for year 2000 at the global scale, comparing the modeled irrigation requirements to the national volumes of water withdrawn for irrigation. The analysis was then extended over a 50-year period, highlighting critical issues peculiar to rainfed and irrigated scenarios. In order to improve the quality of crop growth modelling, a synergistic use of optical and radar data from the Sentinel constellation was tested to retrieve information on maize sowing periods and growing phases. The analysis was performed over a densely cultivated pilot area in South Piedmont (Italy).

Results show a good agreement between the estimated irrigation requirements for year 2000 (962 km^3 globally) and national withdrawals for irrigation. A focus on three areas of the world (California, Northern Italy and India) highlights the wealth of information provided by the model in different climatic conditions. Increases of irrigation requirement rates were found on more than 60% of irrigated lands, especially in South Europe, North-East China, West US, Brazil and Australia, where the mean rate increased more than 100 mm/year from 1970s to 2010s. The analysis of rainfed crops highlights statistically significant trends of water stress duration for more than 38% of rainfed croplands, while only 6% were affected by negative trends and shorter stress duration. The satellite-based analysis described in the third part of the thesis highlights the potential of combined optical and radar data to retrieve information of maize growing phases. The actual sowing periods were retrieved for 1154 test fields and results show that most of the maize were sown in late April or in the second half of May in 2019.

This thesis contributes to advancing our knowledge on the impact of climate spatio-temporal variability on agricultural water requirements. The EO-based data is proven to be a valuable instrument (i) for large-scale hydrological modelling, (ii) to describe the global variability of climate-driven impacts on crop water requirements and (iii) to retrieve high-resolution information to improve the accuracy of crop growth monitoring, in order to perform future analyses of actual irrigation practices.

Contents

List of Figures

List of Tables

Acronyms

A	Area
AEI	Area equipped for irrigation
AgMIP	Agricultural Model Intercomparison and Improvement Project
API	Application Programming Interface
AW	Applied Water
AWC	Available Water Capacity
C	Radar band (4 – 8 GHz)
C3S	Copernicus Climate Change Service
CDO	Climate Data Operators
CDWR	California Department of Water Resources
CI	Cropping intensity
CLS	Copernicus Land Service
CRU	Climatic Research Unit (East Anglia University)
CV	Central Valley, California
DEM	Digital Elevation Model
DTM	Digital Terrain Model
E	Irrigation Efficiency
ECMWF	European Centre for Medium-Range Weather Forecasts
EEA	European Environmental Agency
EO	Earth Observation
EP	Emerging period
ERA5	ECMWF Reanalysis 5 climate dataset
ET_0	Reference Evapotranspiration
ET_a	Crop Actual Evapotranspiration
ET_c	Crop maximum evapotranspiration
ET_p	Potential Evapotranspiration
FAO	Food and Agriculture Organization
GDU	Growing Degree Units
GEE	Google Earth Engine platform
GIS	Geographic information system
GS	Growing season
HH	Horizontal-Horizontal radar polarization
HS	Hargreaves-Samani method for the estimation of ET_0

HV	Horizontal-Vertical radar polarization
I	Irrigation requirement
I_{CDWR}	Irrigation requirement estimated by the CDWR
ID	Days requiring irrigation (literally, Irrigation Days)
IEEE	Institute of Electrical and Electronics Engineering
I_{grid}	Mean irrigation requirement considering the entire area of a grid pixel
IPR	Polarimetric Ratio Index
IPR_f	Filtered Polarimetric Ratio Index
IrD	Irrigation Districts
ISPRA	Istituto superiore per la protezione e la ricerca ambientale
ISTAT	Istituto Nazionale di Statistica
k_c	Crop coefficient, defining the ET_c rate
k_{HS}	Hargreaves-Samani empirical coefficient
k_s	Stress coefficient, defining ET_a
L	Radar band (1 - 2 GHz)
lbp	length of the period before plant emergence
LGP	Length of Growing Periods
LSM	Land surface model
NASA	National Aeronautics and Space Administration
NDVI	Normalized Difference Vegetation Index
NIR	Near Infrared
OECD	Organization for Economic Co-operation and Development
P	Precipitation
PD	Precipitation Days
PIE	Potential Irrigation Events
PM	Penman-Monteith
PML	Penman–Monteith–Leuning
PS	Precipitation Surplus
PS_{grid}	Mean precipitation surplus considering the entire area of a grid pixel
PT	Priestley–Taylor
PU	Punjab, India
PV	Po Valley, Italy
R	Pearson correlation coefficient
RED	Red reflectance (visible)
RS-SEB	Remotely sensed surface energy balance
S2MP	Sentinel-1/Sentinel-2-derived Soil Moisture Product
SAR	Synthetic Aperture Radar
SC	Surface conductance
SD	Water stressed days
SDGs	Sustainable Development Goals

SEBM	Surface Energy Balance Model
SM	Soil moisture (satellite product)
SP	Sowing period
SSF	Soil stress factor
SWB	Soil water balance
T_{max}	Maximum Temperature
T_{mean}	Mean temperature
T_{min}	Minimum Temperature
USGS	United States Geological Survey
V	Volumetric irrigation requirement
VH	Vertical-Horizontal radar polarization
VIR	Visual and Infrared imaging
VV	Vertical-Vertical radar polarization
W	Withdrawals for irrigation
wSD	Number of water stressed days normalized by the number of growing days
θ	Soil moisture
θ^*	Soil moisture at incipient water stress
θ_{fc}	Soil moisture at field capacity
θ_{sow}	Soil moisture at the sowing day
θ_w	Soil moisture at wilting point
ρ	Depletion fraction (or depletion factor)

Name list of satellite sensors

Visible and Near Infrared

BGIS-2000	Ball Global Imaging System 2000
ETM+	Enhanced Thematic Mapper +
GIS	GeoEye Imaging System
HRG	Haute Résolution Géométrique
HRV	Haute Résolution dans le Visible
HRVIR	Haute Résolution dans le Visible et l'Infra-Rouge
MODIS	Moderate-resolution Imaging Spectro-radiometer
MS	Multispectral imager
MSC	Multi-Spectral Camera
MSI	Multi-Spectral Imager for Sentinel-2
NAOMI	New AstroSat Optical Modular Instrument
OLI	Operational Land Imager
OSA	Optical Sensor Assembly
PAN	Panchromatic Imager
PMS	Panchromatic and Multi-spectral CCD Camera
SV-110	SpaceView-110 Imaging System
TIRS	Thermal Infra-Red Sensor
VIIRS	Visible/Infrared Imager Radiometer Suite
WV110	World View 110 camera
WV60	World View 60 camera

Radar

AMI-SAR	Active Microwave Instrument - Synthetic Aperture
AMI-SCAT	Active Microwave Instrument - Scatterometer
ASAR	Advanced Synthetic Aperture Radar
ASCAT	Advanced Scatterometer
AVHRR	Advanced Very High-Resolution Radiometer
MIRAS	Microwave Imaging Radiometer using Aperture Synthesis
MWR	Micro-Wave Radiometer
PALSAR	Phased-Array L-band Synthetic Aperture Radar
RA-2	Radar Altimeter - 2
SAR	Synthetic Aperture Radar
SAR-2000	Synthetic Aperture Radar 2000 (X-band)
SMAP	Soil Moisture Active-Passive (intended as payload)

Chapter 1

Introduction

1.1 Background

The management of water resources is strongly linked to food security and sustainable agricultural production. Intensification of scientific studies focusing on the link between water and agriculture proves the importance and the urgency of new ways of conceiving water uses for crop production. A proper understanding of how climate variability impacts the agricultural water consumption is a main challenge in a globalized world. Food production is pushed to meet the needs of a growing population and the international trade network will probably require future large-scale policies and planning.

Agriculture requires more freshwater than any other human activity, consuming about 70% of the resource at the global scale [1]. The management of irrigated croplands is very important for the global food chain, since these areas provide 40% of agricultural products, accounting for only 20% of total cultivated areas [2]. Moreover, the rainfed agriculture ensures 60% of agricultural productions despite being strongly dependent on rainfall water. Ensuring the availability of irrigation water is a primary concern for the future of humanity, as a part of the comprehensive set of adaptation strategies to climate change. The difficulty of finding a balance between the increasing needs for food production, threats due to water availability and other human needs is one of the most important challenges of this century [3].

The Sustainable Development Goals (SDGs) from the Agenda 2030, adopted by the United Nations, recognize the achievement of food security through a sustainable agriculture as a primary target [4]. The 6th SDG highlights the need for a sustainable management of water resources for the global economic growth and productivity [5]. Given the importance of irrigation in the comprehensive use of withdrawn water, agriculture requires specific studies for the improvement of the knowledge and the techniques for the optimization of water uses.

The crop water requirement (or crop water need) is defined in this thesis as the amount of water (in terms of water depth per unit of area) needed by crops to meet the water loss through evapotranspiration, i.e. the amount of water needed by the

plants to grow optimally [6]. More specifically, evapotranspiration is a process whereby a vegetated surface (e.g., a crop field) converts liquid water from soil to water vapour, combining the evaporation and the transpiration processes [7]. The evaporation process is mainly driven by the solar radiative forcing and air parameters like temperature, air humidity and wind speed. Transpiration is the biological process through which plants vaporize liquid water contained through stomata, and release vapour from their leaves into the air. The combined effect of evaporation and transpiration reduces the amount of water in the soil and is an important output in the hydrological soil water balance. Evapotranspiration is also an important variable for the food production chain since optimal agricultural productions depend on the crops ability to withstand water stresses. In fact, after reaching specific moisture deficits, plants start to suffer the lack of available water for their biological processes. This stress condition entails a reduction in the crop yield, causing lower agricultural productions. Irrigation is the most widely used tool in the history of man to fill these water shortages and increase food production.

Several crop models were developed in the last decades to describe the crop yield and the food production as function of climate variability and technological improvements. The AgMIP (Agricultural Model Intercomparison and Improvement Project), founded in 2010, defined protocols to analyze the agricultural systems and the food production by collecting and comparing the best available crop models [8]. The spatio-temporal variability of hydro-climatic variables (e.g. evapotranspirative rate, precipitation depth, wet days per year) has a high impact on agricultural requirements, with serious implications in terms of food security.

Earth Observation (EO) offers new possibilities to apply hydrological models at large spatial scales. According to the definition from the European Joint Research Centre, EO is *the gathering of information about planet Earth's physical, chemical and biological systems via remote sensing technologies, usually involving satellites carrying imaging devices* [9]. It is widely used to monitor and assess the status of the natural and manmade environment, also monitoring significant temporal changes. Technologies based on remote sensing allow to obtain reliable and repeat-coverage datasets, measuring radiance all over the Earth's surface. Combining EO measurements with appropriate methods, it is possible to gather comprehensive hydrological information for large-scale modelling.

The research of how climate change influences the global hydrological cycle is very important to quantify the impact on agriculture, also considering that world population is expected to reach 10 billion between 2050 and 2060 [10]. In order to improve the reliability of large-scale estimations, a cross-sectoral approach is essential.

1.2 Research motivations and objectives

Climate change is expected to produce several impacts on agriculture. Proper adaptation strategies must match up the needs for global food supply and for sustainable production chains. The optimal crop growth is highly related to climate conditions, whose variability can lead to water stress and production losses [11]: in fact, the spatio-temporal variability of precipitation and evapotranspiration has significant consequences on crop requirements and needs for irrigation [12]. Therefore, the study of how climate variability impacts the crop irrigation requirements is important to manage agricultural and water resources across local, regional and global scales.

Since remote sensing data were introduced in large-scale studies, most of the global crop models were updated by introducing satellite information or satellite-derived products. Yet, there is still a lack of scientific literature exploiting the potential of the most up-to date EO products to improve the accuracy of multiannual global evapotranspiration assessments at the daily temporal scale.

The present thesis aims at filling this gap, assessing the impact of climate variability on multi-decade crop water requirements, analyzing spatio-temporal changes of irrigated and rainfed crop needs and stress periods. For this reason, a hydrological model for the assessment of crop evapotranspirative demand was developed and tested for year 2000. The model was also used for a multi-decade assessment, highlighting significant climate-driven impacts on global agriculture over the last 50 years.

The main questions this thesis aims to answer are: (i) can EO-based products be used to set up a soil-water balance model for the assessment of climate-driven agricultural water requirements, highlighting the global spatial variability? (ii) can we describe the spatio-temporal changes of global crop water requirements and highlight significant climate-driven trends using EO-based data? (iii) Can satellite data be used to reduce the uncertainty related to crop growth modelling, in order to improve the accuracy of agricultural assessments? For this purposes, a list of 26 main crops was considered within a comprehensive assessment, from 1970 to 2019. On irrigated croplands, the model was used to identify significant changes of irrigation requirement rates and days requiring irrigation; on rainfed areas, the analysis of significant trends of water stress was performed. Lastly, the satellite data from the Sentinel constellation were used to retrieve actual sowing periods and growing phases of maize, over a pilot area in Northern Italy. Technologies based on Earth Observation allow new possibilities for the study of climate impact on crop water requirements. Since the assessment was based on daily hydroclimatic data, this thesis aims to analyze the spatio-temporal variability of

days requiring irrigation (on croplands equipped for irrigation) and days experiencing water stress (on rainfed croplands).

One of the main uncertainties which this thesis aims to deepen is related to the lack of information about actual length of crop developing phases. For those crops which are sowed and harvested within the same year, a proper knowledge of actual sowing dates can significantly improve the reliability of the requirement estimation at the local scale. Satellite data can be used to retrieve information about crop growth and the health of plants during the agricultural season, especially combining information from different types of sensors. In this thesis, a synergic use of optical and radar information was used to retrieve the spatial distribution of actual sowing periods at the field scale. When the estimation of water needs is performed on a local scale, a detailed information of crop planting periods can be used to set the models considering needs referred to actual growing periods.

In Chapter 2, the methodology used to develop the soil-water balance model for the assessment of crop-specific water needs is presented. The EO-based hydro-climatic data and the crop growth modelling are described, and the assumptions for computing the daily estimation of actual evapotranspiration, water stress and irrigation requirement are discussed in detail. The model was used for a global assessment of irrigation requirements, using the daily hydro-climatic data from the Climate Change Service of the Copernicus European Programme as model forcings. The assessment was performed for year 2000 because of the availability of crop data and national irrigation withdrawals for this year, allowing a comparison between our estimations and actual irrigation data.

In Chapter 3, the model was used to calculate the global crop water requirements on rainfed and irrigated croplands, over a 50-year period (1970-2019). Results were analyzed in terms of daily statistics of irrigation requirements (on areas equipped for irrigation) and stressed periods for rainfed crops. A statistical analysis was performed to detail the spatial variability of significant trends of irrigation requirements and crop water stress, focusing on the areas where the impact of climate variability induced a high variation of these parameters from 1970 to 2019.

In Chapter 4, the optical and radar data from the Sentinel constellation were used to retrieve maize actual sowing periods and growing phases, over a pilot area in North-West Italy. Since one of the most important uncertainties in modelling the large-scale crop water requirements is related to the lack of information about actual sowing periods and length of growing seasons, this analysis aims to develop possible satellite-based solutions. The method was tested at the local scale, detecting the emerging periods of plants (e.g., the periods when plants break through the soil and start to grow) and retrieving the number of days occurred between emerging and sowing according to the air temperature and soil moisture conditions.

1.3 Earth Observation for hydrology and agriculture

In recent years, Earth Observation-based products have become a reliable and affordable source of information for several research fields. The study of the Earth System requires as many global information as possible, with continuous monitoring of environmental variables. Hydrological and agricultural models can benefit from the EO-based study of the Earth in several respects.

The assessment of crop water needs, the study of available water sources, the classification of irrigated croplands are just some of the research fields for which EO is gaining in significance. For example, the systematic review by Massari et al. [13] analyze many EO datasets, models and algorithms to highlight the potential of remote sensing data in the quantitative assessment of irrigation events and volumes. Several studies point out the reliability of combined optical and radar signals retrieved from satellites in the classification of irrigated croplands, in different climatic scenarios and parts of the world (e.g., the application by Dari et al. [14] in central Italy or the analysis by Brazzi et al. [15] over the Spanish region of Catalonia). Remote sensing is also a reliable instrument to describe the crop growing phases at the field scale by detecting high resolution imagery, as described by Gao et al. [16]. Most of the sector studies exploit the potential of remote sensing for retrieving crop parameters in arid and semi-arid regions, especially when combined with in situ information (e.g., the work by Ayari et al. [17] in Tunisia).

The combined use of remote sensing data, crop developing models and hydrological models allows to improve quantitative assessment, in the study of irrigation at the field scale: for example, Le Page et al. [18] combined SAR and optical information with in-situ data to build a soil water balance model, with the objective of detecting irrigation events in different pilot sites. The potential of remote sensing in the agricultural field is also related to the fast improvement of satellite sensors, especially those supposed to retrieve multi-bands and multi-frequency radar backscattering, as pointed out by Ayari et al. [19]. EO-based agricultural monitoring has, therefore, a high potential to reduce uncertainties in the crop models, mainly related to local policies, undeclared crop switches, crop rotation and availability of water for irrigation.

Remote sensing is the technological base of precision agriculture, defined as *a management strategy that gathers, processes and analyzes temporal, spatial and individual data and combines it with other information to support management decisions according to estimated variability for improved resource use efficiency, productivity, quality, profitability and sustainability of agricultural production* (definition adopted by the International Society of Precision Agriculture [20]).

The use of remote sensing for agricultural applications has grown exponentially during the last decades. The possibility of managing and monitoring crops acquiring information from remote sensors has paved the way for many innovations in agriculture. Technologies for the measurement of electromagnetic energy reflected and emitted from ground surfaces are now widely used to measure vegetation parameters and hydrological variables, using drones, aircrafts and satellites.

Precision agriculture is based on sensors installed on vehicles like satellites, aircrafts, airplanes and drones. Each type of vehicle is suitable for a specific range of operations and, of course, is designed to carry sensors for specific purposes. This thesis focuses on large scale applications, for which remote sensing provides some of the best solutions and the easiest tools for agricultural analyses. Products retrieved from EO technologies different from satellites were not exploited in this thesis. In this Chapter, an overview of the most used satellites and related sensors for agriculture and hydrological modelling is presented.

1.3.1 Satellite sensors

The spread of satellites for EO is one of the most innovative and high-potential technologies for large scale applications. Each satellite is equipped with sensors which are suitable for a set of specific measurements, depending on the aim of each space mission. Satellites are sent to fly over the globe, describing orbits and "photographing" electromagnetic signals from the surface. Each frame (i.e. the sensor's swath) is acquired with fixed dimensions, depending on the technical specifications of the sensor. Moreover, the satellite sensors are sensitive to a wide range of bands, from visible to microwaves, and they can measure the radiation emitted or reflected by the ground surface but also capture the backscattering signal emitted by an active source (which, in most of the cases, is located on the satellite itself).

The measurement of electromagnetic signals from the Earth surface can have multiple applications. They can be used to retrieve daily estimations of meteorological variables, like rainfall or snow; agricultural applications include crop classifications, monitoring of plant health status, monitoring of growing phases and dry conditions, yield estimations; satellite data can also be used to manage emergency scenarios, like flooding or fire. These data are furthermore important for the climate and meteorological models, both for the prediction of weather conditions on short term and the implementation of long-term climate datasets. Satellite data are often combined with ground measurements, for the calibration and validation processes. Each agricultural use requires specific

frequency bands and having a range of bands as wide as possible is important to increase the range and the quality of potential application.

Sensors can be classified according to their resolution, which indicates the potential detail provided by the imagery. There are three types of resolution:

- Spatial resolution: indicates the number of pixels (i.e., the smallest discrete element of a digital image) per image. It is usually provided as a technical feature of the sensor, indicating the size of a square pixel composing the image. For example, if the nominal spatial resolution of a sensor is 4 m, each pixel will represent a 4 m x 4 m square of land.
- Spectral resolution: the ability to acquire and measure specific ranges of electromagnetic wavelengths. As resolution increases, the acquisition bands capture narrower ranges of wavelengths.
- Temporal resolution: indicates the frequency of acquisition of the satellite over a certain point. This concept is related to the "revisit period" (or "revisit time"), i.e. the time required to the sensor to pass over the same orbit and acquire data over a reference frame. However, the temporal resolution can be higher than the revisit time, since it accounts the non-nadir acquisitions acquired over a certain point which can be observed by partially-overlapping orbits.

In this work, the term "resolution" will usually indicate the spatial resolution, except where otherwise indicated.

The first use of satellite EO for agricultural purposes was performed in 1972, after the launch of the first Landsat satellite. The Landsat-1 (NASA) was the first step of the American EO Programme based on satellite imagery, and the mission was equipped with a MSS (Multispectral Scanner System) acquiring visible and near-infrared data at the spatial resolution of 80 meters, with a revisit period of 16 days. Since then, the number of operative satellite sensors which are suitable for agricultural applications has increased significantly, as well as the number of studies based on this technology. In fact, the number of papers focusing on agricultural remote sensing which was published in 2020 was about ten times higher than those published in year 2000 [21]; this is due to the progressive improvement of the computer possibilities and new satellite platforms like cube-sats, allowing researchers easy access and use of this data, and the new global food security challenges that humanity is called to face. Moreover, new computing platforms are now available to deal with the high requirements of satellite data, in terms of storage volumes and processing capabilities. This is the case of Google Earth Engine (GEE), where a huge volume of historical data is available, including images acquired by a wide range of satellites; in addition, GEE provides a python-based command window to process the data directly in the cloud, and to define the spatio-temporal borders of the analysis.

In **Table 1** are listed the most used optical sensors for agricultural applications, detailing the main technical characteristics [22]. The optical data measure the electromagnetic signal from Earth surface in the spectrum of visible and infrared. The sensors are usually designed to retrieve information in two modes: "panchromatic" and "multispectral". The panchromatic mode is used to maximize the spatial resolution, to the detriment of the spectral resolution; the multispectral mode is able to retrieve information for different spectral bands, providing multi-level rasters (e.g., the blue, green and red bands for the Visible): this result is achieved losing some spatial resolution. The multispectral mode is the most widely used for scientific analysis in agriculture [21], especially because the availability of "very high resolution" sensors has increased in the last years.

Optical bands are often combined to retrieve indices which are sensitive to specific variables or elements. For example, the normalized difference between the Red and Near-Infrared bands is commonly called NDVI (Normalized Difference Vegetation Index), which is a widely used index for agricultural applications, including crop classifications, growing monitoring and to derive information about plant health status.

In **Table 2** some of the most used satellite indices derived from optical information are listed: this type of measurements is very popular in the scientific research concerning agricultural analysis.

Microwave sensors provide another important group of EO data. The remote sensing systems which just measure the microwaves emitted by the surface are called "passive", while the "active" sensors measure the backscattering of a signal which is emitted by an antenna installed on board the satellite itself.

In **Table 3** are listed the most important radar satellites for agricultural applications [23]. Radar data can be used for several purposes by choosing appropriately the technical specifics of the sensor: in particular, the choice of a radar product shall take into account the acquisition band of the antenna and the polarization of the signal.

The radar polarization depends on the coupled system of emitting and receiving antennas. It refers to the orientation (horizontal or vertical) of the microwave signals which are emitted and received by the sensor. Most of the active radars are designed to transmit microwaves in vertical and horizontal modes, and also the received signal can be measured in the two components. There are four possible configurations defining the polarization of radar data: VV (Vertical-Vertical), HH (Horizontal-Horizontal), VH (Vertical-Horizontal), HV (Horizontal-Vertical). The first letter indicates the polarization of the emitted signal; the second letter refers to the component of the backscattering signal which is measured by the sensor. For example, VH indicates that the microwaves are emitted with vertical polarization and the horizontal component of the backscattering signal is measured.

Table 1. List of the most used sensors for agricultural applications, operating in the visible and infrared spectrum. The sensors are classified according to the pixel size (ps): Low Resolution (ps > 100 m), High Resolution (10 m < ps ≤ 100 m), Very High Resolution (ps ≤ 10 m). (*) p: to present. The swath is the size of the photograms acquired by the sensors. Acronyms used for the spectral ranges. VIS: visible; NIR: near-infrared; SWIR: shortwave infrared; MWIR: midwave infrared; LWIR: longwave infrared; TIR: thermal infrared.

Visible and Infrared sensors						
			Resolution		Swath (km)	Life time
Mission (sensors)	Nation	Bands	Panchromatic Mode	Multispectral Mode (Number of Bands)		
Low Resolution (LR)						
NOAA 6-20 (VIIRS)	U.S.	VIS/NIR/SWIR/ MWIR/ LWIR	-	370 m/740 m/1.1 km/8 km (22)	2400	1979 – p*
SPOT 4-5 (Végétation)	France	VIS/NIR/SWIR	-	1.15 km (4)	2000	1998 – 2015
Terra (MODIS)	U.S.	VIS/NIR/SWIR/ MWIR/ LWIR/TIR	-	250 m/500 m/1 km (36)	2330	1999 – p*
High Resolution (HR)						
SPOT 1–3 (HRV)	France	VIS/NIR	10 m	20 m (4)	60	1986 – 2013
SPOT 4 (HRVIR)	France	VIS/NIR/SWIR	10 m	20 m (4)	60	1998 – 2017
Landsat 7 (ETM+)	U.S.	VIS/NIR/SWIR/TIR	15 m	30 m (8)	185	1999 – p*
SPOT 5 (HRG)	France	VIS/NIR/SWIR	2.5 m/5 m	10 m/20 m (4)	20	2002 – 2015
THEOS-1 (MS, PAN)	Thailand	VNIR	2 m	15 m (4)	22	2008 – p*
Landsat 8-9 (OLI, TIRS)	U.S.	VIS/NIR/SWIR/TIR	15 m	30 m (8)	185	2013 – p*
Sentinel-2 A/B (MSI)	Europe	VIS/NIR/SWIR	-	10 m/20 m/60 m (13)	290	2015 – p*
Very High Resolution (VHR)						
Kompsat-2 (MSC)	South Korea	VIS/VNIR	4 m	1 m (4)	15	1999 – p*
Ikonos (OSA)	U.S.	VIS/NIR	0.82 m	3.20 m (4)	11	2000 – 2015
Quick Bird (BGIS-2000)	U.S.	VIS/NIR	0.65 m	2.62 m (4)	16	2001 – 2015
Geo Eye (GIS)	U.S.	VIS/NIR	0.41 m	1.64 m (4)	15	2008 – p*
World View 1 (WV60)	U.S.	VIS/NIR	0.5 m	-	17.6	2008 – p*
World View 2-3 (WV110)	U.S.	VIS/NIR	0.46 m	1.84 m (8)	16.4	2009 – p*
Pleiades/PleiadesNeo	France	VNIR	0.50 m/0.30 m	2 m/1.2 m (4/6)	20/14	2013 – p*
SPOT 6–7 (NAOMI)	France	VIS/NIR	2 m	8 m (4)	60	2013 – p*
Gao Fen 1–6 (PMS)	China	VIS/NIR	2 m	8 m (4)	90	2014 – p*
World View 4 (SV-110)	U.S.	VIS/NIR	0.31 m	1.24 m (8)	13.1	2016 – p*
Super View 1-4 (PMS-3)	China	VIS/NIR	0.50 m	2 m (4)	12	2016 – p*
THEOS-2 (MS, PAN)	Thailand	VIS/VNIR	0.5 m	2 m (4)	10.3	2022 – p*

Table 2. List of the most common satellite-based indices for agricultural applications. R: radiation band (in some cases the nominal name is specified, e.g. R430: numbers refer to the wavelength in nanometers [nm]).

	Index	Equation	Application
EVI	Enhanced vegetation index	$\dfrac{2.5(R_{NIR} - R_{RED})}{(R_{NIR} + 6R_{RED} - 7.5R_{BLUE} + 1)}$	Disease, biomass
MSI	Moisture Stress Index	$\dfrac{R_{SWIR_2}}{R_{NIR}}$	Vegetation water content
NDII	Normalized Difference Infrared Index	$\dfrac{R_{NIR} - R_{SWIR_2}}{R_{NIR} + R_{SWIR_2}}$	Vegetation water content, leaf stress detection
NDMI	Normalized Difference Moisture Index	$\dfrac{R_{NIR} - (R_{SWIR_1} - R_{SWIR_3})}{R_{NIR} + (R_{SWIR_1} - R_{SWIR_3})}$	Forest analysis and detection
NDSI	Normalized Difference Soil Index	$\dfrac{R_{SWIR} - R_{NIR}}{R_{SWIR} + R_{NIR}}$	Soil classification
NDVI	Normalized Difference Vegetation Index	$\dfrac{R_{NIR} - R_{RED}}{R_{NIR} + R_{RED}}$	Biomass, breeding, phenotyping, yield, disease, n-management, soil moisture, water stress
NDWI	Normalized Difference Water Index	$\dfrac{R_{GREEN} - R_{NIR}}{R_{GREEN} + R_{NIR}}$	Vegetation water content
NPCI	Normalized Pigment Chlorophyll Ratio Index	$\dfrac{R_{680} - R_{430}}{R_{680} + R_{430}}$	Water stress
SIWSI	Shortwave Infrared Water Stress Index	$\dfrac{R_{858.5} - R_{1640}}{R_{858.5} + R_{1640}}$	Leaf water content, water stress
WABI	Water Balance Index	$\dfrac{R_{1500} - R_{531}}{R_{1500} + R_{531}}$	Irrigation sceduling

Each polarization is used to retrieve specific information, since the emitted microwaves are backscattered according to the characteristics of the reflecting surface, like the soil water content and the geometric structure of the ground.

The most used classification of radar bands was proposed by the Institute of Electrical and Electronics Engineering (IEEE), assigning letters to defined ranges of signal frequencies: L (1 - 2 GHz); S (2 – 4 GHz); C (4 – 8 GHz); X (8 – 12 GHz); Ku (12 – 18 GHz); K (18 – 27 GHz); Ka (27 – 40 GHz); V (40 – 75 GHz); W (75 – 110 GHz). The most used bands for agricultural applications are the C and L bands, which have important capabilities for the crop classification, monitoring of crop growth, detecting biomass and estimating soil moisture. Each band has specific advantages and limitations (e.g. the L band is characterized by a higher penetration depth in presence of high-vegetation [24]). In Chapter 4, will be discussed the potential of the C band from Sentinel-1, for the monitoring of maize growing phases and estimation of sowing dates. However, a detailed analysis of the potential applications of radar bands is not the aim of this thesis.

Table 3. List of the most used sensors for agricultural applications, operating in the microwave spectrum. (*) p: to present. Wavelength and frequency range of radar bands. L: 15-30 cm (1-2 GHz); S: 8-15 cm (2-4 GHz); C: 4-8 cm (4-8 GHz); X: 2.5-4 cm (8-12 GHz). The swath is the size of the photograms acquired by the sensors. Polarization acronyms: the first letter indicates the polarization of the transmitted signal; the second letter refers to the polarization of the receipt signal. VV: Vertical-Vertical; HH: Horizontal-Horizontal; VH: Vertical-Horizontal; HV: Horizontal-Vertical; Quad.: combining all four polarizations; Dual.: combining two polarization modes, usually VV and VH (i.e. the case of Sentinel-1).

Radar sensors							
Mission (sensor)	Nation	Frequency band	Active/ Passive	Resolution	Polarization	Swath (km)	Life time
ERS 1-2 (AMI-SAR, AMI-SCAT)	Europe	C	A	30 m	VV	5/500	1991 - 2011
JERS-1 (SAR)	Japan	L	A	18 m	HH	75	1992 - 1998
RADARSAT-1 (SAR)	Canada	C	A	8 m/100 m	HH	50/500	1995 - 2013
ENVISAT (ASAR, RA-2, MWR)	Europe	C	A/P	1 km/30 km	Quad.	56/40	2002 - 2012
Coriolis (WindSAT)	U.S.	C	P	7 km/80 km	Dual.	1000	2003 - p*
COSMO-SkyMed (SAR-2000)	Italy	X	A	1 m/100 m	Quad.	10/200	2007 - p*
Metop A/B/C (ASCAT, AVHRR)	Europe	L/S/X	A/P	25 km/50 km	VV	500/550	2007 - p*
RADARSAT-2 (SAR)	Canada	C	A	3 m/100 m	Quad.	18/500	2007 - p*
TerraSAR-X (SAR-X)	Germany	X	A	1 m/16 m	Quad.	5/150	2007 - p*
SMOS (MIRAS)	Europe	L	P	35 km	Dual.	1000	2009 - p*
ALOS-2 (PALSAR-2)	Japan	L	A	1 m/100 m	Quad.	25/350	2014 - p*
Sentinel-1 A/B (SAR-C)	Europe	C	A	10 m/84 m	Dual.	20/400	2014 - p*
SMAP (SMAP)	U.S.	L	A/P	3 km/10 km/40 km	VV, HH, HV	1000	2015 - p*
ALOS-4 (PALSAR-4)	Japan	L	A	1 m/25 m	Quad.	35/700	2021 - p*

1.3.2 EO-derived products for large-scale agricultural applications

Applications of satellite data and products derived from remote sensing in the field of hydrological and agricultural modelling are the basis of this dissertation. As previously introduced, EO can be used directly to compose raster images, perhaps after a pre-processing of raw acquisitions, or the different bands can be combined to retrieve satellites indices.

A third possibility consists in the use of remote sensing data into systems and models retrieving information with uniform large-scale spatial details; for example, global climate gridded datasets, maps of land use, elevation models and soil properties. Since remote sensing provides information with relatively high frequencies, this EO source is now widely used within climate and weather models, as well as for a wide range of systems classification and monitoring of the Earth's surface.

In the next sections, three main classes of variables derived from remote sensing were introduced, which were used to the aim of this thesis. A more detailed list of the most important EO-based products is provided in Appendix A.

Climate variables

The use of remote sensing to retrieve large-scale climate data is nowadays a well-established technique used by the researchers all around the world. Despite gauged measurements still provide most accurate data of rainfall, soil moisture, temperatures, winds, hail and other meteorological variables, the study of global climate requires systems able to describe all the Earth surface, including oceans and places unfit for human life. The most used gauge-based climate datasets are obtained by interpolating the network of ground measurements. However, the accuracy of the distributed result is strictly dependent on the density and the uniformity of the measurement network.

Remote sensing measurements cover all the globe surface, acquiring information at intervals of few days. This information is now used by research centers and spatial agencies to retrieve large-scale gridded data of climate variables or assimilated by the re-analysis gridded models. In the latter case, climate variables are not directly derived from satellite observations, but remote sensing and ground observations are combined into global estimates using advanced modelling and data assimilation systems. In this work, precipitation and temperature from a re-analysis dataset were used as driving input for a multiannual modelling at the global scale: it is therefore useful to better detail the difference between satellite-based climate data and reanalysis products.

The methods used to derive climate data from satellite information can be classified according to the spectral range of measured signals. For example, the satellite-based estimation of precipitation can be retrieved using VIR and NIR, according to the principle that cold and bright clouds are associated to convections [25]. An important instrument to derive precipitation data from satellite sensors is the microwave measurement: rainfall can be estimated through algorithms which measure the soil moisture variability through radar sensors, e.g. the SM2RAIN global dataset derived from ASCAT measures [26].

Reanalysis products are another important source of large-scale climate data, which are based on observations from several sources (including satellite sensors) and the assimilation of the observed information in background forecast models. This kind of datasets are widely used in climate research, for the monitoring of current climate and the comparison with past conditions. The available historical observations are used to define a wide variety of climate gridded maps, by running modern short-range weather forecasts models. The global coverage of the reanalysis products, the uniform consistency of the grids (sometimes called "maps without gaps") and the high temporal resolution of the obtained information make this kind of data very useful for climate-based analysis.

Soil properties

EO techniques are widely used to retrieve soil properties for spatial datasets. The combined use of multiple types of sensors is a valuable instrument to describe the physical and chemical properties of soils, like bulk density, cation exchange capacity, organic carbon, pH, soil texture fractions and coarse fragments. Modern machine learning methods can combine the EO information, ground data and soil regional profiles to retrieve a wide variety of large-scale maps to describe soil properties at different depths.

The measurement of soil water content and its temporal variability is at the basis of most of the models describing the agricultural water uses: soil moisture is a very important parameter for the assessment of crop water use at any spatial scale, and is strictly dependent on soil properties. The soil texture defines the capacity of soils to retain water, which is a key factor for the assessment of crop water stress and the study of irrigation requirements.

Remote sensing is now widely used to produce large-scale gridded data of soil parameters.

Most of the studies focused on large-scale agricultural water assessments adopted different assumptions to assign a soil moisture initial level at the beginning of growing seasons, taking into account the soil's ability to retain and store water. In Chapter 3 will be discussed the sensitivity of global crop water requirement assessments to the soil water content at the sowing date, and the

method based on soil parameters and climate variables to initialize the growing season will be described.

Land classification

The classification of the land surface is one of the first uses for which EO was used for. The descriptive study of land uses, temporal changes of vegetation extensions, dynamics of hydrographic networks, digital elevation models (DEM) are just some of the possible applications of satellites for the Earth monitoring. Agriculture is one of the sectors that benefits most from the remote sensing technologies, in terms of increasing of crop yields, monitoring of plant health and dynamic mapping of crop types and irrigation practices.

The digital image classification is a process assigning features to a pixel (or groups of pixels) composing rasters. The agricultural classifications derived from remote sensing measurements are firstly used to identify croplands. Services like the Copernicus Land Service (CLS) provides global rasters of croplands at high spatial resolution (e.g., CLS global map of croplands at 100x100 m resolution [27]). The classification methods work on the basis of training processes (supervised and unsupervised) or on the basis of theoretical models (parametric and non-parametric).

Large-scale agricultural assessments are often based on spatial data of extents of crop-specific areas, which may contain further information on irrigation practices and sowing schedules. The definition of a dynamic agricultural classification combining these information is one of the most ambitious challenges remote sensing could help to address.

In this dissertation, will be particularly exploited the global crop classification from the MIRCA 2000 dataset, which will be detailed in Chapter 2. A more detailed review of the available global crop datasets is presented in Appendix A.

Chapter 2

Global assessment of crop irrigation requirements

The work described in this Chapter has been partially derived from paper [28].

As already briefly mentioned in Chapter 1, irrigated croplands provide 40% of global agricultural production, despite these areas only represent about 20% of total croplands. Therefore, assessing irrigation requirements is essential for the development of effective water-related policies for an efficient management of water resources. Moreover, global-scale analyses are becoming increasingly relevant, motivated by globalized production and international trade of food as well as by the need of common strategies to address climate change.

In this Chapter, a comprehensive model to estimate crop growth and irrigation requirements of 26 main crops at global scale is presented. The model computes a soil water balance using daily precipitation and reference evapotranspiration based on the ERA5 reanalysis dataset, prided by the European Copernicus Program. The irrigation requirement, defined as the minimum water volume to avoid water stress, is computed for year 2000 at the resolution of 5 arc-min (or 0.0833°) and aggregated at different spatial and temporal scales for relevant analyses. The analysis was performed for year 2000 because of the availability of crop data and national withdrawal for this specific year, testing the model before the computation of crop requirements over a multi decade period (as described in Chapter 3).

The estimated global irrigation requirements of 962 km^3 is described in detail, also in relation to the spatial variability and to the monthly variation of the requirements. Three different areas of the world (California, Northern Italy and India) were analyzed in detail, to highlight the wealth of information provided by the model in different climatic conditions. National data of irrigation withdrawals have been used for an extensive comparison with model results. A crop-specific validation has also been made for the State of California, comparing model results with local data of irrigation volume and independent estimates of crop water use. In both cases, a good agreement was found between model results and real data.

2.1 Numerical models for the assessment of crop water requirements

As previously introduced, the irrigation requirement is intended as the amount of water provided to crops when precipitation does not entirely satisfy the evapotranspiration demand. A number of high-resolution assessments of global irrigation requirements exist. The first ones were based on WaterGAP [29], WATERSIM [30], LPJmL [31] and H07 [32] models, which mostly did not consider multi-cropping practices (i.e. the sequence of multiple growing seasons on the same area, e.g. "winter" and "spring" wheat) and provided little crop-specific results. The comparison in **Table 4** shows that latest assessments are generally referred to year 2000, because of the availability of crop-specific information of irrigated areas for that year. This is the case for the GCWM [33], GEPIC [34], the assessment based on the CROPWAT model proposed by FAO [35], and the WATNEEDS model [36].

Table 4 shows that the spatial resolution of global models has increased over the years, mainly because of the release of crop-specific datasets of irrigated areas. In this work, the model used for the computation of crop irrigation requirements is the one presented by Rolle et al. [28].

With the exception of Chiarelli et al. [36], who uses high-resolution daily precipitation, the previous models are rarely based on daily data, or they provide results on lower spatial resolutions (e.g. 1° in Hanasaki et al. [32]). The present thesis is based on daily global data for both precipitation and reference evapotranspiration, working on a relatively high spatial resolution grid to best reproduce detail within the global scale. The reference evapotranspiration was calculated with temperature data, according to the Hargreaves-Samani method [37], and calibrated through global comparison with a widely used monthly dataset. The estimate of irrigation requirements from this study has been compared both to results of other models and to actual data from irrigation volumes on different spatial scales.

The model presented in this Chapter aims to assess global irrigation requirements exploiting the potential of EO-based climate products, in the computation of a soil-water balance approach based on the FAO methodology [7].

For year 2000, spatial coverage resulting from 26 main crops is provided by the MIRCA2000 database. This dataset provides gridded data of croplands over the world at 5 arcmin resolution (0.0833°, about 9 km at the Equator), considering the specific area of each crop. The presence of irrigation infrastructures is also taken into account, since for every crop are provided separated grids describing areas equipped for irrigation and rainfed areas.

Table 4. Summary of models that estimate global irrigation requirement. Acronyms and notes used in the table. MCP: Multi-Cropping Practices. Reference Evapotranspiration methods: PM (Penman-Monteith), PT (Priestley-Taylor), HS (Hargreaves-Samani), SEB (Surface Energy Balance). Temporal resolution of data: (d) daily, (m) monthly, (m-LTA) monthly Long-Time Average (1961-1990). (*) 0.05° in the region between 50°N – 50°S, 0.5° in the rest of the world. (**) effective resolution of 0.166°, matching the two datasets. (a) Average result for the period 1998-2002. (b) Average result for the period 1996-2005. (c) The assessment provided an average result, using input data for the period 1986-1995. (d) The map of irrigated crops refers to year 2000. The assessment provides an average estimation using monthly climate data for the period 1971-2000.

		Global Models	**Spatial resolution**	**Base year**	**MCP**	**Precipitation**	**Reference evapotranspiration**	
2021	[28]	Rolle et al. 2021	0.0833°	2000	yes	0.25° (d)	0.25° (d)	HS
2020	[36]	WATNEEDS	0.0833°	2000[a], 2016	yes	0.05° (d), 0.5° (d)*	0.5° (m)	PM
2011	[35]	CROPWAT (FAO)	0.0833°	2000[b]	no	0.5° (m)	0.166° (m-LTA)	PM
2010	[34]	GEPIC	0.5°	2000	yes	0.5° (m)	0.5° (m)	HS
2010	[33]	GCWM	0.0833°	2000[a]	yes	0.5° (m), 0.166° (m-LTA)*	0.5° (m), 0.166° (m-LTA)**	PT, PM
2008	[32]	H07	1°	1991[c]	no	1° (d)	1° (d)	SEB
2008	[31]	LPJmL	0.5°	1985[d]	no	0.5° (m)	0.5° (m)	PM
2007	[30]	WATERSIM (IWM)	0.1°	2000	no	0.5° (m)	0.5° (m)	PM
2002	[29]	WaterGAP	0.5°	1995	no	0.166° (m-LTA)	0.166° (m-LTA)	PT

Growing periods are defined for temporary crops (i.e. those that are both sown and harvested during the same year) on a monthly basis. In order to use this information within a daily assessment, in this thesis is assumed that sowing and harvest occur on the 16th and the 15th day, respectively, of the given months, similarly to other studies (e.g. [38]). The length of a growing season is then considered as the number of days between the sowing and harvest dates. Growing periods for perennial crops (i.e. those that don't need to be replanted every year, like fruit trees) are defined by the green-up dates instead. Such dates are taken from Chapagain & Hoekstra (2004) [39] and refer to the FAO agro-climatic zones system (GAEZ) [40].

2.2 The MIRCA2000 crop dataset

The MIRCA2000 dataset is a global gridded crop dataset, providing cropland distribution for 26 main crops and monthly physical areas data circa 2000 [41]. All major food crops are included, some as specific products (e.g., maize, wheat, rice) and others as aggregated groups of agricultural products (e.g., perennial crops, pulses, fodder grasses). The advantage of this dataset, compared to other similar products, is that information is provided coupling crop-specific areas, presence of irrigation infrastructures and sowing and harvesting monthly calendars.

The spatial distribution of the global agricultural areas is represented in **Figure 1**, as ratio between cropland hectares and total land hectares: **Figure 1a** provides the spatial distribution of areas equipped for irrigation, while **Figure 1b** describes the spatial distribution of rainfed areas, according to MIRCA2000.
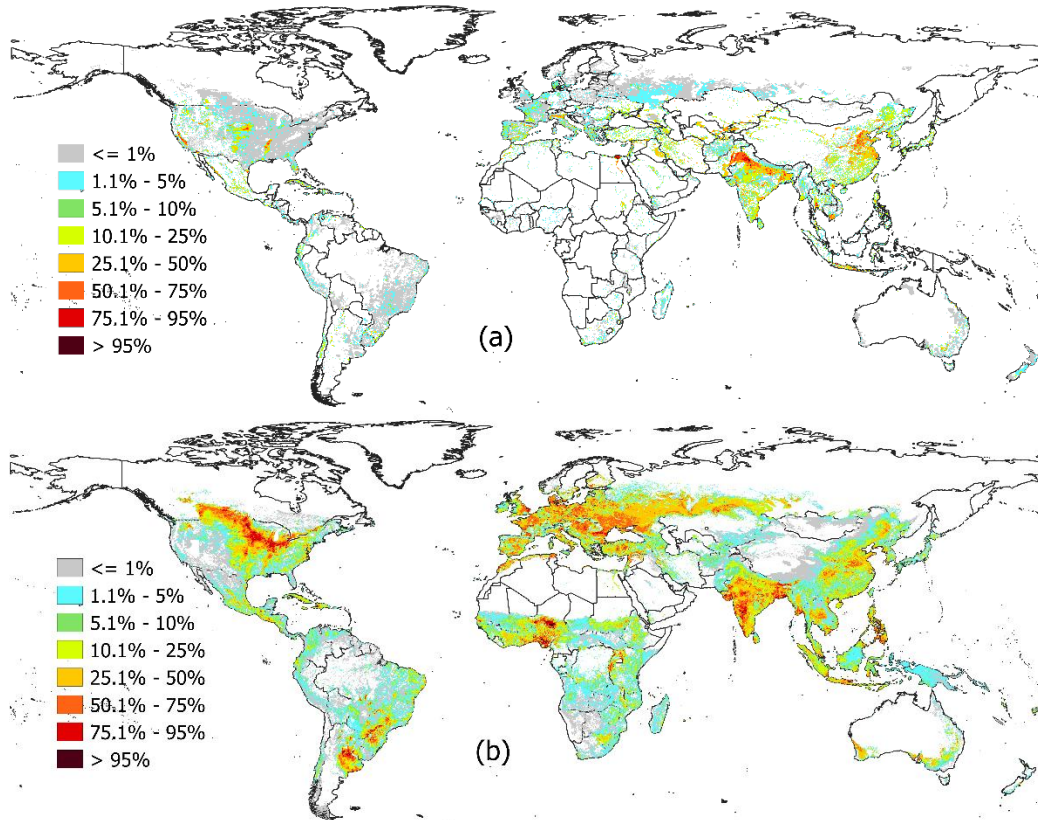
Figure 1. Spatial distribution of global croplands, according to the MIRCA2000 dataset (circa year 2000); (**a**) density of irrigated croplands, as percentage of agricultural area equipped for irrigation with respect to the total land area; (**b**) density of rainfed areas, as percentage of agricultural rainfed area with respect to the total land area.

Another important feature of this dataset is the information of multi-seasonal practices. Whether in rainfed and irrigated conditions, crops can be cultivated more than once per year: for example, wheat is cultivated both in winter and summer in many parts of the world. MIRCA2000 includes information of multi-seasonal crops and provides areas and calendars for every growing season. Irrigated rice, for example, accounts for three growing seasons per year in some regions of India. This information is particularly important for a multi-decade assessment of water requirements, allowing not only a comparison between the annual crop-specific results but also the analysis of temporal variability of seasonal requirements.

In **Table 5**, the crop-specific areas provided by the MIRCA2000 dataset are summarized, grouping separately the rainfed hectares and those equipped for irrigation.

Table 5. Crop-specific classes provided by the MIRCA2000 dataset (circa year 2000), as rainfed croplands and areas equipped for irrigation (AEI). The dataset provides spatial distribution, sowing and harvesting periods for 26 crops (21 primary products, like wheat and maize, and 5 aggregated classes).

Primary crops			Aggregated crop classes		
Crop	**Rainfed [ha]**	**AEI [ha]**	**Crop**	**Rainfed [ha]**	**AEI [ha]**
Wheat	1'479'284	666'322	Other annual	886'517	201'387
Rice	626'018	1'031'197	Fodder grasses	929'885	116'840
Maize	1'216'220	299'007	Other perennial	602'872	128'530
Soybeans	687'782	60'327	Pulses	616'644	54'558
Barley	504'810	46'458	Citrus	39'194	35'627
Sorghum	367'154	34'366			
Millet	318'949	17'437			
Cotton	168'994	162'522			
Rapeseed	212'321	34'038			
Groundnuts	190'449	36'758			
Sugarcane	107'570	101'890			
Sunflower	194'891	12'687			
Potatoes	159'631	37'455			
Cassava	154'424	112			
Rye	99'576	4'423			
Coffee	99'883	1'739			
Oil palm	96'404	110			
Grapes	54'150	17'267			
Cocoa	67'413	125			
Sugar beet	46'192	15'740			
Date palm	1'950	7'234			

2.3 ERA5: the ECMWF Re-Analysis 5 climate dataset

The introduction of hydroclimatic data from remote sensing has brought an important improvement to global models. Satellites are increasingly designed and used for agricultural applications [42], helping to identify irrigated lands [43] and indirectly to estimate irrigation volume [44]. The European Copernicus Program, started in 2014 as a continuation of GMES (Global Monitoring for Environment and Security), developed a system of satellites known as Sentinel Constellation to continuously monitor the Earth environment [45].

Reanalysis products provide complete pictures of past weather and climate, at high temporal resolution. They are a blend of observations with past short-range weather forecasts rerun with modern weather forecasting models. The reanalysis datasets are comprehensive and consistent in time, and are sometimes referred to as "maps without gaps" [46]. The reanalysis process of "data assimilation" combines past short-range weather forecasts and observations. This process imitates the calculation of day-to-day weather forecasts, which are based on the analysis of the current state of the Earth system to set a starting point.

In this study, the hydroclimatic data from the global re-analysis dataset ERA5 were used, i.e. the global reanalysis dataset produced by the European Centre for Medium-Range Weather Forecasts (ECMWF) as an improvement over the previous ERA-Interim product. This dataset was released by Copernicus in 2018 [47], providing hourly climate data that combines satellite information and ground measurements for 1950-present at the spatial resolution of 0.25° (i.e. about 31km at the Equator, a remarkable improvement compared to the 45 arc min, 6-hour spatio-temporal resolution of ERA-Interim).

As shown in Figure 2, ERA5 is based on assimilation of remote sensing and ground measurements and provides several hydro-climatic variables that can be useful in coupled hydrological-agricultural applications [48]. ERA5 is based on the re-analysis of tens of data acquisitions, both from remote sensing and conventional techniques. The number of observations assimilated in ERA5 has increased from about 0.75 million per day in 1979 to 24 million per day by the end of 2018. This re-analysis is produced through the Integrated Forecast System (IFS) of ECMWF (version Cy41r2, operative since 2016), and it's based on a 31 km resolution component (HRES) with 137 levels in the vertical spanning, from the surface to the 0.01 hPa quote [49].

In**Table 6**, ERA5 is compared to the most relevant re-analysis datasets which are currently available, including some products from ECMWF. The higher resolution, the large temporal period, the high temporal frequency of outputs and the global coverage make ERA5 one of the best products currently available for comprehensive modelling.
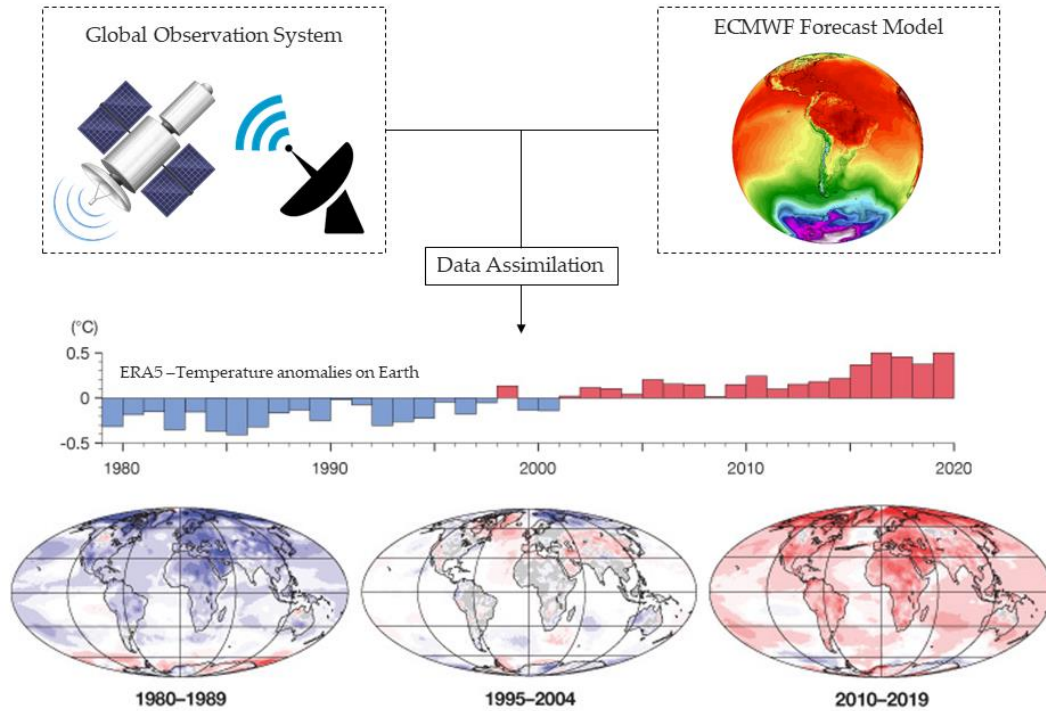
Figure 2. Conceptual scheme of the reanalysis process used by ECMWF to produce ERA5. Annual temperature anomalies on Earth (base period: 1981-2010). Credits by ECMWF.

Table 6. Summary of the most relevant large-scale re-analysis datasets. (*) ERA-Interim has been replaced by ERA5, but many studies still provide estimates and performance analyses based on this dataset; p: present.

Re-analysis dataset	Institution	Coverage	Period	Output	Grid spacing	Levels	Assimilation scheme
ERA5	ECMWF	Global	1950-p	1 h	0.25°	137	4D-Var
ERA5 Land	ECMWF	Global	1950-p	1 h	0.1°	60	4D-Var
ERA-Interim*	ECMWF	Global	1979-2019	6 h	0.75°	60	4D-Var
MERRA-2	NASA	Global	1980-p	1 h	0.5° x 0.625°	72	3D-Var-FGAT
JRA-55	JMA	Global	1978-p	6 h	0.625°	60	4D-Var
COSMO-REA6	DWD	Europe	1995-2019	1 h	0.055°	40	Nudging
UERRA	ECMWF	Europe	1961-2019	6 h	0.1°	60	3D-Var
NARR	NCEP	North-America	1979-2019	3 h	0.25°	60	3D-Var

The reliability of ERA5 for agricultural applications finds confirmation in the recent release of new products derived from ERA5 and available through the Copernicus Climate Change Service. In particular, the AgERA5 dataset provides daily surface meteorological data for the period from 1979 to present as input for agriculture and agro-ecological studies [50]. The climate data from AgERA5 are aggregated at the daily scale and include the most useful information for the estimation of actual evapotranspiration (however, this dataset had not been yet released at the time the analyses described in the present thesis were carried out).

In this Chapter, the methods and results related to the assessment of global irrigation requirements for year 2000 are described. In this case, the hourly data of precipitation and temperatures for year 2000 were downloaded and aggregated at the daily scale as described in the next Chapter. In Chapter 3, the extension of the analysis to the 1970-2019 period will be described, detailing the method used for the processing of ERA5 data over these years.

2.4 Estimation and calibration of Reference Evapotranspiration

The reference evapotranspiration (ET_0), defined as the evapotranspiration rate [mm/day] from a hypothetical well-watered grass surface with fixed characteristics [7], was calculated using the Hargreaves-Samani (HS) method [37]. The expression for daily ET_0 [mm/day] reads:

$$ET_{0,i} = k_{HS} \times R_{a,i} \times (T_{mean,i} + 17.8)\sqrt{T_{max,i} - T_{min,i}} \, , \qquad (1)$$

where k_{HS} is an empirical coefficient (fixed to 0.0023 in the original formula [37]), $T_{max,i}$, $T_{min,i}$ and $T_{mean,i}$ are respectively the maximum, minimum and mean temperatures for the *i*-th day (in °C) and $R_{a,i}$ is the equivalent evaporation (in mm), calculated as ratio between the top-of-atmosphere radiation and the latent heat of vaporization of water ($1/\lambda = 0.408$). Temperature and radiation are daily-averaged ERA5 data. The value 17.8 in Equation (1) imposes a null ET_0 when $T_{mean} = -17.8°C \approx 0°F$.

All the variables required for the application of (1) were taken from ERA5 and were aggregated on a daily scale. The top-of-atmosphere radiation could be calculated using a geometric approach, but the ERA5 product was chosen to be consistent with the spatial grid of temperature data. In order to obtain daily rainfall, the available hourly precipitation data from ERA5 were aggregated summing values from 1:00h to 0:00h in each day. Climate data were downloaded through the Application Programming Interface (API) of ECMWF and subsequently processed to match the MIRCA2000 spatial grid.

Since the HS approach requires only temperature and top-of-atmosphere radiation data, this method was chosen to reduce the uncertainty related to using many other daily variables (e.g. relative humidity, wind) which are required by the Penman-Monteith (PM) method. Although the HS method is a valid alternative to the PM method [7], the HS estimations were calibrated by comparing the annual ET_0 with annual gridded values of PM-based ET_0. In this way, the daily ET_0 were easily estimated using only temperature data, being consistent with a method recommended by FAO.

The calibration was performed by introducing the spatial variability of the k_{HS} coefficient, in order to provide consistency with the annual estimates from PM available in the CRU Time-Series global dataset [51]. This procedure was developed according to the monthly calibration described by Heydari et al. [52]. The yearly HS evapotranspiration has been upscaled on a 0.5° resolution to match the spatial grid of CRU. The k_{HS} coefficient were obtained by multiplying 0.0023 by the ratios between annual PM and HS reference evapotranspiration values. Finally, the k_{HS} values were downscaled to match the MIRCA2000 grid, proportionally to the uncalibrated ET_0 values in each pixel. The calibrated empirical coefficients were used to calculate the daily ET_0, according to (1).

The daily ET_0 from Equation (1) has been computed on the global grid of 0.0833° for the whole year 2000. The mean value of the calibrated k_{HS} coefficients in Equation (1) was 0.0024 over the irrigated cells, with a standard deviation of 0.0004. The calibration produced higher coefficients along coastal and arid regions, which is consistent with the tendency of HS to underestimate ET_0 in these scenarios [53].

Results obtained have been compared with the PM reference evapotranspiration from CRU Time-Series [51] for the months of January and July, as shown in **Figure 4**. The scatterplots compare, on a global scale, the monthly ET_0 from the PM and HS methods, in primarily cultivated areas, i.e. in cells where the cultivated portion is greater than 90% of the pixel's area.

The Pearson correlation coefficient (R) between the two datasets is 0.987 for January (**Figure 4**a) and 0.978 for July (**Figure 4**b). Similar results were obtained considering all the pixels with at least 1% of cultivated area. This ensures that no substantial bias emerges from the monthly comparison.

The two ET_0 from HS and PM have also been compared in every cell, grouping the results by climate conditions. **Figure 3** shows the boxplots over agro-climatic zones for the months of January (a) and July (b), according to the GAEZ thermal agro-classification [40]. Zones are obtained on the basis of climate data from CRU-TS [51] according to the indications given by Van Velthuizen et al. [54], and are shown in **Figure 3d.**
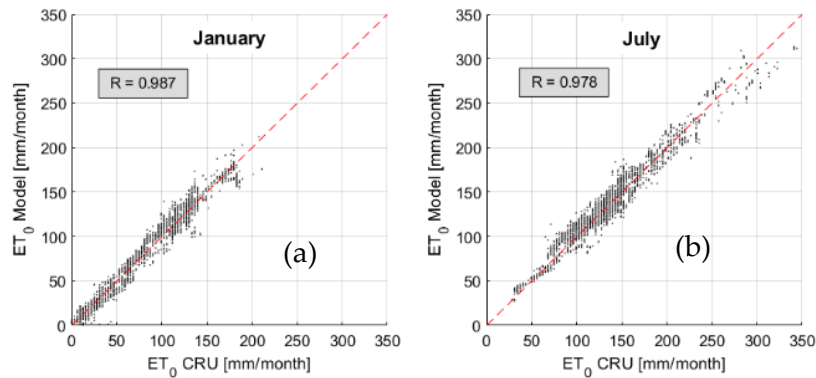
Figure 4. Comparison between the CRU-TS v.4 ET_0 (Penman-Monteith, monthly data) and the monthly average ERA5-based Hargreaves-Samani ET_0. The comparison was made considering all the irrigated cells around the world where the cultivated area is at least 90% of the pixel, for the months of January (**a**) and July (**b**).
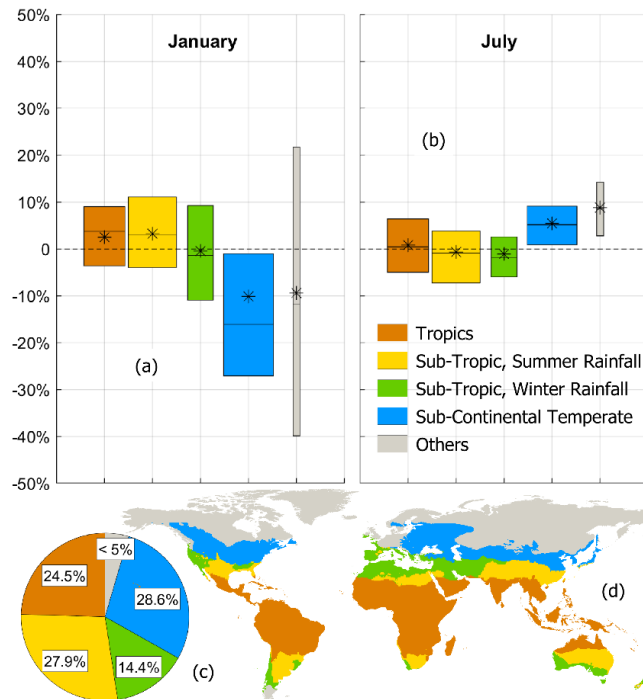
Figure 3. (**a-b**) Boxplots and area-weighted means of percentage differences between monthly ET_0 (Computed HS and PM from CRU-TS). Boxplots show values corresponding to 25%, 50% and 75% of cultivated lands for six climate zones: Tropics (orange), Sub-tropics summer rainfall (yellow), Sub-tropics winter rainfall (green), Temperate sub-continental (blue). The grey boxplot describes the ET_0 alignment over the least irrigated zones: Oceanic Temperate, Continental Temperate, Oceanic Boreal, Sub-Continental Boreal, Continental Boreal, Arctic. The horizontal dimension of the boxplot is proportional to the percentages of irrigated areas per climatic region, reported in the pie chart (**c**). Asterisks: area-weighted means of annual percentage differences. (**d**) GAEZ global agro-climatic classification of surface lands.

The three levels in each boxplot show the percentage differences corresponding to 25%, 50% and 75% of cultivated areas in each climatic zone. The asterisks indicate the area-weighted mean percentage difference. The pie chart in **Figure 3c** shows the percentage of irrigated areas per climate region: tropics (24.5%), sub-tropics summer rainfall (27.9%), sub-tropics winter rainfall (14.4%), temperate sub-continental (28.6%); the sum of areas equipped for irrigation in the oceanic-temperate, continental temperate, boreal and arctic zones are less than 5%. Since 85.5% of total cultivated areas are in the northern hemisphere, in temperate regions January is mostly a winter month: this explains the substantial negative differences found where the HS method is less effective due to low temperatures. On the other hand, HS and PM methods are more aligned on tropical (orange) and sub-tropical regions (beige and yellow). Also the temperate sub-continental region (green), that accounts the largest fraction of temperate areas, shows a good alignment during summer and winter. In summary, except for a few isolated cases on tropical and temperate-continental regions, monthly correlation indices between HS and PM were typically found higher than 0.8. This is consistent with results from previous studies, where HS was found a reliable method on a global scale [55] and also with studies in arid and semi-arid regions where R reaches 0.97 [56].

Although ERA5 provides data of potential evapotranspiration, ET_p (defined as the maximum amount of evaporation, under existing atmospheric conditions, from a surface of pure water), this variable is the result of an energy-balance approach [57] which is conceptually different from ET_0.

Results were compared with this dataset, finding marked local differences, with annual rate of ET_0 computed with HS being up to 25% lower than ET_p, with winter ET_p being too large in central Asia and North America and with unclear low values in some intensively cultivated regions (central France, the Amazon, the Great Lakes region of the U.S., Myanmar, Laos, New Guinea). For these reasons, ET_p is not recommended to be used in the assessment of crop water requirements.

2.5 Method for the estimation of crop water requirements

For assessing irrigation requirements on a global scale, a water balance model has been developed, improving the methodology proposed by Tuninetti et al. [38]. The model calculates the irrigation requirement using a soil-water balance on land equipped for irrigation, taking as input the climatic data and the agricultural information described in the previous paragraphs. The actual evapotranspiration (ET_a) was evaluated for each day, according to the FAO's approach [7], i.e.

$$ET_{a,i} = ET_{0,i} \cdot k_{c,i} \cdot k_{s,i} \, , \qquad (2)$$

where ET_0 and ET_a are expressed in mm/day, i is the specific day, k_c is a dimensionless coefficient specific for each crop and growing phase (or crop coefficient), and k_s is the water stress coefficient, that takes values from 0 to 1.

When k_s=1, the evapotranspiration is not affected by water stress and reaches the maximum rate, named crop evapotranspiration (ET_c). If k_s=0, the crop reaches the wilting point because of the dry soil condition, and there is no evapotranspiration.

The study of Chapagain & Hoekstra [39] provides the crop-specific information to divide the growing period into four phases (initial, crop development, mid-season, late season) and assigning daily crop coefficients. As described by Allen et al. [7], the crop coefficient remains constant during the initial stage ($k_c = k_{c,ini}$). In the development stage, k_c grows linearly from $k_{c,ini}$ to $k_{c,mid}$, i.e. the constant value of the coefficient in the mid-season stage, and finally, in the late season stage, it decreases linearly from $k_{c,mid}$ to $k_{c,end}$. This information is available for the ten different climatic zones summarized in **Figure 3** (based on the GAEZ thermal agro-classification [40]).

The water stress coefficient k_s is calculated according to the FAO methodology [7], i.e.

$$k_{s,i} = \begin{cases} 1 & \text{if } \theta_i \geq (1 - \rho_i)\theta_{fc} \\ \dfrac{\theta_i - \theta_w}{(1 - \rho_i)(\theta_{fc} - \theta_w)} & \text{if } \theta_w < \theta_i < (1 - \rho_i)(\theta_{fc} - \theta_w) \\ 0 & \text{if } \theta_i \leq \theta_w \end{cases} \quad (3)$$

In Equation (3), θ_i is the soil moisture [mm] in day i, calculated multiplying the water content [%] and depth of the root zone [mm]. In the same equation, θ_{fc} and θ_w are the levels of soil moisture [mm] corresponding to field capacity (i.e. the maximum amount of water that can be stored in soil after drainage by gravity action) and wilting point (i.e. the dry soil condition, when crops do not have available water), respectively. The depletion fraction, ρ_i, is the percentage of total available water that can be used by a crop without reaching water stress. The term $(1 - \rho_i)\theta_{fc}$, also known as θ_i^*, is the soil moisture at incipient water stress or stomata closure [mm]. According to the FAO methodology [7], the depletion fraction ρ of day i can be calculated as

$$\rho_i = \rho_{st} + 0.04(5 - ET_{c,i}) , \quad (4)$$

where $ET_{c,i}$ is the crop evapotranspiration in the absence of water stress [mm] and ρ_{st} is a crop-specific standard value of the depletion fraction at $ET_c = 5$ mm/day. This expression is related to the sensitivity of crops to weather conditions, as higher temperatures imply faster stomata closure, in equal soil

moisture conditions. The depletion fraction is found to vary in a range between 0.1 and 0.8.

To apply Equation (3), the 30-arc-sec global dataset of available water capacity was used, i.e. the difference between field capacity and wilting point, from the Harmonized World Soil Database by JRC [58].

We used the data from Allen et al. [7] to set the maximum rooting depths for irrigated lands: roots of temporary crops are supposed to increase linearly in the first two phases of the growing period, from a sowing depth of 0.2 m, and then remain equal to the maximum value for the rest of the season. Roots of perennial crops are supposed equal to the maximum length for the entire year. In this way, the model calculates the actual available water for each day of the growing period.

The daily soil-water balance expresses the variation of soil moisture in the root zone, calculated as a function of inputs and outputs:

$$\theta_{i+1} - \theta_i = P_i + I_i - ET_{a,i} - PS_i \,, \tag{5}$$

In Equation (5), all variables are expressed in mm. θ_i is the soil moisture on day i and ranges between field capacity and wilting point conditions ($\theta_w \leq \theta_i \leq \theta_{fc}$); S_{i+1} is the soil moisture resulting from the daily water balance, used as the initial condition on the following day; P_i is precipitation; and $ET_{a,i}$ is the actual evapotranspiration, calculated according to Equation (2). During dry periods, low rainfall may be insufficient to compensate for evapotranspiration and soil moisture reaches the water stress level (θ^*), the condition in which plants start to close their stomata. The daily irrigation requirement, I_i, is defined as the water needed to avoid water stress, the additional depth that guarantees $\theta_i \geq (1 - \rho_i)\theta_{fc}$ according to equation (3). In the event that daily precipitation brings soil moisture to field capacity, any further input of rainfall that cannot be stored in the soil is called precipitation surplus, PS_i. In Equation (5), this variable represents the sum of runoff and ground percolation. Since irrigated fields are usually almost horizontal, surface runoff and groundwater lateral movements in the root zone were considered negligible: PS_i is assumed equivalent to deep percolation.

On the sowing date of temporary crops, the initial soil moisture is assumed equal to field capacity. For crops grown on paddy fields a specific hypothesis is required: an additional depth of 200 mm is considered to saturate the soil before each sowing date, as suggested by the FAO methodology [59]. This water is not included in the estimation of rice irrigation requirement, because it is not directly used by the plants, and is explicitly reported in the results.

Considering that precipitation may occur in different hours of the day, even during the night when evapotranspiration is negligible, a random assignment of input rainfall was introduced. In fact, the assumption that the stress coefficient (k_s)

is systematically calculated before or after the precipitation occurred may lead to some uncertainties in the assessment of daily ET_a, since the actual daily precipitation rate can be distributed throughout the day. The random assignment can partially this uncertainty, assuming that precipitation may occur in different moments of the day.

The model evaluates the irrigation requirement for each growing season in a cell. If a crop is repeatedly cultivated on the same field, the final amount of I is the sum made for all seasons. Instead, if the same crop is cultivated on different fields within the same cell, the final I for that crop is the area-weighted average between the two requirements. The total volume of irrigation requirement is calculated on a monthly or annual scale, considering the contribution of the 26 crops, as

$$V = 10 \sum_{c=1}^{26}(I_c \cdot AEI_c), \tag{6}$$

where V, I_c and AEI_c are, the total irrigation requirement volume [m³], the irrigation requirement [mm] (calculated according to Equation 5) and the irrigated area [ha] for a specific crop c, respectively.

The averaged requirement considering the entire area of a cell is $I_{grid} = \frac{V}{(10A_{grid})}$, computed as the ratio between the total volume [m³] of irrigation requirement and the area A_{grid} [ha] of the 0.0833° grid cell: this is used here to compare irrigation requirements from different regions in the world. The spatial variability of I_{grid} values is consistent with the actual distribution of irrigated areas and cropping intensities within cells.

2.6 Crop irrigation requirements for year 2000

2.6.1 Global spatial variability

The model described above was applied using the climatic and agricultural data of year 2000, and the global volume of irrigation requirement was estimated in 962 km³. **Figure 5a** shows the spatial distribution of annual cell-averaged requirements (I_{grid}) and **Figure 5b** also shows the spatial distribution of cell-averaged precipitation surplus (PS). Factors influencing the I_{grid} are the ratio between annual precipitation and the reference evapotranspiration (i.e. the Budyko index), the temporal variability of these forcings (even in wet regions a significant amount of irrigation may be required if the precipitation is strictly seasonal), and the extension of AEI in each pixel of the grid.
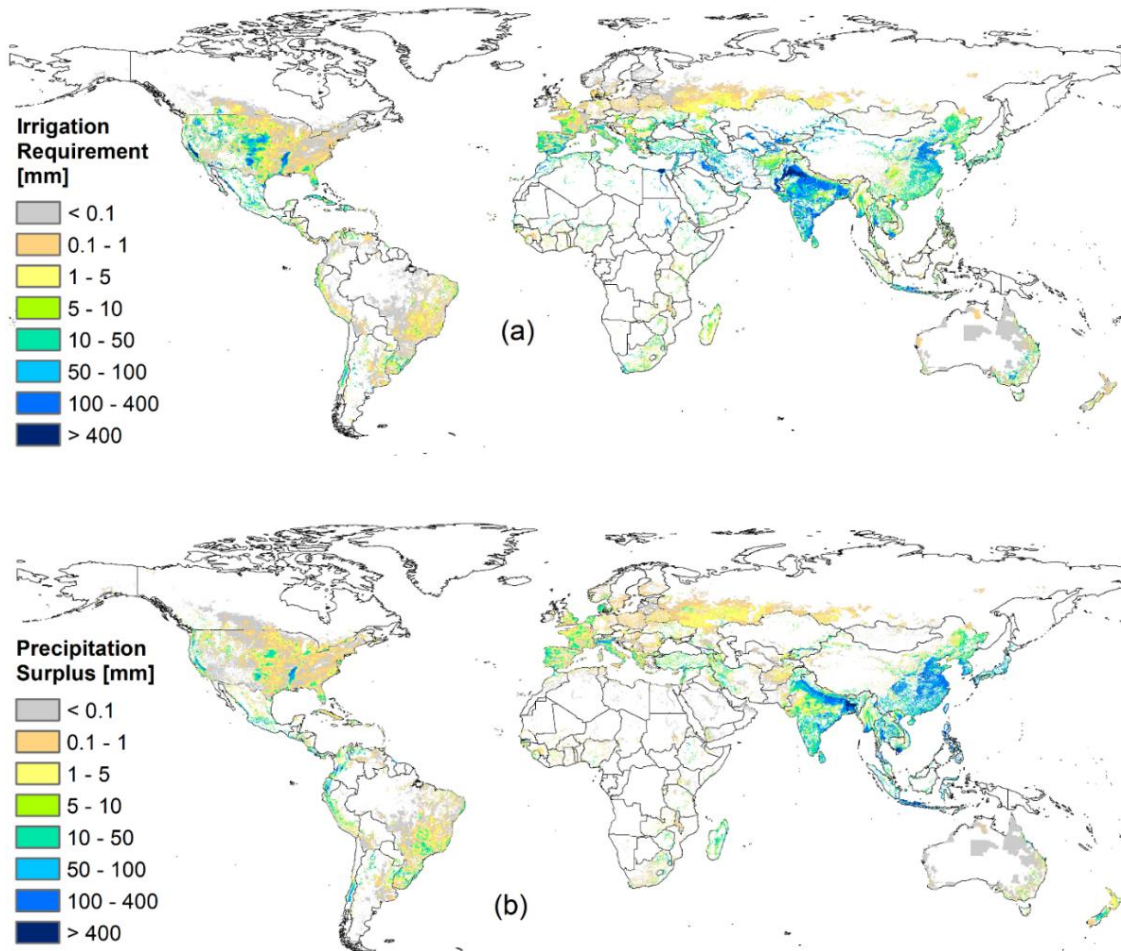
Figure 5. Spatial distribution of irrigation requirement and precipitation surplus. Cell-average water depths [mm], as a ratio between the total volume cumulated over the year within the cell and the cell area.

For example, in Bangladesh the Budyko index is 1.5 but the high rainfall rate is concentrated in the monsoon season, and the tropical high evapotranspiration quickly leads crops to water stress during dry periods: so, high Igrid values were found. In the central and northern parts of Australia, the irrigation requirement is typically higher than 900 mm/year, but the very low density of cultivated areas keeps the cell average Igrid below 1 mm/year (in this region, less than 0.1% of the territory is usually equipped for irrigation).

In arid and semi-arid regions, high Igrid values were found (e.g., over 750 mm/year in the Indo basin, over 800 mm/year in the Nile delta and over 720 mm/year in California) and negligible precipitation surplus due to the lack of precipitation. In many European and American temperate regions, high Igrid levels usually depend more on AEI density and crop types than on climate

conditions. For instance, Italy's northern Po Valley requires much more irrigation than southern territories: despite south of Italy is typically drier, northern high rates depend on the density of cultivated areas (especially rice paddies).

The global precipitation surplus (*PS*) over irrigated lands was found as 672 km^3 and the spatial distribution of *PS*$_{grid}$ is shown in **Figure 5b**. Although *PS* is a "water loss" for the water balance of the root zone, it has an important role in the hydrological cycle and ecosystem functioning. This rainfall water is not used by the crops, but it is an important source of recharge for aquifers. Moreover, PS may be an important water resource in those areas where rainfed agriculture is still the most common practice, especially where the seasonal regime of rainfall concentrate the precipitation in limited periods of the year. For example, Castejón-Porcel et al. [60] highlighted the importance of the runoff from agricultural fields in the semi-arid region of Campo de Cartagena (Region of Murcia, Spain), especially considering future changes in the seasonal availability of precipitation.

The precipitation surplus is not just a potential source of water resource, but its potential negative impact for the local agriculture must be taken into account. In fact, in those regions with "critical" runoff periods (for example, the south Asia during the Monsoon period), the precipitation surplus may lead to a loss of sediments, nutrients and other agro-chemicals from croplands: this process has the double negative effect of reducing the fertility of crop fields and deteriorate the water quality [61].

The comparison of national estimates (i.e. the sum of *I* and *PS* volumes from equation (5) over national areas) shows that 171 countries in the world require irrigation, and in 106 of them the *PS* volume is higher than *I*. If part of this precipitation surplus could be stored and used during the growing season, this would lead to a significant decrease in water withdrawals. For example, the irrigation required by China was estimated to the second highest in the world (130 km^3/year) and even a higher precipitation surplus (193 km^3/year); in theory, it could be possible to satisfy all the Chinese irrigation requirements by using annual precipitation on AEI.

Despite the apparent similarity between **Figure 5a** and **Figure 5b**, a low annual correlation between irrigation requirement and precipitation surplus was found: the Pearson correlation coefficient (R) between *I*$_{grid}$ and *PS*$_{grid}$ is 0.38 (as shown in **Figure 6b**). An even lower correlation was found comparing the annual distribution of *I* and *PS* (water depths over AEI) for which $R = -0.16$ (**Figure 6a**): the higher correlation between *I*$_{grid}$ and *PS*$_{grid}$ is due to their common dependence on irrigated areas and cropping intensities. On a monthly scale, where the variability of *P* and *ET$_0$* is more important, higher correlations between *I* and *PS* were found (e.g. R$_{July}$ = -0.29 and R$_{December}$ = -0.20).
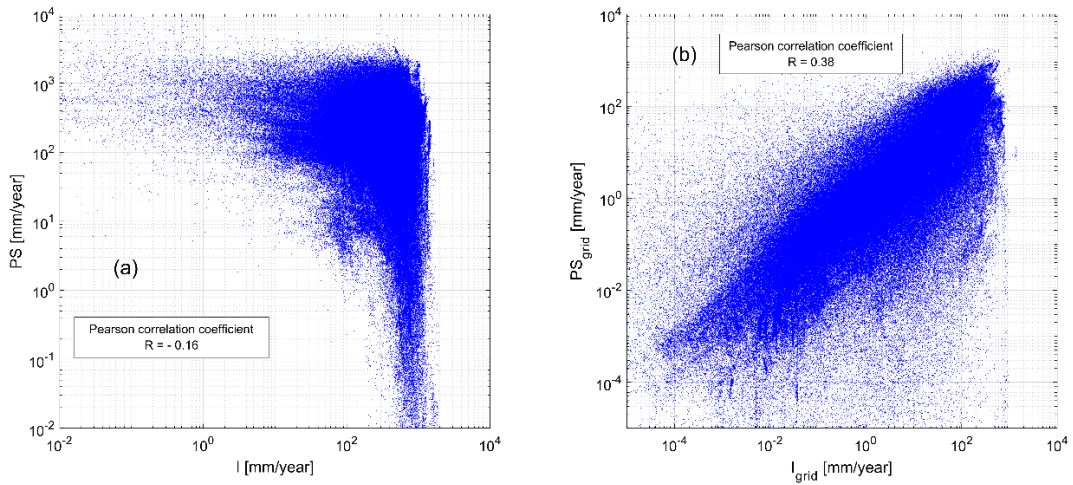
Figure 6. Correlation between annual irrigation requirements and precipitation surplus [mm/year]. (**a**) Pearson correlation coefficient between *I* and *PS* (irrigation requirement and precipitation surplus annual rates over irrigated croplands); (**b**) Pearson correlation coefficient between annual I_{grid} and PS_{grid} (average irrigation requirement and precipitation surplus, considering the total area of the MIRCA2000 grid pixels).

2.6.2 Crop-specific requirements and monthly variability

In considering individual crops, it is significant that, according to FAOSTAT, more than 48% of total agricultural production in tonnes in year 2000 included only four crops: sugar cane, rice, wheat and maize. The irrigation required by these four was 58% of the global estimation. Rice's requirement is the largest, nearly 30% of total. This is mainly because of the huge extension of paddies, the high cropping intensity, i.e. the fraction of the arable area that is cultivated [7] which may exceed 1 on those croplands where more than one growing season occurs each year, and the high sensitivity of rice to soil moisture depletion (e.g., in Uttar Pradesh, Haryana and Punjab in northern India, there are three consecutive growing seasons of rice per year). Paddies are artificially maintained at a high moisture level, and field capacity is frequently reached even with weak precipitation, with a consequent major loss of *PS* during rainfall events in the growing period. **Table 7** summarizes our findings on the crop-specific results, classifying them by the extent of irrigated areas from MIRCA2000.

Figure 7 shows the temporal distribution of crop-specific volumes of irrigation requirements for year 2000, calculated according to Equation (6) and cumulated at monthly scale. The largest volume is required from June to September, mainly because most of the summer crops are cultivated in the northern hemisphere (e.g. 90% of maize *I* is required during these four months).

47

Table 7. Crop-related summary of estimations and irrigated areas. *I*: Irrigation requirement; *PS*: Precipitation surplus; AEI: Areas equipped for irrigation; CI: cropping intensity, i.e., the fraction of the arable area that is cultivated (CI>1 for crops cultivated more than once per year on the same fields, like rice in northern India). Rice's requirement does not include additional amounts of water to saturate the fields before sowing (globally 206.2 km^3).

CROP	I [km^3]	PS [km^3]	AEI [10^3 ha]	CI
Rice	271.4	360.1	1'031	1.6
Wheat	153.1	44.3	666	1.1
Maize	66	48.7	299	1
Others annual	51.8	19.8	201	1.2
Cotton	73.3	21.2	162	1
Others perennial	80	48.5	129	1
Fodder grasses	71.8	14.5	116	1
Sugar cane	71.7	50.9	101	1
Soybean	16.6	15.3	60	1
Pulses	18	2.8	55	1
Barley	7.3	4.1	46	1
Potato	12.4	5.8	37	1
Groundnuts	7.5	9.6	36	1
Citrus	15.1	12.2	35	1
Rape seed	6.7	0.5	34	1
Sorghum	8	3.4	34	1
Millet	3.5	1.9	17	1
Grapes	7.4	4	17	1
Sugar beets	6.1	0.89	16	1
Sunflower	3.6	1.8	13	1
Date palm	8.4	0.14	7.2	1
Rye	0.74	0.68	4.4	1
Coffee	0.67	0.83	1.7	1
Cocoa	0.01	0.06	0.13	1
Cassava	0.02	0.03	0.11	1
Oil palm	0.04	0.11	0.11	1

In contrast with other seasonal crops, wheat is massively cultivated during winter and spring, and requires more irrigation from December to May. For example, more than 46% of wheat AEI are in India and Pakistan, where this crop is mainly cultivated from November to May and most of the rainfall occurs in the summer. Winter wheat is also largely cultivated in Europe, U.S. and China, and is usually planted between October and December. In contrast, in the northern part of India (e.g., Punjab) wheat is mainly cultivated from June to November as well as in southern Europe and in the US Northwest. The monthly volumes of irrigation required by rice, wheat and cotton are well aligned with results from the GCWM model, described by Siebert & Döll [33], even if lower values of total irrigation requirement in spring months were found.
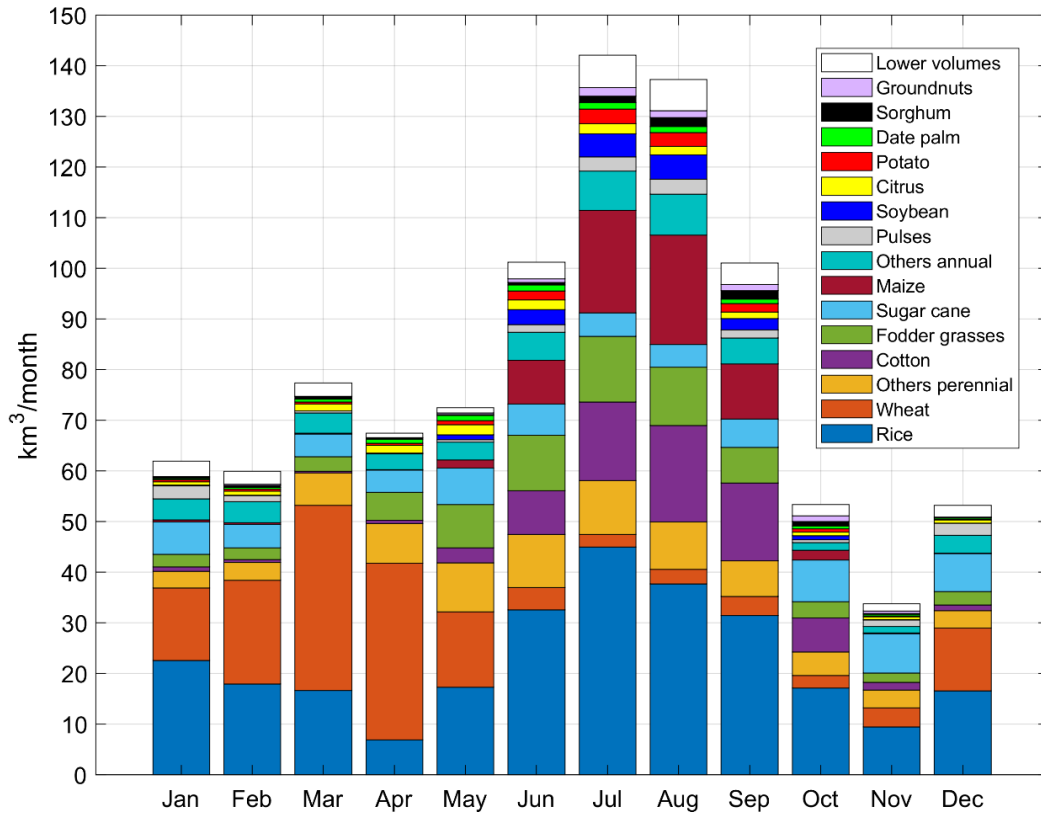
Figure 7. Monthly volumes of crop-specific irrigation requirement [km³/month]. Rice volumes refer only to the evapotranspiration requirement.

2.6.3 Regional focuses on three intensive areas

To better explore the spatial variability of results and to verify the ability of the model to provide estimates for various climate scenarios, the monthly water balance on three intensively cultivated regions has been analyzed in more detail. These are: Central Valley (CV, California), Po Valley (PV, Italy) and Punjab (PU, India), belonging respectively to sub-tropic winter rainfall, temperate sub-continental and sub-tropic winter rainfall climatic zones. The three areas have similar geographical extents (about 52000 km², 47000 km² and 50000 km² respectively), but heterogeneous portions of areas equipped for irrigation (42%, 32% and 72% respectively). **Figure 8** shows the monthly variability of the main water-balance terms, i.e. the climate variables (P and ET_0), the area-weighted values of irrigation requirements, and precipitation surplus.

The cumulative volumes of I and PS are also shown (on the right axes). In the lower part of each panel, the bar graphs show the monthly distribution of AEI by actual cultivated crops.
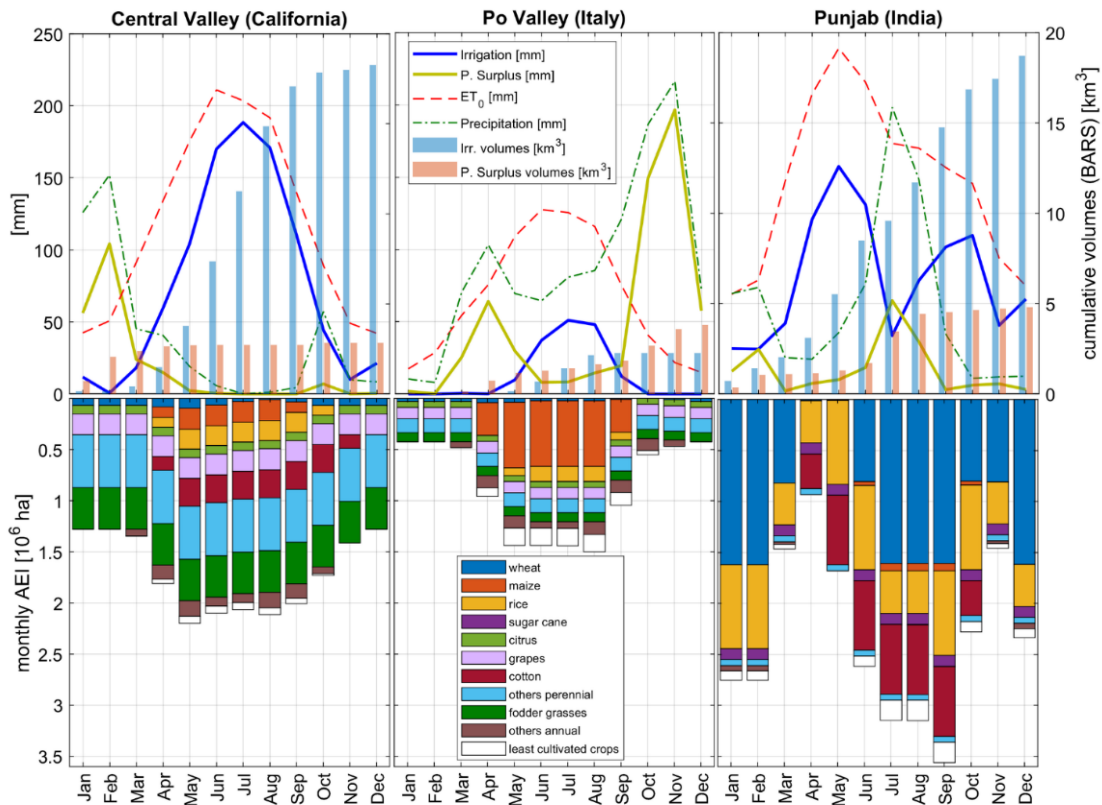
Figure 8. Monthly variability of climate forcings and model results, over three intensively cultivated areas. The selected regions belong to different agro-climatic zones: Central Valley (California, sub-tropic winter rainfall), Po Valley (Italy, temperate sub-continental) and Punjab (India, sub-tropic summer rainfall). The variables on both the axes have been quantified considering the monthly cultivated AEI, as shown in the lowest part of the plots.

CV is mainly cultivated with perennial crops (23% of total AEI), fodder grasses (18%), grapes (9%) and cotton (12%); PV has maize (43%) and rice (10%) in the warm season and perennial crops over the entire year (9%); PU is mainly cultivated with wheat (45%), rice (23%) and cotton (19%).

Irrigation requirements of CV and PU are comparable (19.0 km³ and 20.6 km³ respectively) but monthly values are very different, mainly because of the difference in precipitation and evapotranspiration rates. In California, the maximum irrigation requirement is close to 190 mm for the month of July due to the combination of high ET_0 and very low precipitation. In this region, all the water surplus is concentrated in the winter months, with a maximum of 105 mm in February, while the high evapotranspiration rates of warm months (e.g. over 150 mm/month in all the summer period) maximize the irrigation requirement. The Po Valley average reference evapotranspiration is lower and precipitation is higher than in CV and PU, due to the temperate climate. *I* reaches 50 mm only in July: a

short period if compared with five months in California and six in Punjab. Almost no irrigation is required in Po Valley from October to April, due to the combined effect of high rainfall and low ET_0. In this area, the irrigation requirement is mainly concentrated in the summer period, but it only reaches 2.2 km^3 (a small volume, compared with CV and PU). Annual water surplus over PV is 3.8 km^3, a huge volume if compared with the two other regions, but this surplus is mainly concentrated in the October-November period. In fact, in year 2000 Po Valley was afflicted by an intense flood event in November, so the high water surplus can be assumed as strongly related to that specific event.

2.6.4 Classification over water-stressed areas

Additional insights from the results can be gained by grouping the volumes of irrigation requirement according to the classes of agricultural water risk described in the Water Risk Framework, published by the Water Resources Institute [62]. This framework includes a global dataset of water risk indices (referring to the 1960-2014 period), combining indicators of physical risk, water quality and regulatory aspects for several human activities. The "Agricultural Water Risks" was used to classify the irrigation requirements assessed by our model.

Figure 9 shows the distribution of irrigation requirement volumes by classes of agricultural water risk: a high risk means that the requirement volume may be hard to satisfy. Irrigation water could be unavailable (quantitative risk) or polluted (qualitative risk), and this may be critical for crops.

Only 1.2% of global *I* volume falls within the low-risk class, mainly required in North America and Oceania. Unfortunately, 44.5% of irrigation requirement is exposed to a medium-high risk, and 28.4% to a high or extremely high risk.

Southern Asia is the most exposed area to agricultural water risk: most of the irrigation required in this region (about 25% of global *I*) falls into the medium-high, high and extremely high-risk classes. This is due to the fact that India and Pakistan are two of the most productive countries, with two of the most water requiring agricultural systems.

About 87% of North American *I* is affected by low and medium risk, with western states (e.g. California) being more exposed to quantity and quality limitations than are the central and eastern regions. In North Africa, agricultural areas along big rivers are less exposed by risk (e.g. the Nile delta) while the small fraction of croplands in the arid and semi-arid territory is exposed to medium or high risk. The largest part of European irrigation requirement is exposed to medium risk, but the nature of the risk is different depending on the climate region (e.g. Po Valley is more exposed to quality-related risk, while Spain and southern Italy to quantity-related risk).
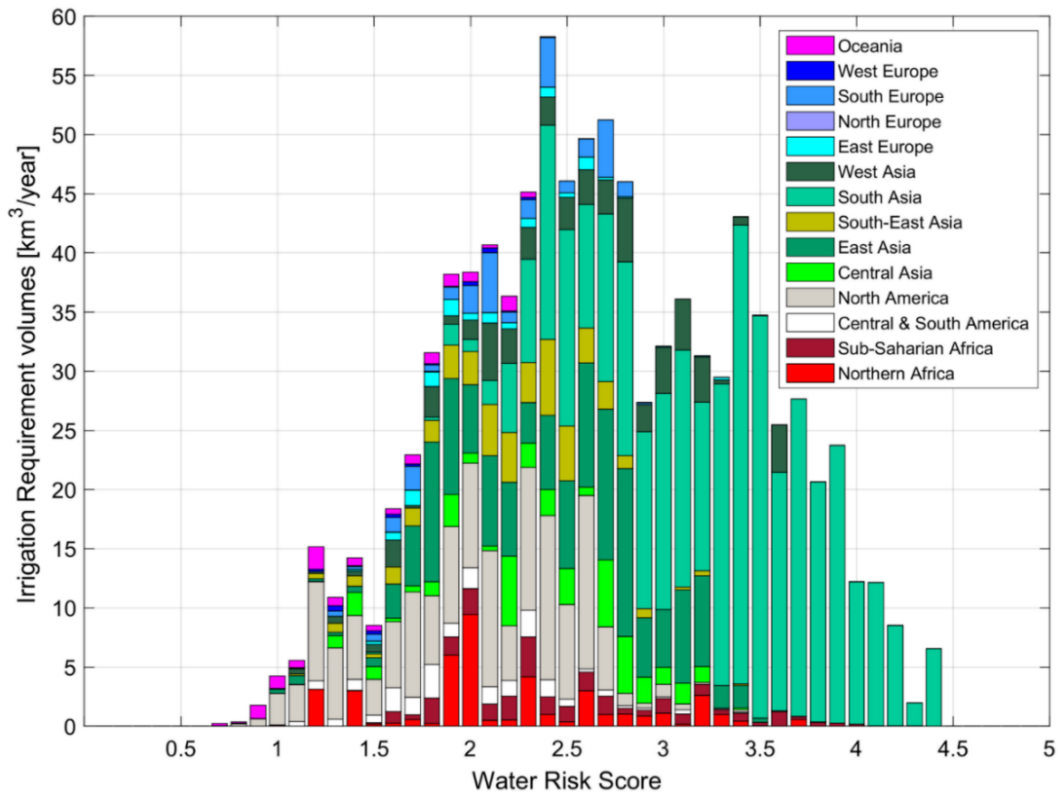
Figure 9. Distribution of irrigation requirement volumes by classes of Agricultural Water Risk. Classification of the World Resources Institute: Low risk (0-1), Low-Medium risk (1-2), Medium-High risk (2-3), High risk (3-4), Extremely High risk (4-5).

2.7 Comparison with previous estimations and national data

In comparing the results of this study with previous assessments, one must take into account that all global assessments are affected by some uncertainty. The quality of input data, spatial and temporal resolution, modelling assumptions such as the length and number of growing seasons or the classification of some crops in macro-categories (e.g. "others annual") play an important role in the assessment of irrigation requirements. In this study, a part of the uncertainty is reduced using a model based on actual daily data of precipitation and temperature.

Table 8 shows a comparison of irrigation requirement results from the global models introduced in **Table 4**. The comparison points out the alignment of our estimation to the literature and how much the improvement of the input detail affects the final result.

Table 8. Comparison of global estimations of irrigation requirements. (i) Estimates based on Penman-Monteith reference evapotranspiration. (ii) and (iii) Estimates from two approaches based on Priestley-Taylor reference evapotranspiration.

	Assessment	I [km³/year]
[28]	Rolle et al. (2021)	962
[36]	Chiarelli et al. (2020)	1068
[35]	Mekonnen & Hoekstra (2011)	899
[34]	Liu & Yang (2010)	927
[33]	Siebert & Döll (2010)	1180 [i], 1448[ii], 1145[iii]
[32]	Hanasaki et al. (2008)	1320
[31]	Rost et al. (2008)	1364
[30]	De Fraiture (2007)	1450
[29]	Döll et al. (2002)	1091.5

The estimate from this study is well aligned with most of the previous works, especially with assessments based on the MIRCA2000 dataset. The differences between the latest models may have several causes: the use of different climate datasets, the modelling approach for the crop growth (e.g. Siebert & Döll [33] use average global values of crop coefficients, neglecting climate-related differences) and the initial soil moisture conditions (e.g. Chiarelli et al. [36] performed a sensitivity analysis assuming three different scenarios to simulate the initial moisture condition on the sowing date). The GCWM model [33] from Siebert & Döll provides three results, obtained using different methods to estimate the reference evapotranspiration: 1180 km³/year using Penman-Monteith and two results using different alternatives of the Priestley-Taylor method (1448 km³/year and 1145 km³/year). The estimate from the H07 [32] model (1320 km³/year) was reported by Siebert & Döll [33], and refers to the 1986-1995 period.

Compared to later studies, the older models seem to overestimate the irrigation requirement. This is probably due to the fact that most of these models were not based on crop-specific data of irrigated areas and growing calendars, so the assessments were performed with a larger number of assumptions, using average values to model the crop development. For example, Döll et al. (2002) performed the assessment classifying rice paddies separately and aggregating all the other crops [29].

2.7.1 Comparison with national withdrawals for agriculture

Model results, in terms of irrigation requirement volumes, have been cumulated at the national scale and compared with data of agricultural withdrawal (*W*) for the year 2000, provided by AQUASTAT [59] and by the Organization for Economic Co-operation and Development (OECD) [63]. The national withdrawals for irrigation are the volumes of water taken from surface

water bodies or groundwater to be used in agriculture, in fields equipped for irrigation. Withdrawals include the volumes required by crops and the water losses due to inefficiencies in the distribution and irrigation systems.

The ratio between *I* and *W* can be reasonably associated with a national mean irrigation efficiency (*E*), defined as the ratio between the amount of water withdrawn for agricultural purposes and the theoretical volume required by crops. The irrigation requirements are equal to withdrawals in the ideal condition of maximum efficiency (no water losses in the irrigation system) and absence of water stress during the growing season. In the real systems withdrawals are generally higher than requirements. The comparison between these two volumes is important to validate our estimations: the difference between *I* and *W* may depend on the technological level of the country, on the cultivated crops (e.g. the irrigation efficiency of rice paddies is generally very low) and on the availability of freshwater.

Figure 10 shows the logarithmic scatter plot of the 81 national withdrawals and requirement volumes. Nations are grouped by classes of efficiency, delimited by dotted, dashed and continuous lines: 45 nations lie between 0.1 and 0.5 and 18 nations between 0.5 and 1. More than 80% of required volumes belong to nations within these ranges (54% belongs to nations with efficiency between 0.1 and 0.5). India, China and the U.S. are the countries with higher irrigation requirement: 25.4%, 13.5% and 12.0% of global irrigation volumes, *I*, respectively. Spain is the European country with the highest irrigation requirement (15.7 km^3/year, near 1.6% of global *I*).

For 12 countries, the irrigation efficiencies were estimated to be lower than 0.1: in most of these countries the irrigation water volumes are very small, due to the lack of irrigated lands. Japan appears to have a surprisingly low efficiency (0.06), considering its economic and technological levels, but this may be a consequence of a massive presence of rice paddies (about 54% of total cultivated areas, according to FAOSTAT) which have a very low irrigation efficiency: Döll et al. [29] assume an irrigation efficiency for rice lower than 0.1.

For 6 nations the mean efficiency is higher than 1 (irrigation requirement higher than agricultural withdrawals), e.g. United Kingdom (1.4), United Arab Emirates (1.5), Czech Republic (4.5). Withdrawals lower than requirements in nations with high water-demand states like United Arab Emirates may be due to deficit irrigation practices, in which a provision of lower water volumes than actual requirements are due to lack of water availability [64]. Results are consistent with the efficiencies estimated by Siebert & Döll [65], with similarities in some critical nations (e.g. they obtain *E* = 2.55 in Czech Rep. and *E* = 1.79 in UK). In some of these nations, high efficiency values may be due to the low magnitude of irrigation requirement and withdrawals.
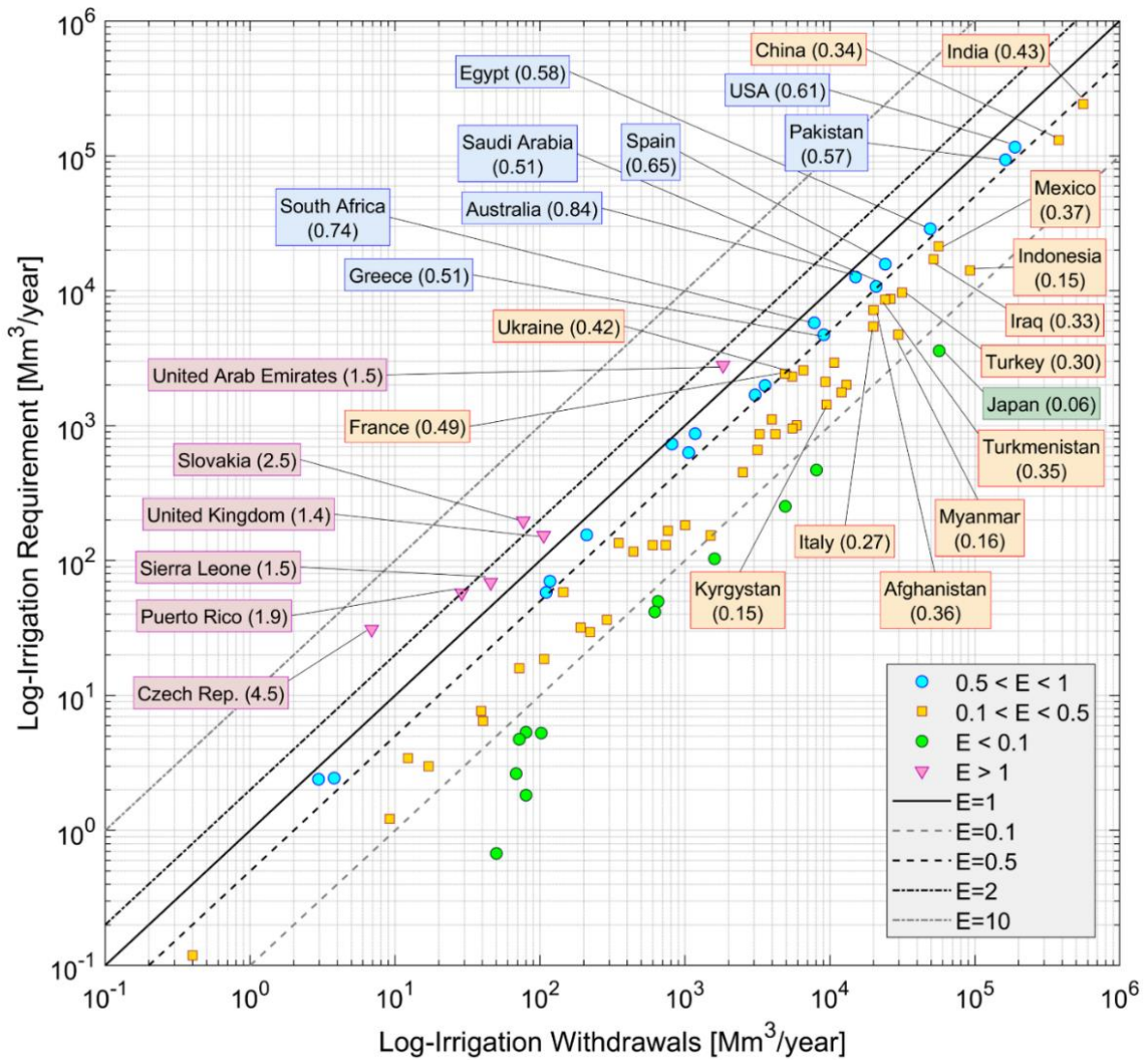
Figure 10. Comparison of national irrigation requirements and withdrawals and aggregation by classes of national efficiency. Blue circles, red crosses and green squares are countries where the irrigation requirement was estimated to be lower than the actual withdrawals for irrigation (*I<W*), grouped by classes of mean national irrigation efficiencies (*E*). Purple triangles are countries for which the model estimates *I* higher than actual *W*. The bold continuous line indicated the condition of *I=W*; classes of efficiencies lower than 1 are limited by dashed lines, while the two dotted lines delimit classes of efficiencies higher than 1. For *E<1*, the labeled countries have at least 106 ha of areas equipped for irrigation.

2.7.2 Comparison with U.S. sub-national estimations

A more detailed validation of the model has been done using data from the United States of America (U.S.), for which the Geological Survey (USGS) provides local information about withdrawals for irrigation in year 2000 [66]. Irrigated lands are more concentrated in the western U.S., especially in the Central Valley of California, in Idaho and other northwestern states, but also in Nebraska and Arkansas (concentrated in the Mississippi region). According to this dataset, the U.S. withdrawal for irrigation was 196.4 km^3 in year 2000. Building a weighted linear regression between the observed withdrawals and the irrigation requirements in each U.S. state (using AEI, i.e. Areas Equipped for Irrigation, as weight), an angular coefficient was estimated (i.e. the expression of the overall irrigation efficiency) of 0.58 (as shown in **Figure 11**). This result is comparable with the value of 0.6 provided by Döll et al. with the same procedure [29].
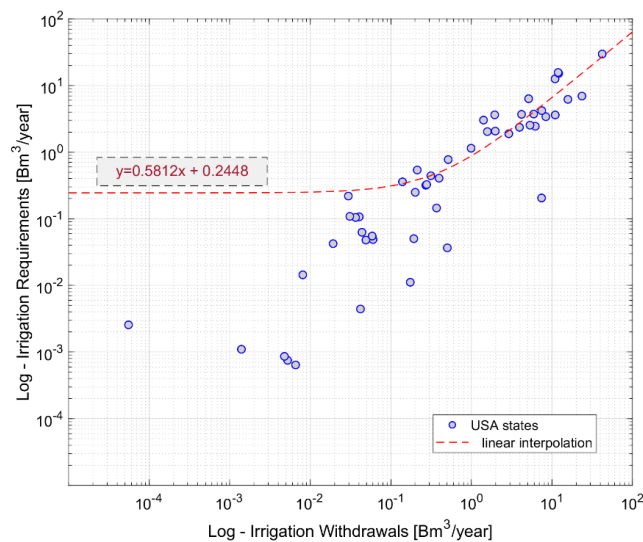
Figure 11. Comparison of withdrawals for irrigation and irrigation requirements [Bm^3/year] for the U.S. states. The weighted linear regression (built using the AEI of each state as weight) shows an angular coefficient of 0.58, which can be assumed as average U.S. irrigation efficiency.

California is the U.S. state with the largest extension of AEI, and presents an irrigation efficiency of 0.64 (higher than the average value of United States). **Figure 12** shows the comparison between our crop-specific estimates of irrigation requirement (*I*) and the data of applied irrigation water (*AW*), which is the volume of withdrawn water that is actually delivered to the crop fields. This information is available for seven crops, provided by the California Department of Water Resources (CDWR) for year 2000 [67]. Rice is the crop with the largest difference between *I* and *AW*, and this is consistent with the low efficiency associated to

paddies. The same dataset also provides estimates of the crop-specific irrigation requirements in California. The model was validated by comparing our results with the estimates from the CDWR (*I_{CDWR}*), as shown in **Figure 12**.
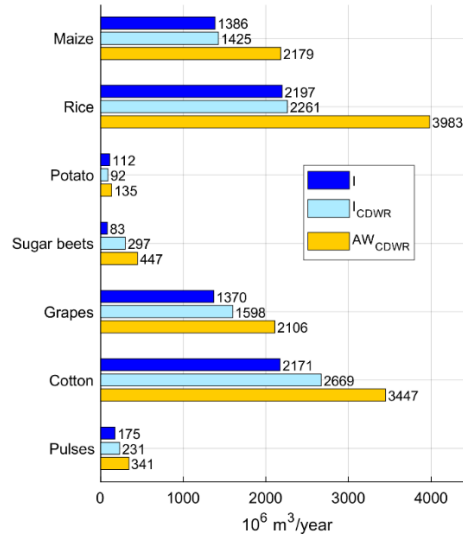
Figure 12. State of California: comparison between crop-specific irrigation requirement estimations (*I*), the irrigation requirements estimated by the California Department of Water Resources (*I_{CDWR}*) and the data of applied water also provided by the CDWR (*AW_{CDWR}*). The *AW_{CDWR}* and *I_{CDWR}* data refer to year 2000.

The irrigation requirements obtained in this thesis are well aligned with the *I_{CDWR}*: for example, were found results for maize, rice and grapes corresponding to 98.0%, 94.5% and 93.7% of *I_{CDWR}* estimations respectively. Large differences between *I* and *I_{CDWR}* volumes for cotton and sugar beets are consistent with the differences of cropland extent between CDWR and MIRCA2000. The ratio between AEI from MIRCA2000 and CDWR is 0.27 for sugar beets and 0.73 for cotton, and the ratios between *I* and *I_{CDWR}* are 0.29 and 0.85 respectively.

Unfortunately, the other crop-specific information available in California are grouped into categories (e.g. fruits or vegetables) that do not match the MIRCA2000 dataset, thus further comparisons cannot be performed.

2.8 Concluding remarks

In this Chapter, a model for the assessment of global irrigation requirement is presented. The analysis is based on the high-resolution dataset ERA5 from the Copernicus Climate Data Store. The model assesses the minimum irrigation required to avoid water stress, working on a daily soil water balance and modelling the crop development according to the FAO methodology, limiting

uncertainties related to climate-forcing data by using satellite information. The reference evapotranspiration is calculated following the Hargreaves-Samani method, which requires only information about surface temperature and solar radiation, fitting very well when compared to more complex and data-intensive methods like Penman-Monteith.

The model was used to assess the irrigation requirements for 26 crops in the world, working on crop-specific agricultural areas equipped for irrigation, while the focus on year 2000 is motivated by agricultural data availability permitting comparison of results with previous studies, many of which were focused on that year. Due to the difficulties in simulating crop development on a global scale in many different climatic, technological and cultural scenarios, the main uncertainty remains the correct modelling of the length of growing periods.

The global volume of irrigation requirement for year 2000 was found to be about 962 km^3, which is an amount comparable both with results from models driven by long-term climate data and from models working with monthly time series. The spatial distribution of irrigation requirements (0.0833°) points out their dependency on the extension of local areas equipped for irrigation, the crop intensity and the kind of crop cultivated, as well as the lack of precipitation during growing periods. The model also estimates that an important amount of rainfall occurring along the growing seasons is lost as surplus over irrigated lands (672 km^3, about 68% of irrigation requirement), mainly motivated by the seasonal variability of precipitation.

The comparison between irrigation requirements and national data of agricultural water withdrawals shows a good agreement between the two variables, with reasonable values of irrigation efficiencies. The model has been validated through a comparison between crop-specific estimations of irrigation requirements and data provided by the California Department of Water Resources, which highlights a very good fitting.

The classification of irrigation requirements by classes of agricultural water risk shows that most of the requirement in South and East Asia is exposed to high and very high risk of not being satisfied, due to possible unavailability of irrigation water in terms of quantity and quality. The global estimation described in this thesis is a first step of a wider project of irrigation assessment, in which the temporal variability and the use of additional data from remote sensing are foreseen.

Chapter 3

Temporal trends in global agriculture requirements

The work described in this Chapter has been partially derived from paper [68].

The temporal variability of crop water requirement is a key topic in the study of climate effects and adaptation strategies. The Agricultural Model Intercomparison and Improvement Project (AgMIP) [69], for example, tested different available models in the production of future climate scenarios for agriculture at the global scale with 0.5° grid resolution. Other few works analyzed the climate-driven changes of crop evapotranspiration in the recent past. Ruane et al. [70] examined the performance of different climate datasets in agricultural large-scale models within the AgMIP project, considering four crop types and different combinations of climate forcings/crop gridded datasets. Recently, Chiarelli et al. [36] estimated the global water requirements for years 2000 and 2016, providing monthly crop-specific results. Other studies focused on national or subnational scales, e.g. the assessment by Yin et al. [71] applied to China from 1982 to 2015. In this work, the model described in Chapter 2 was used to perform a global assessment of agricultural water needs, in order to reduce the lack of studies based on EO-information retrieving daily estimates of crop requirements.

In this Chapter, the coupled soil water balance and crop growth model described in Chapter 2 has been used to estimate the daily actual evapotranspiration of 26 main crops for five decades, in order to highlight significant trends of water needs. The daily scale enables the quantification of the effects of hydro-climatic fluctuations on the timing and duration of water-stressed periods. In this thesis, the information on rainfed and irrigated cropland areas is fixed in time, allowing to focus on the temporal variability of hydro-climatic drivers alone. Consequently, the variables analyzed are, as much as possible, not dependent on the extent of the cultivated areas per pixel, e.g., water depths are considered rather than volumes. The estimation of the temporal evolution of water volumes, which requires the knowledge of cultivated and irrigated areas per crop in time, is beyond the scopes of this thesis.

3.1 Estimation of multi-decade agricultural water requirements

The assessment of crop water requirements from 1970 to 2019 is based on the methodology described in Chapter 2. However, in this Chapter are described the improvements that were introduced to calibrate the reference evapotranspiration over a multi decade period, and the method used to set the initial condition at the sowing day based on EO data.

The methods used to model the crop growth and to calculate the daily water requirements were presented and discussed in Chapter 2.5.

3.1.1 Daily climate data

The model runs at a daily time step using precipitation (P) and reference evapotranspiration (ET_0), defined as the evapotranspiration from an ideal well-watered grass surface [7], to compute the soil water balance and to assess the crop actual evapotranspiration. The simulation covers the period 1970-2019 and is based on the climate data from ERA5, i.e. the global reanalysis dataset produced by the European Centre for Medium-Range Weather Forecast (ECMWF) within the Copernicus Climate Change Service (C3S) [72] [73]. The reanalysis uses the information from ground measurements and the global satellite network, exploiting the growing availability of remote sensors over the last two decades [74].

Although ERA5 includes results since 1950, the present analysis starts in 1970 in order to avoid uncertainties related to previous periods [75]. The climate data were downloaded at the original resolution of 0.25° (about 30 km at the Equator) and processed with the Climate Data Operators (CDO) [76] to match the MIRCA2000 grid. The CDO tool offers specific methods of interpolation to redefine the resolution of each climate variable.

As previously described in Chapter 2, daily precipitation was calculated by summing hourly rainfall from 1:00 am to 0:00 am in each day, from 1970 to 2019. In **Figure 13**, the mean annual precipitation rates from ERA5 [mm/day] for the 2010-2019 decade are shown, as well as the percentage variations with respect to the 1970-1979 average annual rates.
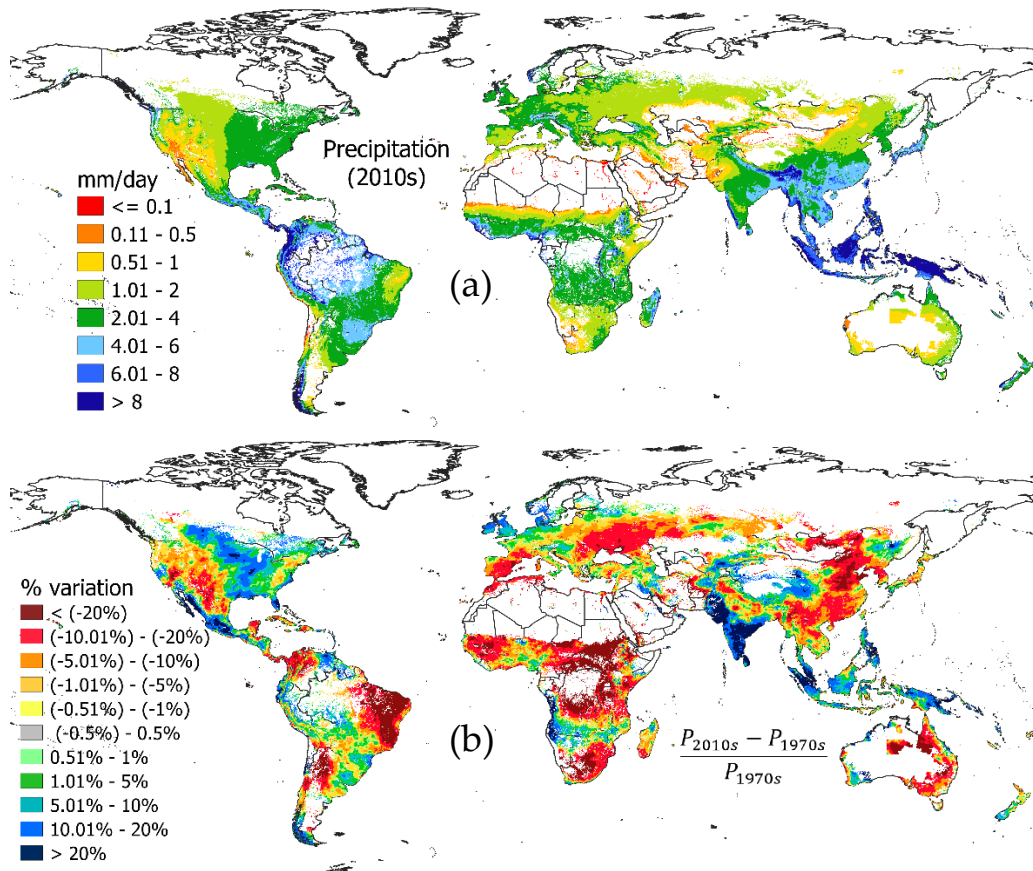
Figure 13. (**a**) Global map of mean precipitation rates [mm/day] over croplands, calculated as average values for the 2010-2019 decade. (**b**) Percentage variations of the mean daily precipitation rates, comparing the 2010-2019 and 1970-1979 decades; blue-green areas: P_{2010s} > P_{1970s}; yellow-red areas: P_{2010s} < P_{1970s}; grey areas: very low variations between the two decades (<0.5%).

According to the procedure described in Chapter 2, the daily reference evapotranspiration, $ET_{0,i}$ (in mm/day), was calculated using the Hargreaves-Samani method, according to Equation (1). Although Hargreaves-Samani is one of the methods suggested by FAO to calculate ET_0 [7], the empirical coefficient k_{HS} in Equation (1) was calibrated for each pixel, in order to reproduce annual values of $ET_{0,i}$ available from a reference application of the Penman-Monteith method.

Considering that the procedure from Chapter 2 was used to calculate ET_0 only for year 2000, a methodological improvement was introduced in order to calibrate the empirical coefficient of HS from Equation 1 (k_{HS}) taking into account the climate variability over 50-years period. The CRU Time-Series global data [51], previously introduced in Chapter 2, was used to calculate the annual deviations between the ET_0 from Hargreaves-Samani and Penman-Monteith, as ratio between $ET_{0,PM}$ and $ET_{0,HS}$ [mm/year] in each pixel. The final grid of k_{HS} was obtained as multiplying

the original value (0.0023) by the 1970-2019 mean deviations. The calibration was performed considering all the fifty years, in order to include the decades of maximum density of ground sensors used by CRU (1961-1990) [77], and the recent years with most active satellite sensors on which ERA5 is based [74]. This simplified method for the assessment of ET_0 limits the uncertainty related to using many input variables, while remaining consistent with ground-based annual data of Penman-Monteith ET_0.

In **Figure 14** is represented the spatial distribution of the calibrated k_{HS} coefficients on agricultural areas. In most of the coastal zones, the HS method seems to underestimate the rate of daily evapotranspiration, since the calibrated k_{HS} are significantly higher than the mean value of 0.0023. This is probably a consequence of the fact that Penman-Monteith takes into account the effect of wind speed, which is often high in the coastal zones, resulting in higher ET_0 compared to Hargreaves-Samani. The HS methods appears also less effective at higher elevations above the sea (e.g., on the Himalayas), but in these areas the density of agricultural areas is usually very low.
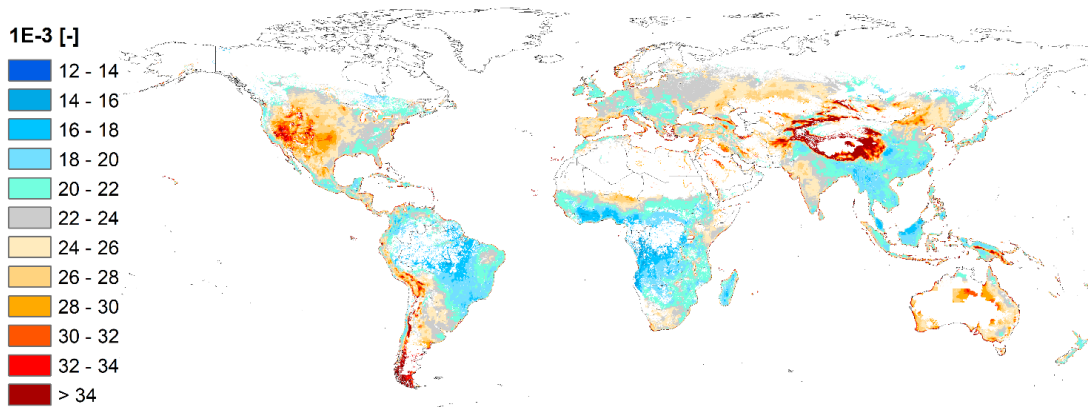
Figure 14. Spatial distribution of calibrated Hargreaves-Samani coefficients (k_{HS}). The calibration was performed on all the pixels containing croplands, according to the MIRCA2000 dataset.

In **Figure 15a**, the mean annual rates of ET_0 [mm/day], calculated with ERA5 data and calibrated according to the method previously described, is shown as average rates for the 2010-2019 decade. In **Figure 15b**, the percentage variations of mean ET_0 is shown, with respect to the 1970-1979 average annual rates.
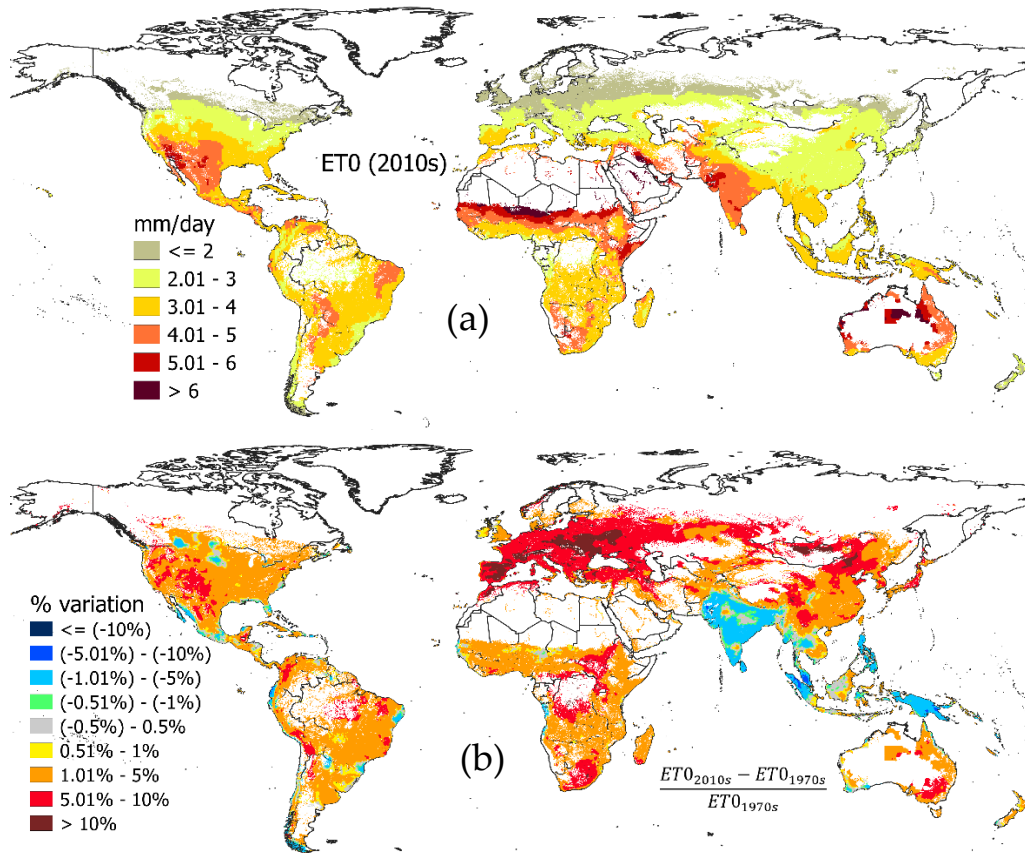
Figure 15. (**a**) Global map of mean rates of Reference Evapotranspiration [mm/day] over croplands, calculated as average values for the 2010-2019 decade. (**b**) Percentage variations of the mean daily ET_0 rates, comparing the 2010-2019 and 1970-1979 decades; blue-green areas: $ET_{0, 2010s} < ET_{0, 1970s}$; yellow-red areas: $ET_{0, 2010s} > ET_{0, 1970s}$; grey areas: very low variations between the two decades (<0.5%).

3.1.2 Initial soil moisture at sowing date

As previously introduced in Chapter 2, the amount of water a crop can draw for its needs is related to the soil properties of water-holding capacity [7]. The available water capacity (*AWC*) of a soil is calculated as difference between the two limits of soil moisture: the upper limit of field capacity (θ_{fc}) [m^3_{water}/m^3_{soil}] and the lower limit represented by the wilting point (θ_w) [m^3_{water}/m^3_{soil}], i.e. the dry condition at which the crop stops evapotranspiration.

In this Chapter, the global SoilGrids dataset (250 m x 250 m resolution) [78] was used to set the global *AWC* over croplands, as an improvement to the dataset previously introduced in Chapter 2 for the assessment on year 2000: this high-resolution dataset allowed to obtain an estimation of the specific *AWC* for croplands, as detailed below.

The original grid was upscaled to obtain a 0.0833° grid, matching the MIRCA2000 resolution. Pixel values were computed averaging the SoilGrids pixels containing croplands according to the global soil classification from the Copernicus Land Service [27]. Since SoilGrids provides data for different soil depths, the final *AWC* was further calculated as a mean between the upscaled grids up to 1 m depth, to set a representative value of available water capacity per unit of soil volume in the rooting zone.

Each crop has a specific tolerance threshold to water stress: the soil moisture threshold of incipient water stress (θ^*) [m³water/ m³soil] depends on the crop-specific sensitivity to soil water deficit, i.e. the difference between the field capacity upper limit and the actual water content in the soil, as described by Allen et al. [7]. The crops that are more sensitive to soil water deficit reach water stress in wetter soils, while the same deficit still represents a sufficiently wet condition for the less sensitive crops.

For temporary crops, the initial soil moisture at the sowing date (θ_{sow}) needs to be defined. Considering the lack of information about the cropland use before the sowing date, the corresponding moisture cannot be obtained from the soil water balance. Previous studies used different solutions to address this problem: Chiarelli et al. [36] used an initial soil moisture equal to 50% of *AWC*; Siebert et al. [33] proposed a simplified water balance on fallow lands with k_c=0.5; Rolle et al. [28] assumed that each growing season starts with soil moisture at field capacity.

In this Chapter, a sensitivity analysis was performed to quantify the impact of initial soil moisture on the final estimations of ET_a and I for temporary crops, in order to set the soil moisture at the sowing date consistently with actual climate conditions (improving the assumption of sowing at field capacity adopted in Chapter 2). Two simulations were performed assuming the two limit values of initial soil moisture, $\theta_{sow}=\theta_{fc}$ and $\theta_{sow}=\theta_w$ in the starting day of each temporary growing season. The global area-weighted average of ET_a and I rates [mm/year] were calculated for the 1996-2005 period, on rainfed and irrigated areas respectively, in order to perform the analysis on a decade centered on year 2000 (for which the agricultural data are available).

Results show that the global actual evapotranspiration of temporary crops is 12% lower when the growing seasons start at wilting point, compared to the "field capacity" hypothesis. Moreover, irrigation requirement (excluding rice) is about 3% higher when all temporary seasons start at wilting point.

Soil moisture data from ERA5 [72] [73] were used in this work for different soil layers, to be consistent with the actual weather conditions over the 50-years period: according to this improvement, the uncertainty related to setting soil moisture at field capacity on the sowing date, as described in Chapter 2 for year 2000, was reduced.

Assuming 0.2 m as the standard effective rooting depth for the water balance calculation at the sowing date [79], the monthly soil moisture grids were calculated as the average between the first two layers (0-7 cm and 7-28 cm respectively). For each sowing day, the soil moisture was calculated as the fraction of the "soil saturation upper limit" dataset from SoilGrids, equal to the ratio between the monthly soil moisture and the saturated moisture from ERA5. Since ERA5 does not provide any information about maximum soil water capacity, the saturated limit was set using the maximum values for the 1970-2019 period in each pixel. When the initial soil moisture turned out to be higher than field capacity, the θ_{fc} value was used.

3.1.3 A statistical index for daily analysis of rainfed water stress

The use of daily hydro-climatic data over a 50-years period enabled long-term simulations at the daily time scale, which in turn allowed to perform analysis of daily results. For each crop, the number of precipitation events (*PD*, i.e. *precipitation days*) with rainfall greater than 2 mm/day was computed for the growing season of every year from ERA5 data. *PD* was compared to the number of days in which the crop requires irrigation (*ID*, i.e. *irrigation days*), considering a minimum modelled requirement of 2 mm/day. For perennial crops, *PD* and *ID* were computed throughout the whole year, while for temporary crops they referred to the growing periods.

The *PD* and *ID* values were also aggregated at different spatial scales: to this aim, the aggregated results were averaged over the area of interest, using the extension of area equipped for irrigation as weight.

In rainfed areas, where no irrigation occurs to avoid the daily water stress, the number of water stressed days (days in which k_s<1) for each crop was computed and indicated with *SD*. In order to compare pixels with different cropland extensions and compositions, a proper index was defined considering all crops grown in the pixel, i.e.

$$wSD_{y,j} = \frac{\sum_{c=1}^{26} SD_{y,c,j}}{\sum_{c=1}^{26} LGP_{c,j}} \, . \tag{7}$$

wSD [-] quantifies the annual number of water stress days of year *y* on the *j*-pixel, calculated as the ratio between the sum of *SD* on rainfed areas for the 26 crops, and the sum of the corresponding lengths of growing periods (*LGP* in days) in the same pixel. The *wSD* index has been introduced to normalize the total number of water stress days per pixel. The rainfed scenario ensures that no other

water inputs occur but rain, allowing to test the effect of dry periods on cultivations.

3.2 The global variability of irrigation requirements over the period 1970-2019

The irrigation requirement (*I*) is strongly related to the precipitation availability. In this Chapter, the temporal changes of global irrigation requirements are discussed, both in terms of global annual rates, number of days requiring irrigation and crop-specific variability.

3.2.1 Temporal variability of annual days requiring irrigation

More than on the total rainfall rate, *I* depends on how rainfall is distributed across the growing season: more irrigation is required during long dry periods, while frequent small rainfall events may keep soil moisture far from stress levels. The number of days requiring irrigation per growing season (*ID*) depends on the crop type, on the geographical position and on the harvesting calendars. This variable and the seasonal number of precipitation days (*PD*) referred to the maize growing seasons, were computed and aggregated in different areas of the world (**Figure 16**). A t-Student test was performed to highlight significant temporal trends for *ID*, with a level of significance of 5%. Positive trends of *ID* were found to be statistically significant in Europe, East-Asia, South-East Asia, West Asia, South America, Sub-Saharan and North Africa. In the Southern and Eastern zones of Europe, trends of *ID* are marked because of the combination of ET_0 increments and strong decreases of *PD* (in some cases, -35% from 1970s to 2010s), as confirmed by Seneviratne et al. [80]. In Northern Africa, precipitation is very low (both considering annual rates and number of events): therefore, the *ID* increment through the years is mainly driven by the ET_0 trend. Significant *ID* trends were found in Sub-Saharan Africa, West and East Asia and Oceania, with different slopes.

The slightly negative *ID* slope in North America results from the combination of two opposite scenarios: in the East part of Canada and U.S. a precipitation increment caused a considerable reduction of irrigation requirement, while on the Western regions the opposite occurs (not strong enough to be detected on a sub-continental scale).
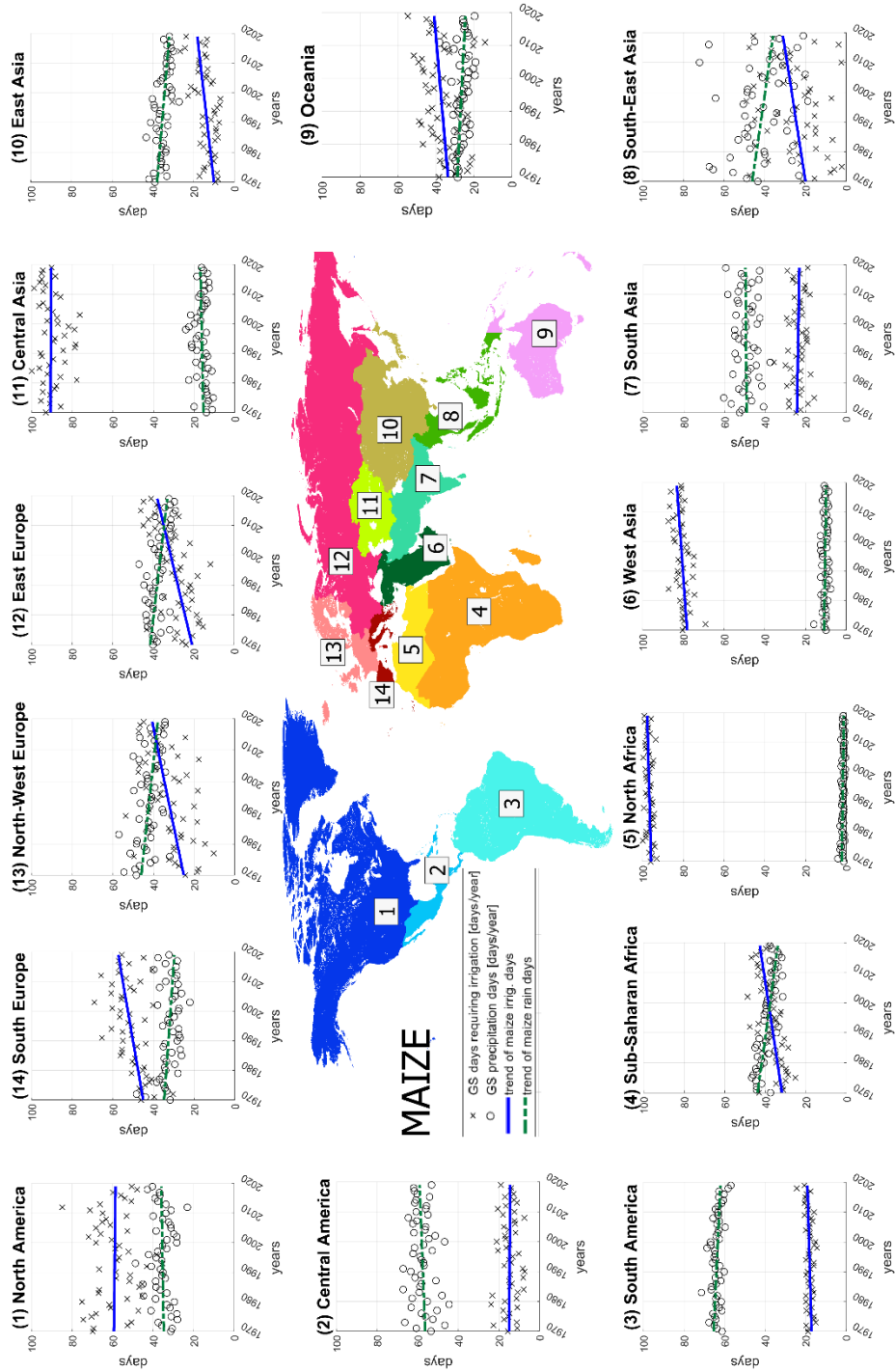
Figure 16. Temporal variability of annual precipitation days (circles) and days requiring irrigation (crosses) for the growing of maize (1970-2019). The slopes of the green and blue lines show the linear trends of rainfall days and irrigation days for maize, respectively. The analysis is performed in fifteen areas of the world, defined by the UN classification. In the legend, GS stands for Growing Season.

Changes of *PD* from ERA5 are reflected in other studies about trends of wet days, like the global analysis by Rajah et al. [81]. Global projections from the last IPCC report [82] shows high confidence that future changes of wet days will confirm the trends of the last decades.

An increase in time of the number of days requiring irrigation (*ID*) leads to two main consequences. First, higher *ID* often implies increment of irrigation requirement volumes over the growing season, because the final estimation results from a larger number of stress events. Second, the crop requirement in many areas of the world may not be entirely satisfied with the current irrigation calendars, especially for those crops requiring frequent irrigation (e.g., vegetables or pulses).

3.2.2 Spatio-temporal variability of annual irrigation requirements

The temporal variation of irrigation requirement rates (*I*) was analyzed for the 26 crops under study, calculating daily series from 1970 to 2019. The analysis reveals that *I* increased in 62% of areas equipped for irrigation, comparing the mean annual rates of 1970s and 2010s decades (**Figure 17**).
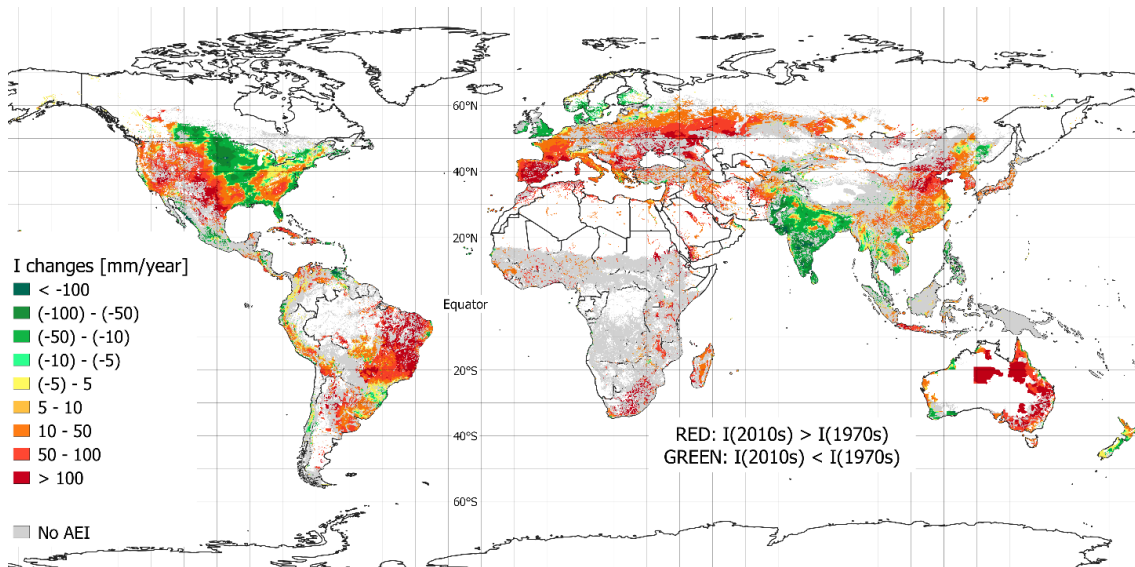
Figure 17. Changes of mean annual irrigation requirements (I) [mm/year], comparing 1970s and 2010s. The map colors describe how much (red) or less (green) irrigation is required over the AEI between the two decades, comparing the 10-years AEI-weighted average requirement of 26 crops.

The increment is higher than 10 mm/year on more than 53% of global irrigated areas. The highest increments of mean annual I (>100 mm/year from 1970s to 2010s) were found in South Europe (especially in Spain, Italy, South France, Balkan peninsula and Ukraine), North-East China, the eastern part of Australia, Brazil, and the western part of U.S.

In 29% of irrigated areas, the irrigation requirement decreased from 1970s to 2010s for more than -10 mm/year. Most of these areas are concentrated in South Asia and in the central part of U.S., from North Dakota to Mississippi. In the first case, less irrigation is required because of the combined effect of mean ET_0 decrease and precipitation increments (especially in the Indo Valley and Northern India), while the result in U.S. depends mostly on the greater precipitation availability (+100 mm/year from 1970s to 2010s), that compensated the increment of ET_0 (+10 mm/year).

3.2.3 Crop-specific variability of irrigation requirements

The comparison of crop-specific rate of irrigation requirement between 1970s and 2010s shows a heterogeneous pattern. The variability of climate forcings has different impacts on I depending on the latitude, because of the heterogeneous changes of P and ET_0. The crop-specific comparison shows that in most of the northern AEI, above 30°N, more irrigation is required in 2010s than in 1970s. As shown in **Figure 18**, going from North to South, all the croplands require more irrigation except the fodder grasses (which are mainly cultivated in the Eastern part of Canada and U.S., where the I rate have decreased).

The crop-specific analysis in the northern hemisphere shows higher increments of I from 1970s to 2010s for multi-seasonal temporary crops (e.g., wheat, which is cultivated both in winter and spring-summer), especially in North-West America, Europe and North-Central Asia. Soybean requires quite the same amount of irrigation if comparing the two decades at these latitudes, as a result of the opposite effects of higher I in Eastern China and lower I in Eastern U.S. Most of the irrigated areas from 30°N to Equator are in South-East Asia, except for some regions in Central America.
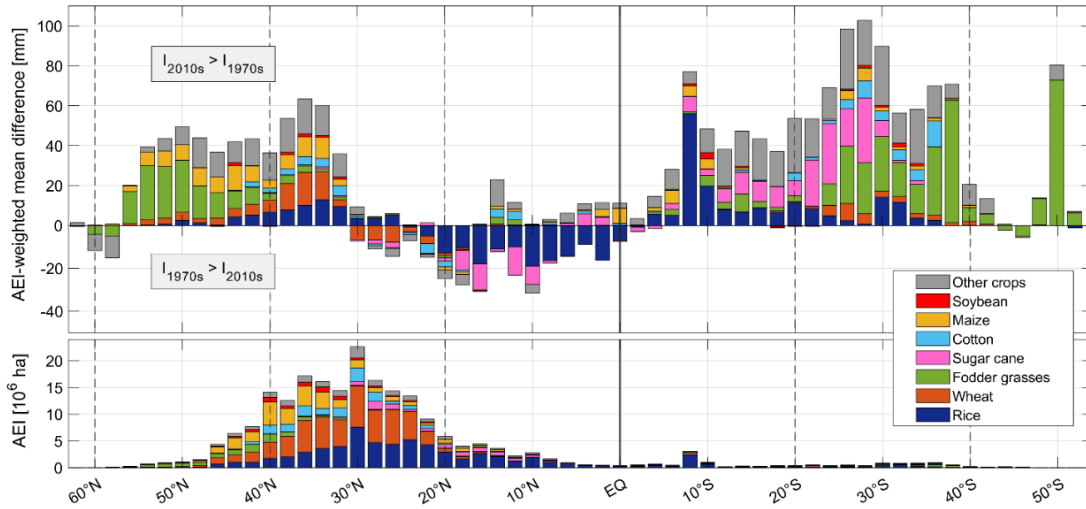
Figure 18. Variations of crop-specific irrigation requirements [mm] by latitude, between 2010s and 1970s. The box below shows the geographic distribution of crop areas equipped for irrigation (AEI): more than 90% of AEI are in the Northern hemisphere, most of which located between 20°N and 40°N.

Most of the AEI in India and Pakistan requires less irrigation in 2010s than in 1970s: the irrigated croplands in these nations are favored by the changes of climate forcings, which lead to an advantageous scenario from the point of view of agricultural water needs. Considering the global scale, a hypothetical crop switch from North to South in Asia could be a beneficial solution, with a significant reduction of *I*. For example, larger increments of irrigation requirements were found in the Northern part of China, where most of the irrigated areas are concentrated and water is partly transferred from southern regions, through the South–North Water Transfer Project [83].

Less than 10% of irrigated lands are in the Southern hemisphere. The analysis of water requirement variability indicates very high increments of irrigation requirement for all the crops cultivated in these regions. The combined effects of climate forcings on Oceania, Southern Africa and Southern America, lead to significant disadvantages in the irrigation practices in this hemisphere. The Amazon region appears to be quite unsuitable for irrigated agriculture from a climatic point of view [84] and results show high increments in the irrigation required by crops in this area. Contrary to the Northern hemisphere, irrigation requirement has increased more on the coolest regions going from North to South, mainly because of the strong reduction of mean annual precipitation (up to -300 mm/year in Brazil, due to the combined effect of climate variability and deforestation [85]). The irrigation requirement of soybean appears to be less sensitive to climatic variability, as previously found in the Northern hemisphere.

A more detailed analysis of the *I* variations was performed considering some relevant crops. In **Figure 19**, the temporal variability of mean daily irrigation requirements of citrus is shown, comparing the Aragon-Catalonia region (Spain), Israel and Cuba.
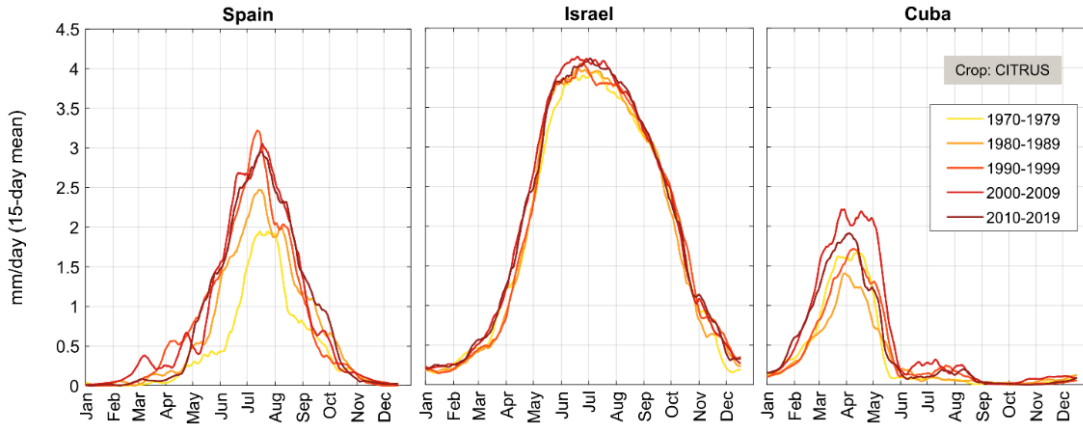
Figure 19. Daily irrigation requirement of citrus (perennial crop) over decades. The three plots show the variability of daily citrus irrigation requirements over Spain (Aragon-Catalonia region), Israel and Cuba. Every line represents the mean irrigation requirement over a decade, plotted as a 15-days moving average [mm/day]. The increment of irrigation required by citrus is evident, especially during summer months in Spain and spring months in Cuba.

The mean daily *I* has generally increased comparing 1970s and 2010s (e.g., +50% in Spain during summer, from about 2 mm/day to more than 3 mm/day). The period of irrigation has also increased through the years in the three countries. In the last decades, citrus required irrigation in the early-spring period (which wasn't necessary in the 1970s) and higher irrigation rates during the spring and autumn periods.

3.3 Water stress trends on rainfed croplands

A trend analysis of crop water stress, induced by climate change, was performed on rainfed croplands. On these areas, precipitation is the only water input, and it is possible to quantify and compare the length and the severity of water-stress periods. Considering this, it is possible to relate the water stress to potential yield losses of rainfed crops.

The annual water stress days (*wSD*) were calculated for each pixel containing rainfed crops, from 1970 to 2010, as described in Chapter 2.4. A *t*-Student test was performed to highlight significant trends, with a level of significance of 5%. On a global scale, 38.1% of rainfed areas show statistically significant positive trends of

annual water stress days, while significant decreases were found only for 6.7% of the rainfed areas.

As shown in **Figure 20a**, large part of East Europe and East China shows high trends of wSD, more than double in 2010s than in 1970s. In the Central Africa, high wSD increment depends on the fact that in 1970 rainfed areas were affected by very small stress: despite the water stress in 2010s still counts a few days per year, it should be noted that most of the croplands in Central Africa are rainfed, and these increments may lead to reduction of crop yield with significant consequences. South and East Europe are affected by significant increments of annual stress days. Some of these regions are densely cultivated (e.g., Northern Italy, Spain and Ukraine), and high positive stress trends may limit the rainfed crop yield, affecting national crop productions. Western China shows a similar scenario, while in the central part of the nation the heterogeneous changes of precipitation availability led to a more complex scenario: increments of precipitation in Eastern Qinghai have diminished the water stress on rainfed areas.

All the South America shows high positive trends of wSD, especially in the Amazon region. Despite the mean annual precipitation rate has slightly increased over the decades, the annual number of precipitation days has decreased (as shown in **Figure 16** for the maize season). Because of this situation, the low number of stressed days has more than doubled in many parts of Brazil and Colombia. India is one of the nations with the highest extension of rainfed areas. A large part of this region is affected by significant negative trends of annual ET_0, resulting from the combined effect of factors: the falling of the difference between maximum and minimum temperatures, decrease of wind speed and increasing of cloudiness on the region [86]. The further general increase of annual precipitation rates, according to the ERA5 data, leads to significant decrease in the number of stressed days per year, particularly in the Southern part of the nation.

A similar analysis was performed to find significant trends of severe water stress, considering annual days close to wilting point ($k_s < 0.1$). In this case, 16% of rainfed croplands show a significant positive trend (as shown in **Figure 20b**). In North America, most of the rainfed areas are affected by low trends of annual stress days, both positive (in the Western region) and negative (Minnesota, North Dakota and Missouri). However, the number of severe-stress days has increased in most of the Western rainfed croplands.

This means that, even if the annual duration of water stress didn't significantly change (**Figure 20a**), water stress has become much more severe. High trends of severe stress were found in Spain, Ukraine, North-East China, South Africa and the Amazon region. The analysis of water stress on rainfed croplands is particularly interesting for those countries with poor irrigation infrastructures. In these nations, water stress increments may have a huge impact on the local economy, with limited possibility of adaptation because of the technology gap.
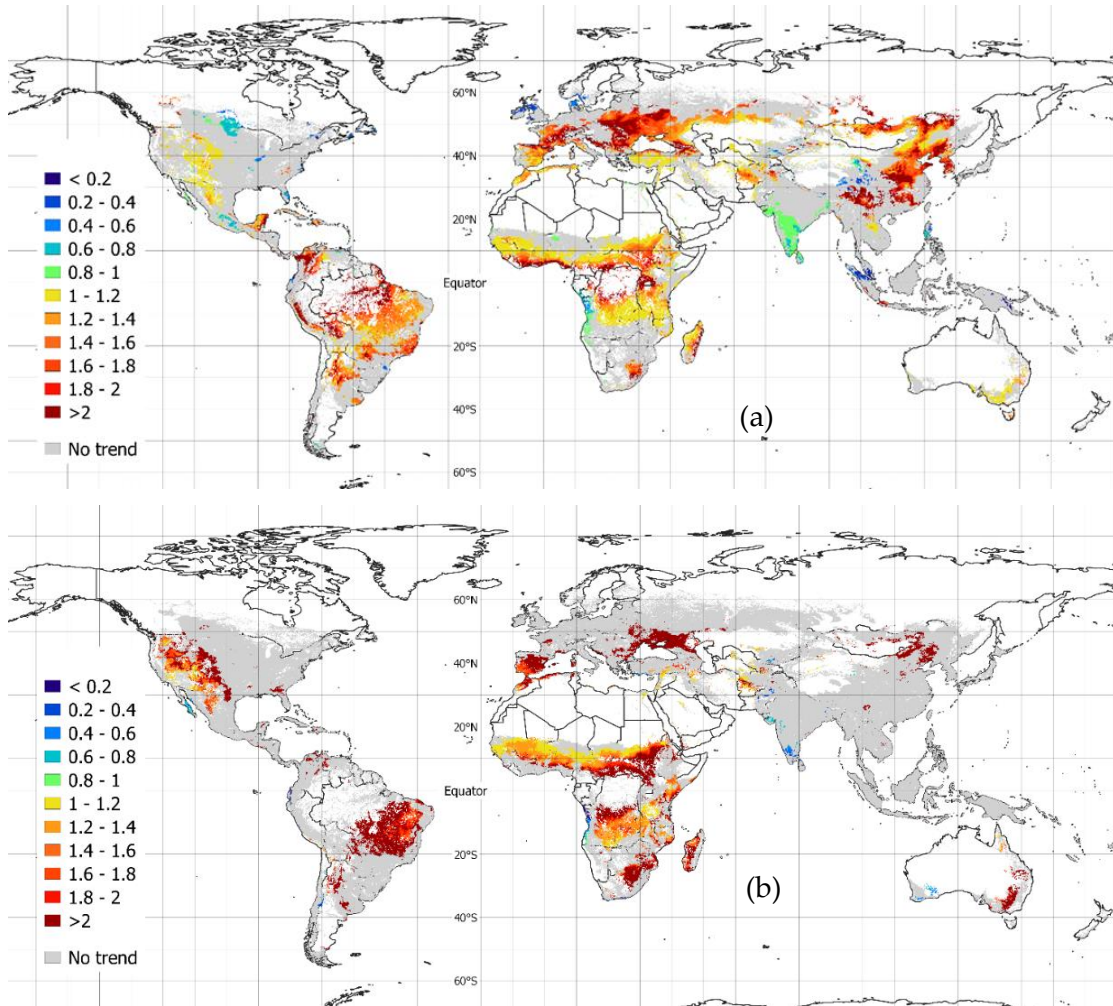
Figure 20. (**a**) Ratio between 2010s and 1970s mean annual stress days on rainfed areas. Warm colors indicate that the mean number of annual stressed days has increased during the last 50 years, while the cold colors describe the opposite scenario. Over grey areas, there is no significant trend of water stress days, according to the t-Student (level of significance of 5%). (**b**) Ratio between 2010s and 1970s mean annual severe stress days (k_s<0.1) on rainfed areas. Warm colors indicate that the mean number of annual severe stressed days has increased during the last 50 years, while the cold colors describe the opposite scenario. Over grey areas, there is no significant trend of severe water stress days, according to the t-Student (level of significance of 5%).

In contrast, important rainfed stress and consequent yield losses may induce developed countries to improve the irrigation efficiencies of their irrigation systems [87], equipping part of the rainfed fields for irrigation. As an alternative, nations may shift to alternative crops and varieties and/or shift planting dates in areas most affected by climate impacts, using crop migration as an adaptation strategy [88].

3.4 Comparison with previous analyses

Despite several previous works have dealt with the impact of climate variability on the agriculture water requirements, a few studies focused on large spatial scales. Despite any previous long-term assessment of multi-crop daily water requirements is actually available at the global scale (to the best of the author's knowledge), some previous studies were used to compare the results in terms of crop-specific trends or sub-continental assessments.

The global assessment by Chiarelli et al. highlights that the actual evapotranspiration from irrigated croplands increased by 4.07% from year 2000 to year 2016 (N.B. the analysis was based on the agricultural data from MIRCA2000 and on the FAO guidelines, as for this thesis); yet, the global volume of irrigation requirements (named *Blue Water* by Chiarelli et al.) decreased by 5.9% between 2000 and 2016: this result can be explained considering the decrease of needs for irrigation in South Asia (i.e. the region with the highest density of irrigated croplands), as also pointed out in this dissertation.

Therefore, a comparison with previous results can be done by comparing estimations over specific nations or regions. For example, the analysis of temporal water demand for some major crops in the Hebei province (China), which was carried out by Li et al. [89], confirmed some of the results from the present thesis; in fact, the region in the north-east of China is one of the most exposed to temporal increments of irrigation demand, and this climate-induced condition has been highlighted both by the present analysis over the 1970-2019 period and by the 2007-2017 analysis performed by Li et al.

The global assessment conducted by Oumarou Abdoulaye et al. [90] quantifies the variation of maize irrigation requirement between 1960 and 1999, at the global scale. Results from this study pointed out temporal increments of maize needs for irrigation all over the world, comparing 1999 to 1960: +1.63% in Latin America and Caribbean, +1.36% in South Asia, +2.05% in Sub-Saharan Africa, +4.78% in Europe and Central Asia, +3.11% in Middle East and North Africa, +2.64 in East Asia and +2.66% in North America. The comparison with results in **Figure 16** highlights a good alignment for the case of maize, even if the result from this thesis quantifies the trends of irrigation days per year (N.B. even if the irrigation days and the rate of irrigation requirement are two different variables, their increments are strongly correlated). In particular, the comparison between two years, 1960 and 1999, may not be enough representative of an actual temporal change, since the results are driven by the weather conditions of a specific year and not averaged on a decade. However, the crop-specific analysis by Oumarou Abdoulaye et al. fit well the results from this thesis, comparing the changes in different sub-continental regions.

Results were compared to the assessment by the European Environmental Agency (EEA), describing the changes of the crop water demand and crop water deficit (i.e. the difference between annual rates of ET_c and ET_a, assuming no irrigation) of grain maize during in the European Union (E.U.) [91]. The EEA highlights that most of the European irrigation requirement comes from the Mediterranean countries (in terms of annual rates [mm/year]), especially in Spain. Moreover, the study of how water deficit changed for grain maize between 1995 and 2015 pointed out increasing gaps between water requirements and available precipitation in most of the Mediterranean regions: in these two decades, the maize water deficit increased more than 5 mm/year in many regions of Italy, Northern Spain, Southern France and Greece. The water deficit also increased significantly in most of the Eastern nations of the E.U. (especially Poland and Romania). In UK, the maize water deficit decreased between 1995 and 2015 (between -3 mm/year and -1 mm/year, on average). These results are consistent with the map of water stress trends in **Figure 20**, where however are described the trends of stress days per year (instead of water deficit rates) considering all the crops and not just maize. The most evident difference in the comparison was founded in France, where the number of agricultural stress days per year appears to be significantly increased from 1970 to 2019, while the EEA calculated a decrease of maize water deficit between 1995 and 2015. This difference can be explained considering that the reference periods of the two analyses is very different, both as number of decades and starting year; moreover, the increment of stress days in France can be explained considering the increasing of winter drought conditions, which do not affect summer crops like maize.

3.5 Concluding remarks

In this Chapter, the impact of climate change on rainfed and irrigated agriculture has been examined through trend analyses of water requirements and water stress. Results show heterogeneous changes in the irrigation requirements of crops over the 1970–2019 period, both in terms of annual rates and in the number of days in which irrigation is required. On more than 53% of irrigated croplands, the irrigation requirement has increased more than 10 mm/year comparing the 1970s and 2010s decades. Moreover, there is a statistically significant increase in the annual number of days requiring irrigation in most irrigated areas of Europe, East and West Asia, Africa and Oceania, mainly due to a decrease of precipitation events during the growing seasons.

The global analysis of temporal changes also highlights a decrease of annual irrigation requirements in some world areas, such as the intensively cultivated areas in South Asia and North-East America, comparing the mean annual rates of

2010s and 1970s. Focusing on rainfed croplands, the temporal analysis highlights that 38.1% of areas are affected by statistically significant positive trends of annual water-stressed days, while significant negative trends were found on 6.7% of rainfed areas. On 6% of rainfed areas, the number of annual water-stressed days has more than doubled over the considered period (1970–2019) and 16% of rainfed areas show a statistically significant increment of severe water stressed days per year.

Most of the cereals which are cultivated in North America and Europe required more irrigation in 2010s than in 1970s, especially rice and wheat. The increase of irrigation requirements is progressively higher moving from North to South for most of the crops, particularly for cereals. In India and Pakistan, however, the irrigation requirements generally decreased through the decades, especially for rice, wheat and sugar cane. Most of the irrigation requirements in the Southern hemisphere has highly increased, disadvantaging the irrigated agriculture respect to the Northern regions. In most of Europe, South-East Asia, Oceania and Sub-Saharan Africa, the number of days per growing season requiring irrigation has significantly increased, especially because of decreases in seasonal frequency of rainfall days.

The global analysis of changes in the agricultural water requirements confirms that hydroclimatic forcings have already affected crop evapotranspiration in the past decades, causing yield losses. As regards the fixed in time distribution of croplands, a more detailed analysis of water volumes will be enabled when new crop-specific data quantifying the temporal evolution of rainfed and irrigated areas will be available. However, the results here obtained are already relevant to understand the climate-driven trends in water requirement. Results presented here are useful in the choice of adaptation strategies to climate change in agriculture at large spatial scales and may support the decisional process leading to policies of water and agriculture management and food production. These actions are, in fact, particularly complex in an increasingly globalized world, where nations are dependent on each other for food production and tightly interconnected by international trade.

Chapter 4

Satellite-based estimation of sowing dates and growing phases

The work described in this Chapter has been partially derived from paper [92]

The reliability of crop-growth modelling is related to the accuracy of the information used to describe the agricultural growing phases. A proper knowledge of sowing dates has a significant impact on the effectiveness of any analysis based on modeled crop seasonal developing. Since one of the highest uncertainties in the modelling of crop water requirements is due to the lack of actual large-scale sowing calendars, it is essential to exploit the potential of remote sensing to limit this uncertainty.

In this Chapter, a remote sensing-based estimation of maize sowing periods for year 2019 is presented. The analysis is based on the optical and radar information from Sentinel-1 and Sentinel-2, used in combination to identify the actual emerging periods of maize in a temperate area equipped for irrigation, in the northern part of Italy. The choice of testing this method on a local scale is due to the need of validate results with local sowing information. Moreover, the aim of this method is providing a solution for large-scale analyses, since the satellite data could easily be used in different parts of the world.

The crop classification was carried out according to the information provided by local public authorities over an area of 30 x 30 km, and 1154 maize fields were considered within the analysis. The satellite data were used to check the potential presence of rainfed maize, depending on the position of the fields in relation to the irrigation channels and the administrative areas belonging to the irrigation districts.

The combined use of NDVI and radar time series allowed a high-resolution assessment of sowing periods and the description of maize growing phases, by detecting changes in the ground surface geometry. A radar-based index was introduced to detect the periods when plants emerge through the soil, and the sowing periods were retrieved considering the heath needed by seeds to germinate and the daily temperatures before the emergence.

Results show that the pilot area can be considered uniformly equipped for irrigation. The comparison between NDVI and SAR time series shows the higher sensitivity of radar for the monitoring of maize during the final growing phase. Sentinel-1 appears more suitable to describe the late growing phase of maize, since the radar backscattering is sensitive to the dry biomass of plants while the NDVI decreases because of the chromatic change of leaves.

More than 60% of maize is sowed in April, 52% during the last 6 days of the month, also highlighting the presence of another important sowing period in May. Orography can partially explain the delay of sowing, since the optimal climate conditions for agriculture occur later at higher elevations. Even if a moderate correlation (R=0.41) was found between sowing periods and elevation above the sea level, also the presence of winter crops in the most densely cultivated areas can contribute to delay the sowing of spring maize at lower elevations. The results obtained highlight the potential of synergy between remote sensing sources for agricultural management policies and to improve the accuracy of crop-related modelling.

4.1 Potential of EO for high-resolution crop monitoring

The analysis of crop growing phases is essential to gather information about the factors affecting agricultural production and to adopt proper management strategies. Given the importance of agriculture in the global food system, the sensitivity of crop yields to several factors is increasingly studied through multidisciplinary approaches. Many studies are based on crop models, requiring input information at proper resolutions and spatial scales [93]. The improvement of crop modelling at different spatial scales, from local to global, is a key factor in raising awareness of drivers affecting crop yield and crop-related variables. The importance of climate variables for agricultural production is widely analyzed, particularly in terms of climate-driven impacts through the past decades [68] and of future vulnerability due to projected climate scenarios [69]. Besides to climate variables, agricultural production is very sensitive to human practices, technological improvements, and local policies [10].

Sowing periods have an important impact on the crop yield of many of the most common crops, like maize, wheat and rice [94]. Several authors analyzed the impact of late sowing on yield losses; for example, studies have shown that late sowing causes maize yield losses in the U.S. Midwest, because of increasing water stress during the vegetation and reproductive phases [95]. Similar analyses have been performed for different crops: for example, Ortiz-Monasterio et al. [96] quantified that wheat yield decreases by about 1% for every day of late sowing in Northern India, because of non-optimal climate conditions in the final growing

phase. Frequently, the temporal shift of sowing and harvesting dates has been adopted as local adaptation strategy to climate change, e.g., the sorghum production in Italy [97], rice in Sri Lanka [98], soybean in Austria [99], oilseed crops in the U.S. South-West [100]; however, many limitations still constrain the adjustment of growing periods as a reliable strategy to prevent local climate-driven yield losses [101].

Earth Observation (EO) has shown a high potential to retrieve land surface parameters [102] [103]. Remote sensing is increasingly used for agricultural applications because it provides data suitable for many purposes, from large-scale numerical modelling to precision farming. Techniques combining optical and radar data from satellites offer a wide range of solutions for high-resolution agricultural applications [104]. The optical data are highly sensitive to the color of the soil, to the dynamics of the vegetation cover as well as to the process of photosynthesis, while microwave instruments can detect geometric and dielectric properties of ground surfaces [105] [106]. In fact, the measured signal is dependent on the radar configurations (frequency, incidence angle, and polarization) and the dielectric and geometric properties of the surface.

The study of EO as an instrument to retrieve sowing information is receiving an increasing attention. Although some sowing calendars are provided for global crop models (e.g., the MIRCA2000 gridded monthly calendars [41] or the FAO national information for irrigated crops [107]) there is still a lack of information at regional and local scale, where the spatial variability of sowing days and multi-seasonal practices is more evident. Several studies addressed the use of satellite data for the assessment of crop sowing periods in different regions of the world, combining sensors and frequency bands to describe initial phenological phases. For example, Zhang et al. [108] developed a scalable method based on MODIS data to estimate sowing periods of soybean in Mato Grosso (Brazil). EO-based methods were tested for several crops in many other regions, such as maize in South Africa [109], maize and soybean in the U.S. states of Iowa, Illinois, and Indiana [94], and wheat in India [110]. Several combinations of EO sensors have been exploited, mostly based on visible, infrared and microwave data. Recently, much attention has been given to active radar as a reliable instrument to retrieve sowing periods [111]. The analysis performed over the Bekaa Valley (Lebanon) by Nasrallah et al. [105] showed the reliability of multi-polarization active radar for the assessment of crop sowing periods.

This Chapter aims also to exploit the potential of combined optical and active radar information to describe the vegetation cycle of maize, highlighting the strengths of each sensor to detect significant properties of growing phases. To address the above goals, the high-resolution information from Sentinel-1 and Sentinel-2 have been combined with ground information on land use to analyze the growth cycle of maize over a densely cultivated temperate region in Piedmont

(North-West Italy). Since maize is sowed and harvested within the same year, the analysis was carried out for the year 2019: besides the availability of data, analyzing year 2019 avoids uncertainties related to the agricultural practices during the global pandemic occurring in 2020.

In Chapter 4.2, the satellite data used for the study and the ground information which was used to derive the land classification are presented. In the same Chapter the procedure adopted to identify the pilot fields, to describe the phenological cycle of maize and to derive sowing dates is detailed. In Chapter 4.3, the results of the applications are presented and discussed; first, the checking for rainfed areas in the largely irrigated region are addressed; the spatio-temporal variability of emerging and sowing periods is then discussed, comparing the results with available large-scale calendars and with the information provided by local farmers.

4.2 A satellite-based method for the monitoring of maize sowing and growth

4.2.1 Characterization of the pilot area

This study aims to exploiting the potential of remote sensing information to analyze the maize growth over a densely cultivated pilot area within the province of Cuneo, in the North-West of Italy. The pilot area extends approximately from 7.47°E to 7.85°E, and from 44.34°N to 44.6°N (about 30 × 30 km), including the municipalities shown in **Figure 21**. Most of the croplands are distributed in the plain region in north-central part of the site, typically below 600 m of elevation, according to information from the Corine Land Cover classification [112] and the Digital Terrain Model provided by Regione Piemonte [113]. According to the Köppen–Geiger classification, the local climate is warm temperate, with humid summers and mean temperatures below 22 °C.

The monthly hydro-climatic information provided by ISPRA [114] shows that the mean precipitation and the mean reference evapotranspiration range between 2–3.5 mm/day and 2.5–3 mm/day respectively (average values for croplands from April to October), as shown in **Figure 21c** and **Figure 21d**.

The pilot area is characterized by a complex pattern of crops and an extensive network of irrigation channels. Maize is the most cultivated cereal, accounting for 65.7% of cereal areas and 17.0% of total agricultural hectares (including pastures and fallow lands), according to the Italian National Institute of Statistics (ISTAT [115]).
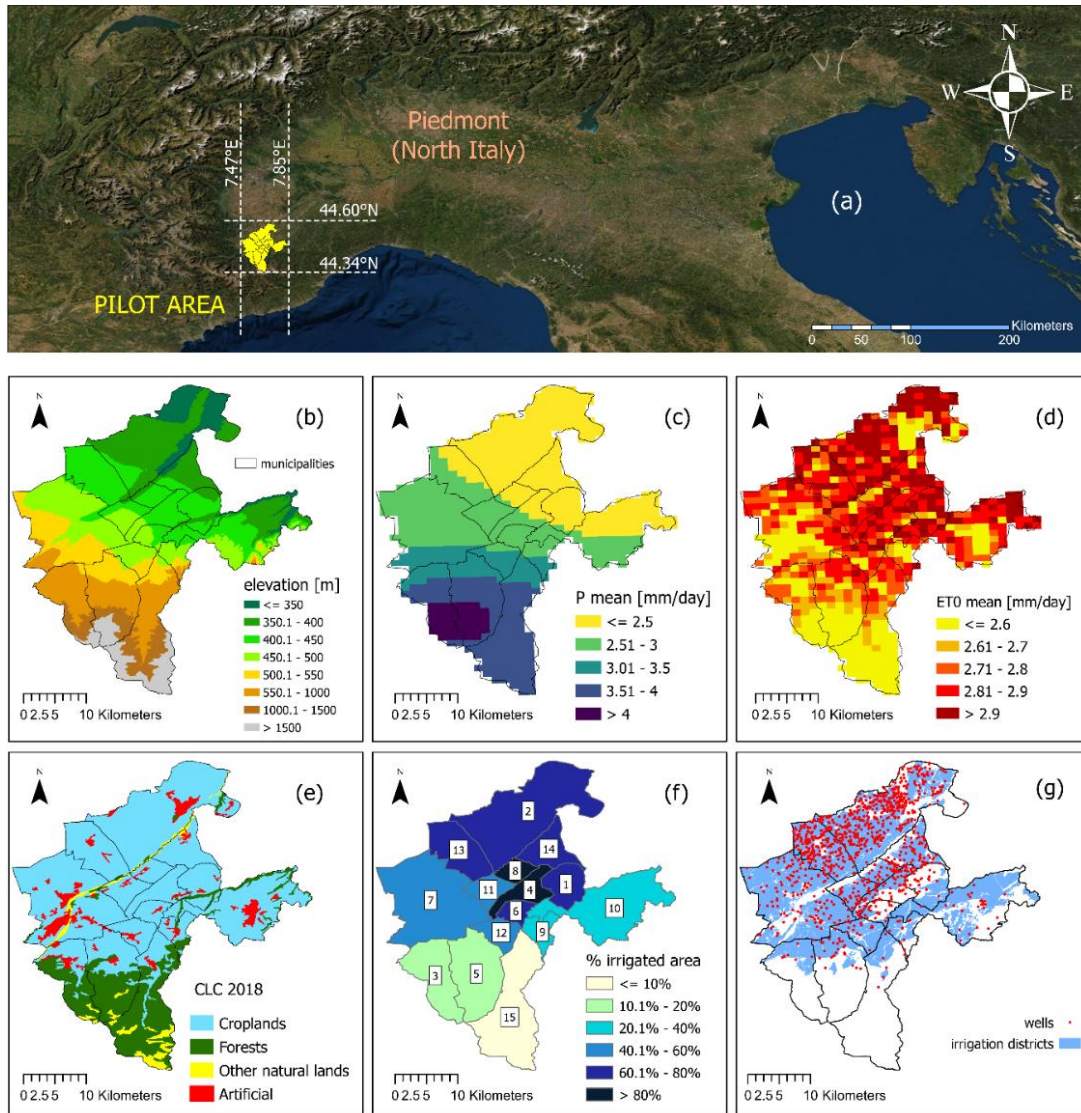
Figure 21. Characterization of the pilot area: location, elevation, climate, croplands, irrigation districts. (**a**) Location and limits of the pilot area (7.47°E to 7.85°E, 44.34°N to 44.6°N): 15 municipalities in the province of Cuneo (North-West Italy). (**b**) Spatial elevation above the sea level [m], 10x10 m resolution. (**c**) Mean daily precipitation [mm/day] from April to October (average 1970-2019). (**d**) Mean daily reference evapotranspiration [mm/day] from April to October (average 1970-2019). (**e**) Land classification of the pilot area, according to the Corine Land Cover (2018) information. (**f**) Fractions of irrigated croplands [%] with respect to the overall municipal areas: Rocca de' Baldi (1), Fossano (2), Boves (3), Morozzo (4), Peveragno (5), Margarita (6), Cuneo (7), Montanera (8), Pianfei (9), Mondovì (10), Castelletto Stura (11), Beinette (12), Centallo (13), Sant'Albano Stura (14), Chiusa di Pesio (15). (**g**) Irrigation districts and infrastructures, including rain gauges.

As shown in **Figure 21f**, irrigated croplands account for large parts of municipal territories, especially in the north-central part of the site, according to the Agricultural Census promoted by ISTAT in 2010 [116] (e.g., irrigated croplands are more than 80% of Morozzo and Montanera overall areas). The same Census highlights that about 90% of maize fields in the province of Cuneo are irrigated. The pilot site is equipped with a dense network of irrigation channels, belonging to 7 irrigation districts. The shape files describing the extension and the location of irrigation infrastructures and administrative areas were provided by Regione Piemonte [117]. More than 98% of irrigation channels are located within the borders of the irrigation districts. Besides the network of irrigation channels, the area is equipped with a high number of wells [118] (**Figure 21g**), which may provide additional water to the fields.

4.2.2 Satellite data

Sentinel-1

The Sentinel-1 constellation acquires C-band SAR (Synthetic Aperture Radar) data, at the spatial resolution of 10 m × 10 m. The synergic acquisitions of Sentinel-1A (launched on 3 April 2014) and Sentinel-1B (launched on 25 April 2016) provide co-polarized (Vertical-Vertical, VV) and cross-polarized (Vertical-Horizontal, VH) images with a 6-days frequency and an incident angle of approximately 39° at the study site.

The Sentinel-1 data are available at different processing levels, depending on the corrections applied to the raw acquisitions. The Level-1 of Sentinel-1 data provides GDR (Ground Range Detected) images, available as gridded backscattering coefficients derived from raw signals through a processing procedure: thermal noise removal, radiometric calibration, terrain correction and speckle filtering [119].

The Sentinel-1 data used in this study were downloaded from the Google Earth Engine platform [120] as multi-band rasters in decibel units, which were pre-processed to meet the Level-1 GDR requirements [121]. The mask of maize fields shown in **Figure 22a** (whose characterization is discussed in Chapter 4.2.1) was used to select just the maize pixels from the SAR images. The VV and VH polarization bands were extracted from the multi-band rasters and converted from decibel (dB) to linear (lin) units:

$$VV_{lin} = 10^{\left(VV_{dB}/10\right)} \tag{8.a}$$

$$VH_{lin} = 10^{\left(VH_{dB}/10\right)} \tag{8.b}$$

where *VV_dB* and *VH_dB* are the backscatter signals provided in decibels as Level-1 SAR product; VVlin and VHlin are the backscatter signals converted into linear units, which are consistent with the units of raw acquisitions.

The SAR instrument from Sentinel-1 is an active microwave sensor, which has been shown to be sensitive to several ground variables, such as soil moisture [106] [122] [123] and surface geometry [124]. Both VH and VV channels can be used for crop growth monitoring, since the phenological cycle impacts the ground geometry of the fields, both in terms of roughness and biomass volume. The co-polarized signal has been shown to be more sensitive to combined surface-volume scattering, also having a high signal-to-noise ratio, while the cross-polarized channel is more suitable for detecting volumetric changes of vegetation [125].

Normalized SAR-derived index

The potential of the combined use of VH and VV for agricultural monitoring has been explored in the scientific literature. The VH/VV ratio (**Figure 22b**) has been shown to be a very suitable vegetation index, being able to limit the double-bounce effect caused by the vegetation ground interaction [104] [105] [106] [125].

The effect of soil moisture and bare soil roughness can be limited by normalizing VH/VV, which is able to detect the vegetation-induced backscattering setting the minimum signal for a specific type of crop, and then filtering the soil moisture-induced noise during the bare-soil period. However, even if Sentinel-1 enables the detection of high-resolution ground geometric changes, the aim of this study is to retrieve information of generalized behaviors of crop-specific sowing, to compare the estimations with local available sowing information and general crop calendars. For this reason, a large number of fields were considered in this case, in order to perform the EO-based analysis within a representative spatial sample of the area.

For each acquisition, the average VH/VV ratio was calculated for every maize field through a GIS-based analysis. The VH/VV mean results were then converted into decibel units with:

$$\left(\frac{VH}{VV}\right)_{dB} = 10 \cdot \log_{10}\left(\frac{VH}{VV}\right)_{lin} \tag{9}$$

In order to compare the signals from different maize fields, a new index called *IPR* (Polarimetric Ratio Index) is proposed in this study; it is based on the normalized VH/VV ratio considering the maximum and minimum value from each field:

$$IPR_i = \frac{\left(\frac{VH}{VV}\right)_i - \left(\frac{VH}{VV}\right)_{min,i}}{\left(\frac{VH}{VV}\right)_{max,i} - \left(\frac{VH}{VV}\right)_{min,i}} \tag{10}$$

where the max, min pedexes identify the maximum and minimum values of VH/VV_i [–] during the growing season respectively, calculated for each i-th maize field. The *IPR* index allows a direct comparison of the backscattering variability during the first part of the season, avoiding misalignments due to different ground roughness in different maize fields. The minimum equal to zero corresponds to the context of bare soil. The maximum equal to 1 corresponds to the maximum of VH/VV ratio and then to the highest vegetation volume scattering. The *IPR* from pixels corresponding to each maize field (classified according to the procedure that will be described in Chapter 4.2.3) were averaged for each acquisition day, to calculate the mean daily *IPR* of every maize field.

Although the normalized combination of VV and VH has already been used for crop phenology monitoring [105], to the best of our knowledge, this is the first time that a noise-filtered index based on the normalized VH/VV was directly used to retrieve crop-specific emerging periods.

Sentinel-2

The Sentinel-2 constellation provides optical data at the 10 m × 10 m spatial resolution every 5 days (**Figure 22c**). Many indices for terrestrial monitoring can be derived from the optical information. In this Chapter, the NDVI (Normalized Difference Vegetation Index) was used for the monitoring of vegetation changes in terms of optical and infrared signals. The NDVI index is defined as [126]:

$$NDVI_i = \frac{NIR_i - RED_i}{NIR_i + RED_i} \tag{11}$$

where *NIR* and *RED* are the Near InfraRed and the *RED* reflectance respectively, for each i-th maize field.

The Theia-Land web service provides 10 × 10 m cloud free NDVI data, correcting the atmospheric effect from Sentinel-2 measurements [127]. The NDVI time series were calculated by averaging the pixels corresponding to each maize field (classified according to the procedure that will be described in Chapter 4.2.3) and interpolating the mean values for each Sentinel-2 acquisition [111] [17]: a linear interpolation was performed to retrieve NDVI grids for the days between two consecutive sets of data, since NDVI changes are mainly driven by the phenological growth of plants.
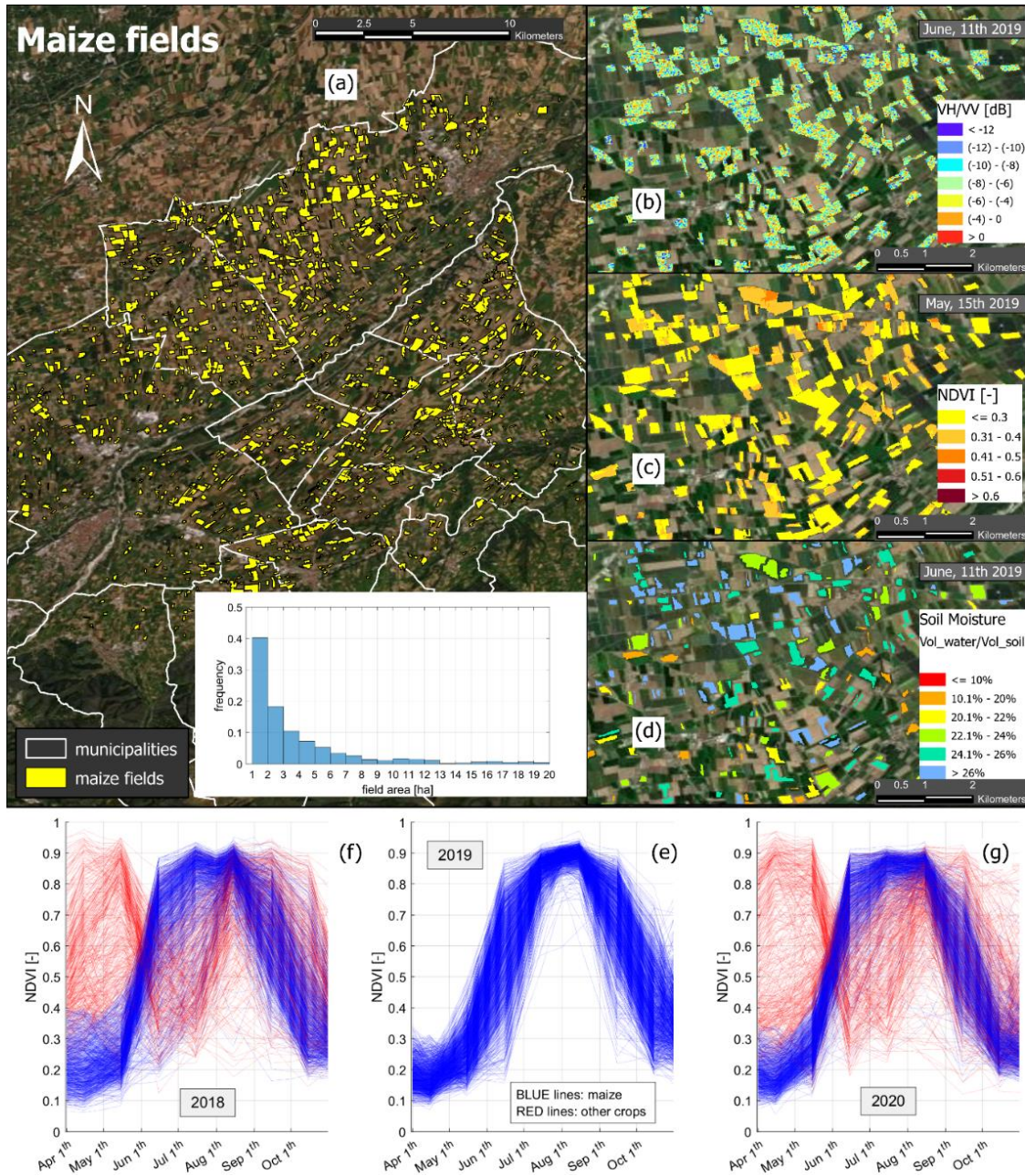
Figure 22. (**a**) Spatial distribution of maize fields over the studied region and frequency distribution of field areas. (**b**) Example of VH/VV 10 × 10 m data over the maize fields. (**c**) Example of NDVI 10 × 10 m data over the maize fields. (**d**) Example of soil moisture 10 × 10 m data over the maize fields. (**e**) NDVI series for 1154 fields classified as "maize" in 2019. Comparison with NDVI from same fields in 2018 (**f**) and 2020 (**g**).

Soil Moisture satellite products

The surface soil moisture (SM) was estimated by El Hajj et al. [128] from a synergy between the Sentinel-1 SAR and Sentinel-2 optical data and using neural network techniques. The S²MP product (Sentinel-1/Sentinel-2 Moisture Product) provides gridded data of soil water content [Vol_{water}/Vol_{soil}] over agricultural areas with 6-days frequency and a spatial resolution of 10 m × 10 m (**Figure 22d**). The S²MP data used in this Chapter were downloaded from the open access service of Thisme Data Service [129]. The S²MP operational data refer to the upper soil layer (3–5 cm) and are derived both from the ascending and descending orbits of Sentinel-1, passing at the zenith at around 5:30 pm (ascending) and 5:30 am (descending) respectively. The SM information derived from the descending orbit was not used, to avoid the effect of morning dew, in agreement with Le Page et al. [18]. The backscattering coefficient used for the S²MP estimation was obtained combining the contributions from vegetation and soil. The accuracy of the S²MP estimation was estimated to be about 6% for dry soils and up to 6.9% for very wet soils [128] and the RMSE was 1.5% higher for NDVI increasing from 0 to 0.75. The S²MP product can be applied for NDVI lower than 0.75 (for denser vegetation covers, the backscattering signal appears to be too attenuated to provide good SM estimations).

4.2.3 Classification of maize fields

The classification of agricultural fields was based on the geo-referenced information from the cadastral geodatabase of Regione Piemonte [130], which provides the shape files of all the cadastral parcels for the pilot area. First, the parcels representing agricultural areas were identified matching the cadastral shape files and the annual attribute tables from the agricultural registry of Regione Piemonte [131], which collects the annual farmer's declarations of land use. Combining this information, each agricultural parcel was classified according to the declared cultivated crop for year 2019.

A NDVI-based filtering was performed to improve the accuracy of the maize classification: despite the shapefile of cadastral parcels identifying the maize areas, the area of many of these parcels also has non-agricultural elements (e.g., gravel roads, farms buildings, rows of trees). The NDVI allows consideration of only the actual agricultural pixels in each parcel, as well as checking the quality of the cadastral classification. The shape files were converted in a 10 × 10 m raster to match the resolution of NDVI data from Theia. The pixels within the shape mask of maize parcels were analyzed in terms of NDVI response to define the borders

of actual maize parcels based on the NDVI signal. The values at 15-day intervals have been interpolated to obtain a daily signal from April to October.

According to El Hajj et al. [24], fully developed maize can reach NDVI values higher than 0.7, while the NDVI values for bare soil are typically lower than 0.3. The preliminary-classified parcels were filtered by selecting those areas with at least 2 weeks of bare soil in the spring period (April–June) and with an increasing NDVI signal reaching values higher than 0.7 for at least 3 weeks between July and September. As a result of the filtering procedure, 1154 fields were obtained. The spatial distribution of maize fields on which the analysis described in this study is based is shown in **Figure 22a**, as well as the frequency distribution of the areas of the fields. As shown in **Figure 22e**, the NDVI series show an initial development of maize plants starting in May–June, when the optical index shows increasing values from 0.3 to 0.7. The maximum development of maize plants results for the period between late July and the first half of August.

In order to verify the effects of annual crop rotation (a widely adopted practice in this region [132]), the NDVI-based classification was performed on the same 1154 parcels for the years 2018 and 2020. As shown in **Figure 22e** the NDVI analysis highlights that all parcels behave uniformly in 2019, indicating a correct crop classification for 2019, which is the reference year for the cadastral classification. In contrast, 34.3% of the fields cultivated with maize in 2019 were shown with different crops in 2018 (**Figure 22f**); the percentage was even 36.1% in 2020 (**Figure 22g**).

An EO-based spatial analysis has been carried out to check for the presence of rainfed maize. Since the availability of irrigation infrastructures can have a significant impact on agricultural practices, it is important to determine if sowing calendars should be discussed separately for irrigated and rainfed maize. In this Chapter, 159 potential rainfed maize parcels were identified, selecting those outside the irrigation districts and at least 100 m from the closest irrigation channel. Still, it is possible that irrigation from water wells is operated. The results of this analysis are discussed in Chapter 4.3.1.

The NDVI responses from each maize parcel have been analyzed from April to October and matched with the radar backscattering signal during the same period. The signals from the parcels within the irrigation districts were compared to the signals from other parcels, to highlight the effect of irrigation: during the dry periods, the NDVI from rainfed maize is expected to be lower than from the irrigated maize, where the stress effect is mitigated by irrigation. Likewise, the SAR backscattering can detect differences between rainfed and irrigated parcels, being sensitive to the vegetation water content.

The soil moisture data described in Chapter 4.2.2 were used to check for rainfed maize. For each parcel, the mean soil moisture was calculated for the period from May to July. The mean NDVI was calculated likewise on each field for the same

growing period. According to the assumption that irrigation allows maintenance of higher levels of soil moisture during dry periods, as well as higher NDVI responses, the mean soil moisture and NDVI were compared for the parcels within the irrigation districts and those far from irrigation infrastructures.

4.2.4 Identification of crop emergence and sowing periods

The backscattering and NDVI signals were analyzed during the maize growing season. The sensitivity of the VH/VV signal was exploited to identify the emergence periods of maize (EP), i.e., the time at which the germinating plant emerges from the ground and starts to grow. According to the NDVI series, the initial growing phase develops during May and June. Even if the NDVI signal suggests some fields are already sowed during April, the analysis of backscattering signal was performed from May, to avoid the uncertainty related to the fields still cultivated with winter crops in April.

The *IPR* daily signal was compared to the NDVI for two growing stages: the initial and growing phase (May–June–July) and the middle-final phase (August–September–October). The two phases were defined according to the mean NDVI values. From May to July the NDVI increases because of the cover development, reaching the maximum between July and August. In the last three months, the NDVI gradually decreases because of the chromatic change of maize leaves, up to rapid and strong variations indicating net changes corresponding to the harvesting times.

The EP periods were identified through an approach based on the analysis of the IPR signal. The bare soil period was identified for each field, according to the NDVI data, and the IPR backscattering signal was calculated for this period to identify the noise from moisture and roughness variability in bare soil. For each field, the noise induced by bare soil was removed from the IPR signal for the complete growing season, as described in equation 12:

$$IPR_f = IPR_{GS} - \frac{\sum_{lbp} IPR}{lbp} \tag{12}$$

where *IPR* is the normalized VH/VV backscattering (non-dimensional), IPR_f is the filtered *IPR* obtained by removing the backscattering from pure bare soil, IPR_{GS} is the IPR backscattering during the growing season (*GS*), and *lbp* is the length of the period before plant emergence [days]. The filtered normalized backscattering, expressed as Polarimetric Ratio Index (IPR_f) should have values close to zero until the plants start to grow out from the ground.

The EP was assigned to each field according to the time in which the IPR_f signal exceeded the 0.1 threshold. This cut-off value was fixed according to the uncertainty associated with the radar signal [133].

The maize sowing periods (SP) were inferred from the EP, considering the daily air temperature and the soil moisture conditions in the days before the emergence, as previously done by Nasrallah et al. [105]. According to the method described by Swan et al. [134], the days needed by the planted seeds to emerge from the ground were computed calculating the daily Growing Degree Units (GDU) [°C]. This indicator, also named Heat Units, describes the relation between crop development and the daily temperature. The heat accumulation, calculated considering the daily minimum and maximum temperatures, is used to measure the time required by crops to reach specific development phases.

Several authors provide estimations of the total GDU required by the maize plants to emerge through the soil: Darby and Lauer [135] calculated a GDU requirement of 69.4 °C while Abendroth et al. [136] suggested a range between 50 and 66.7 °C. For maize cultivated in the Eastern part of Po Valley (North-East Italy), a GDU requirement of 61 °C was proposed by Berti et al. [137]. In the present work, a mean GDU requirement of 62.9 °C was assumed as reference value for maize to reach the emerging phase, to be consistent with general recommended values and specific GDU estimated for Northern Italy. The daily GDU were calculated as

$$GDU_i = \frac{T_{max,i} + T_{min,i}}{2} - T_{base} \tag{13}$$

where GDU_i are the growing degree units for the *i*-th day [°C], T_{max} and T_{min} are the maximum and minimum air temperatures for the *i*-th day and T_{base} is the low threshold temperature required for maize growth. According to the guidelines from the University of Wisconsin [138], T_{base} was assumed equal to 10 °C and the upper and lower limits for daily T_{max} and T_{min} were fixed to 30 °C and 10 °C respectively. Daily temperature data provided by Arpa Piemonte [139] were used to determine the daily GDU for each field. The daily GDU were cumulated backwards from the emergence days to reach the required amount of Growing Degree Units for the crop emergence: for each field, the day on which the cumulative Growing Degree Units reached 62.9 °C was chosen as the sowing date.

According to Schneider and Gupta [140], soil moisture (SM) can affect the total GDU required by maize to reach emergence: for moisture values below the optimum in the seeding-zone, 16.7 °C should be added to the amount to be reached. Even if the impact of soil moisture occurs only in very dry periods, the optimum condition of soil water content is an important factor for the choice of sowing dates by farmers: for this reason, the impact of soil moisture on the length

of emerging periods was considered in this study. The gridded moisture data from Theia (described in Chapter 4.2.2) were used to identify moistures below optimum conditions. The upper limit of soil moisture was set for each field considering the maximum value from January 2018 to October 2021: these values were assumed as the field capacity of each field. According to the methodology described by FAO [7], each crop reach water stress conditions when soil moisture reaches values lower than specific fractions of field capacity: the FAO guidelines suggest that maize reaches stress conditions when soil moisture is lower than 45% of field capacity. The mean soil moisture during the 20 days before the plant's emergence was calculated over each field: for the fields where the mean SM was found lower than 45% of field capacity, the GDU requirement of 62.9 °C was increased by 16.7 °C.

4.3 EO-based description of maize growing cycle

The outcomes of the analysis are described in this Chapter and summarized as follows. First, the results of the irrigated/rainfed classification (Chapter 4.3.1) show that maize can be uniformly considered irrigated on the pilot area; in fact, the analysis performed on the fields in and outside the irrigation districts did not point to any relevant difference in the satellite time series. The results from the analysis performed throughout the growing season arei discussed in Chapter 4.3.2, comparing the potential of optical and SAR data to retrieve information for different growing phases. The maize sowing periods (SP) are reported and discussed in terms of emergence periods of maize plants detected from SAR information, and the derived distribution of actual SP over the pilot area (Chapter 4.3.3).

4.3.1 Identification of potential rainfed fields

The maize parcels within and outside the irrigation districts (respectively called "in ID" and "out ID" in this Chapter) were compared in terms of NDVI and VH/VV series. This comparison was performed to identify differences between the two graphs, in order to potentially calculate separate SP for rainfed and irrigated scenarios. As shown in **Figure 23**, the 0.25, 0.50 and 0.75 quantiles of the signals from the maize parcels were computed every 6 days, to be consistent with the SAR frequency of acquisition. The quantiles series do not show any significant difference between the two groups of parcels. Despite the 0.95 and 0.05 quantiles of NDVI showing a different range of values in June and September, this misalignment can be explained considering the differences between the two sets of parcels: in fact, less than 14% of maize parcels were considered as potentially

rainfed. In addition to the numerical difference between the two groups, the potentially-rainfed parcels are concentrated in areas at higher elevations and along the rivers, while the irrigated parcels are more uniformly distributed over all the pilot area.

Time series of mean NDVI and VH/VV were obtained from daily mean values from **Figure 23**. The NDVI mean signal from parcels within the irrigation districts is consistent with the mean signal calculated for the other parcels. The VH/VV comparison highlights a slight difference between the two groups from April to May: the VH/VV from parcels within the irrigation districts is −0.6 dB lower, considering the mean for the two months. However, this misalignment can be considered a consequence of the noise induced by the bare soil geometry, since the difference gradually reduces when the VH/VV become more sensitive to the growth of the plants.
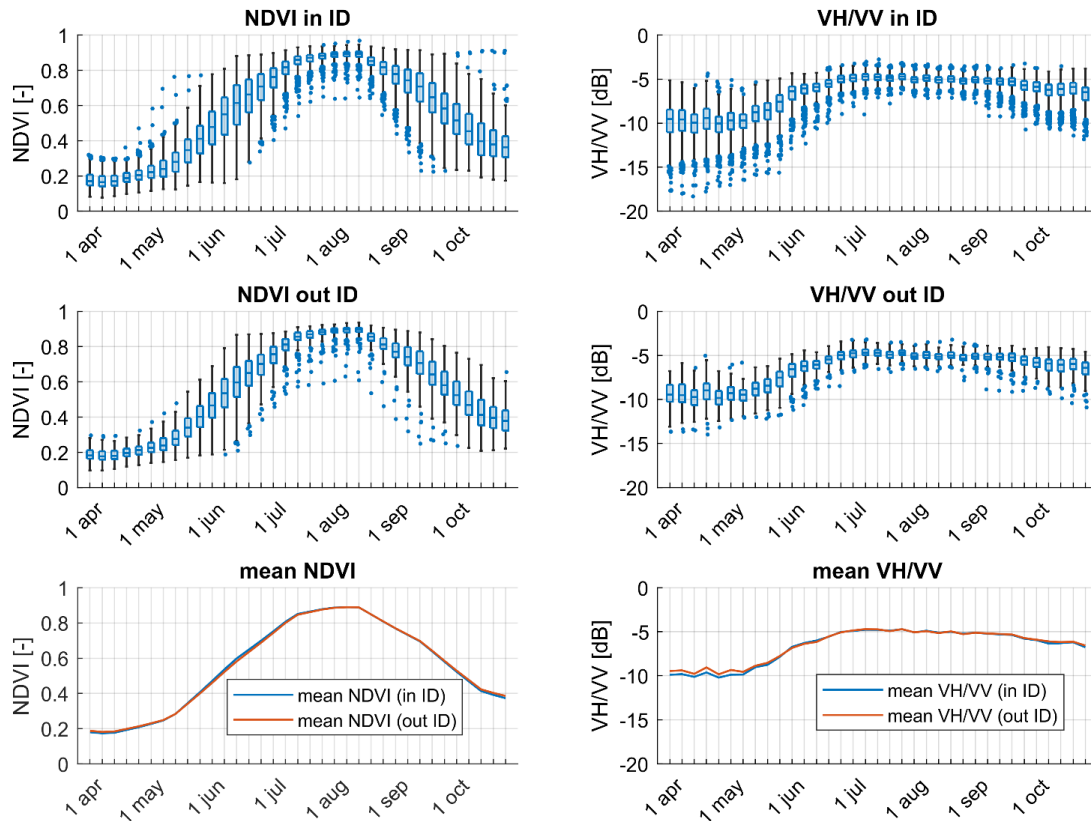
Figure 23. Time series of NDVI values (interpolation of 15–days revisit time) and VH/VV backscattering signal (6–days revised time). Each boxplot represents the distribution of values of NDVI and VH/VV from all the maize fields. The horizontal blue lines in the boxplots represent the 25%, 50%, and 75% quantiles, respectively (from the ground up). The black lines above and under each boxplot include the values within 95% and 5% quantiles, respectively. The blue dots represent the outlier values. In the two lowest subplots the mean daily values of the series are reported.

A further comparison was performed between the two groups of fields, considering the complete series of NDVI and VH/VV among the growing season. Even if the temporal mean signals from the two groups of parcels are well aligned, the effect of irrigation could lead to more evident divergences considering the long-term effect during the full growing season. The sum of the mean daily NDVI from April to October was compared for the fields inside and outside the ID: a misalignment of −0.01% was found between the sums of the two mean NDVI signals. The same analysis shows a misalignment of −1.7% from April to October between the sum of mean VH/VV within and outside the ID, and a misalignment of −0.4% considering the period from June to October (when the irrigation season is concentrated, and the effect of bare soil is limited). In both cases, the analysis did not point out any appreciable differences between the two groups of fields.

The monthly correlations between NDVI and VH/VV were calculated for the two groups of parcels, to identify potential impacts of irrigation limited to the areas of the irrigation districts. The analysis was performed for the first part of the maize growing cycle, when the VH/VV is still sensitive to the soil moisture anomalies induced by irrigation since growing plants still do not cover entirely the ground. **Table 9** shows the monthly Pearson correlation coefficients (obtained dividing the covariance by the product of the two variables' standard deviations) considering all the signals retrieved every 6 days from all the parcels of each group. The mean monthly NDVI was also compared with the mean soil moisture retrieved over the two groups of parcels. The comparison does not show any appreciable difference between the maize parcels cultivated within or outside the irrigation districts.

Table 9. Columns 1-2: Pearson correlation indexes (R) between NDVI and VH/VV. For each month from April to July, the optical and radar responses were compared, considering all the maize parcels and a 6-days frequency. R was calculated for the group of parcels within and out from the irrigation districts (IrD). Columns 3-4-5-6: comparison between mean monthly NDVI and soil moisture for the parcels within and out from the irrigation districts (soil moisture as % of water per unit of soil, in the upper 3-5 cm).

Month	Correlation between NDVI and VH/VV		Comparison of NDVI and soil moisture (SM)			
	R (in IrD)	R (out IrD)	NDVI (in IrD)	NDVI (out IrD)	SM (in IrD)	SM (out IrD)
April	0.2	0.2	0.21	0.22	0.24	0.26
May	0.62	0.6	0.46	0.45	0.22	0.23
June	0.64	0.66	0.71	0.68	0.2	0.2
July	0.23	0.21	0.84	0.83	0.17	0.18

4.3.2 Growing phases

The analysis performed throughout the growing season showed some relevant results in terms of optical and radar performance in the monitoring of maize growth. The comparison between NDVI and VH/VV shows a good alignment in the remote sensing responses during the initial growing phases, as shown in **Figure 23**. From May to July the NDVI increases from about 0.2 to the maximum values (0.75–0.9) and the VH/VV backscattering also increases from −10 dB to −5 dB on average. Although the NDVI decreases significantly during the final phase (September–October), there is no evidence of an analogue decrease in terms of backscattering. Since the NDVI is derived from visible and near infrared frequencies, the strong decrease is driven by changes in the chromatic response of maize leaves. However, the VH/VV does not appear to be affected by an analogous decrease during the same period; in fact, the backscattering signal is sensitive to changes in the ground coverage structure and water content.

Since VH/VV shows a low decrease during September and October, we can assume that this response is driven by the reduction of plant water content and the progressive drying of maize leaves. Yet, the signal decreases "slowly" because of the presence of dry biomass on the ground inducing volume scattering. This misalignment between NDVI and radar backscattering in the final part of the growing season is particularly meaningful for those algorithms retrieving soil moisture values based on NDVI information: since the plants' height affects the reliability of soil moisture results, these models usually suggest specific ranges of NDVI for which the soil moisture can be used. However, according to the results from **Figure 23**, any information whose reliability is affected by the plant coverage would be more robust taking into account the response of the dry biomass in terms of the global radar backscattering.

The maize growth was also analyzed in terms of the normalized backscattering signal (IPR). The scatterplots in **Figure 24** show the relation between IPR (i.e., the normalized VH/VV backscattering) and NDVI along two main growing phases. In the first growing phase (May–June–July), most of the maize fields appear to be already sowed and the development of plants corresponds to the NDVI changes and the IPR response. NDVI increases are due to the visible and near infrared signals of the land cover.

In the first part of the phase, when the NDVI is still lower than 0.25 (bare soil), the variability of IPR is mainly due to changes in the soil moisture and roughness due to the incipient growth of maize plants. The first consequence of maize emerging, before any response in terms of NDVI, is the change of soil roughness, to which the normalized backscattering is very sensitive.
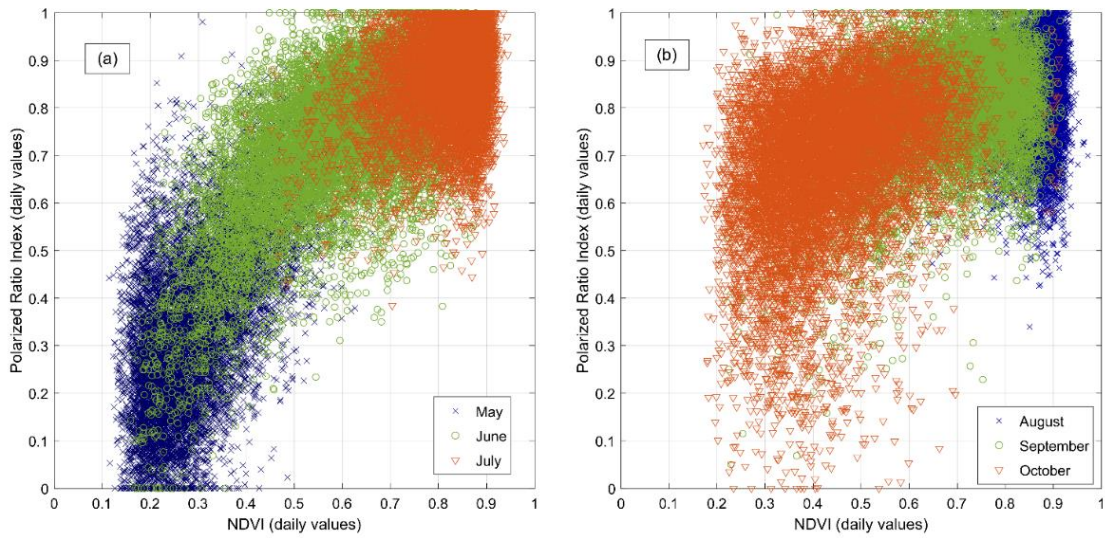
Figure 24. Comparison of daily NDVI and daily Polarized Ratio Index (*IPR*) over maize fields, for different growing stages: (**a**) May, June, July; (**b**) August, September, October. Each point represents the comparison between daily NDVI and IPR for a specific field. During the middle and final phase, plants have now reached the maximum stage of development (NDVI variability is very low and mainly due to plant health status) and the crop response in terms of NDVI is due to the change of plant color and to the final harvesting.

NDVI is more sensitive to chromatic responses of vegetation coverages instead of roughness variability, and the seedlings of freshly born maize do not provide any significant change in the optical response during the early days of growth. In fact, as shown in **Figure 24a**, the daily comparison between NDVI and IPR highlights a range of values where IPR starts to grow quickly but NDVI appears to be less sensitive (i.e., May, during the first part of the growing season). The results in **Figure 24** show the distribution of daily NDVI and IPR month-by-month over the pilot area: the distribution of the IPR increments seem to indicate that the emerging phase starts in early May and continues up to late June; in fact, even if most of the blue crosses reach high values of IPR during May (**Figure 24a**), there are still some fields where the plants break through the soil during June (green circles, **Figure 24a**).

During the second period, from August to October (**Figure 24b**), the NDVI starts to decrease because of changes in the chromatic response of maize leaves. During August plants have reached the maximum height of development and there is no significant NDVI variability (blue crosses, **Figure 24b**). Despite NDVI markedly changing in this period (values from 0.9 to 0.2), the daily variability of IPR appears to be lower.

The NDVI decrease from August to October is directly correlated to the vegetation's water content: maize plants become gradually drier during the final

phase of the growing season, with a different response in terms of red and infrared reflectance. However, the SAR backscattering depends both on the vegetation water content and the geometric structure of the ground coverage.

The misalignment between NDVI and IPR decreases is due to the sensitivity of the radar backscattering to dry biomass covering the ground, which limits the IPR variation compared to NDVI. Sudden decreases in the VH/VV signal to low values may be due to the maize harvesting over some of the fields, during September and October (orange triangles and green circles in **Figure 24b**).

4.3.3 Emerging of plants and sowing periods

In order to identify the periods in which maize starts to grow, the SAR data were analyzed for the period from May to June. The mean and variance of VH/VV over time in each parcel are shown in **Figure 25**: each point in the scatterplot represents the VH/VV statistics from May to June, colored according to the mean NDVI calculated for the same period.
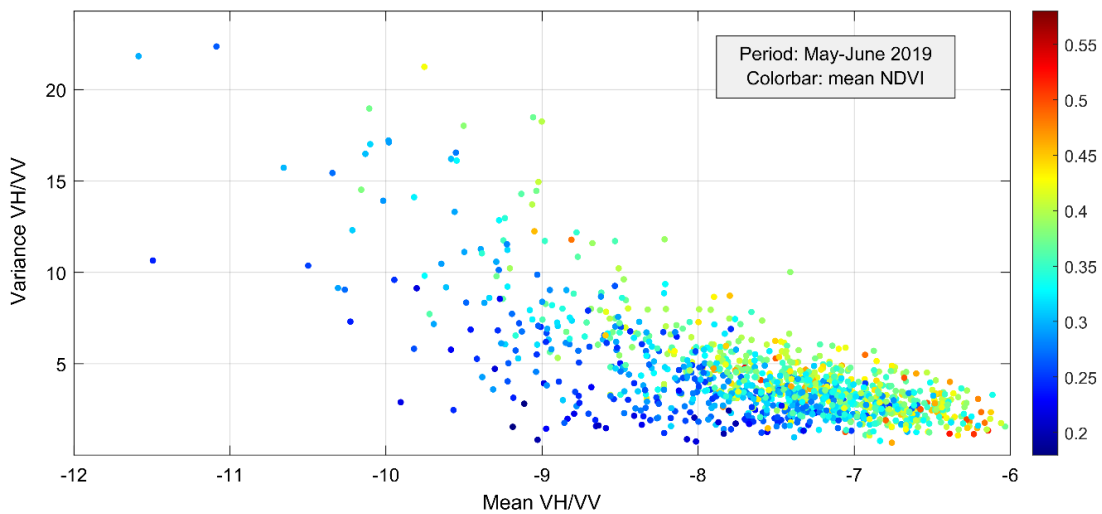
Figure 25. Comparison of radar backscattering mean and variance during the initial period of maize growth. Each point represents a maize parcel during the period from May to June, colored according to the mean NDVI for the same period.

Fields where maize is sown in the early May (or even in April) show a lower variance of VH/VV, because the growth of plants tends to produce a uniform field coverage. For the same reason, the early sowed fields show a higher mean backscattering and a higher mean NDVI, because the growing phase is at a later stage and plants are more developed. The presence of different mean NDVI classes over the May–June period may indicate that maize was sowed in distinct phases. About 25% of maize fields appear to have a mean NDVI lower than 0.3 in the first

two months: for these fields, the NDVI series typically assumed values higher than 0.3 during April, meaning that winter crops planted on the same plots before maize were probably still cultivated until this time.

The high values of VH/VV variance are typical of scenarios where maize plants break through the soil. The low height of plants corresponds to low NDVI and radar backscattering, but also to high variability of ground coverage due to the incipient growing phase.

The normalized backscattering signal (*IPR*) was filtered to limit the sensitivity of radar data to the moisture variability of bare soil, according to the procedure described in Chapter 4.2.4. The variability of the filtered signal (*IPR$_f$*) is mainly related to the geometric changes of the ground surface, which is related mainly related to the emerging of maize plants during the first part of the season. Therefore, the temporal analysis of *IPR$_f$* allows identification of the time at which plants emerge from the ground. The emergence time was identified according to the series of *IPR$_f$*, checking the time in which the filtered backscattering exceeds the threshold of 0.1. The bar plot in **Figure 26** shows the distribution of the emergence periods (EP).
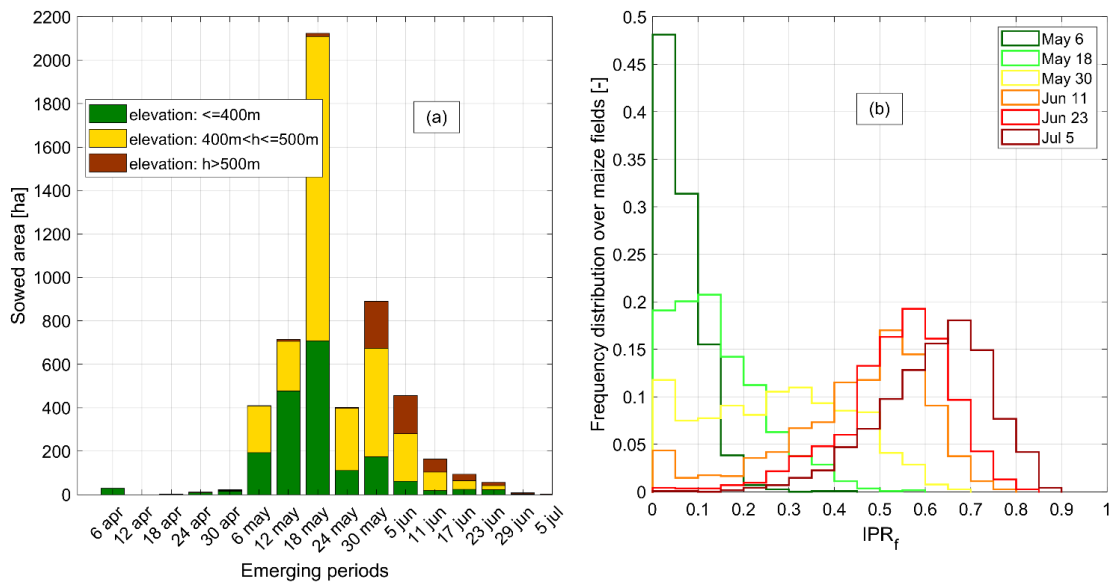
Figure 26. (**a**) Temporal distribution of emergence periods (i.e., the periods when the plants emerge through the soil). The 6–days revised time refers to the availability of radar data that were used for the analysis. For each day, the hectares where the plants have come out from the ground have been cumulated according to the class of elevation (meters above the sea level). (**b**) Temporal variation of the IPR$_f$ frequency distribution. After the end of June, no more fields show values < 0.1, showing that the maize has passed the emergence phase.

Most of the maize starts to grow out of the soil surface during the second half of May, especially in the days before the 18th of May. The distribution of EP highlights the presence of a second main emergence period, between the last days of May and the beginning of June.

It is interesting to observe that sowing of maize at low elevations (h < 400 m above the sea level) appears to occur earlier than at higher elevations, with highest elevations (typically h > 500 m) characterized by plants breaking through the soil between the of May and mid-June. This fact is consistent with the lower temperature at higher elevations.

The presence of two different SP is consistent with the typical agricultural practices of the area, where winter crops are harvested in late spring. These crops may be present on those parcels sowed later at the lower altitudes, while the time shift at high elevations may depend by the later warming of weather conditions.

Despite some areas appears to be sowed in the first week of April, this practice is not widespread over the region. The early sowing is mostly related to the grain maize, which requires longer periods to grow and reach the optimum water content in the final product at the end of the season, and to local insurance policies that refund maize farmers in case of late frosts in April.

According to the methodology described in Chapter 4.2.4, the actual sowing dates were estimated by inverting the method for the calculation of the emerging period from the sowing date, according to daily temperatures and soil moisture conditions. Considering that emergence periods can be calculated on a 6-days interval, because of the revisiting time of Sentinel-1 data, the estimation of actual sowing dates is affected by the same uncertainty; in **Figure 27** results are presented with such temporal resolution.

More than 52% of maize areas are sowed in the last six days of April, especially in the northern municipalities where this percentage is higher than 70% (e.g., 78% in Fossano, 73% in Sant'Albano Stura). About 9.1% of maize fields are sowed in the remaining days of April. About 30% of maize areas were sowed in the second half of May and at least 9% during the first half of the month.

The spatial distribution of maize SP highlights that, on average, the fields at lower elevations are sowed earlier (see the DTM map in **Figure 21b**). A statistical analysis was performed to calculate the correlation between the SP and the topographic elevation: the 6-days intervals, consistently with the Sentinel-1 revisiting time, were numbered for year 2019 (e.g., April 13th–18th interval is the 18th group of 6 days); for each field, the numbered 6-days sowing period was compared to the elevation (in terms of meters above the mean sea level). However, the Pearson correlation coefficient (R), which quantifies the correlation strength between two sets of variables (ranging from 0 to ±1), shows a moderate positive correlation of 0.41 between sowing periods and topographic elevation (according to the classes of correlation proposed by Evans in 1996 [141]).
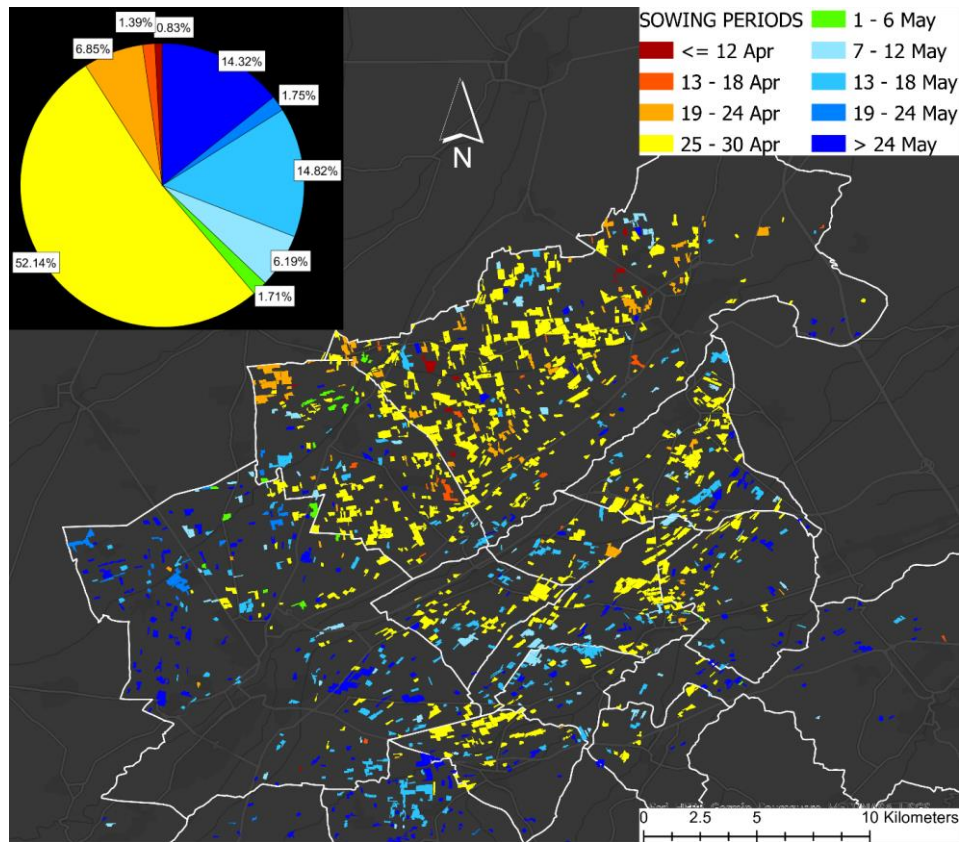
Figure 27. Spatial distribution of sowing dates at 10x10 m resolution. The sowing periods are grouped by 5-days classes. The spatial variability confirms the SAR analysis of emergence periods: for lower elevations, maize is sowed earlier on average.

In fact, despite an evident gradient of sowing periods moving from lower to higher altitudes, a significant part of fields at low altitudes appears to be sown during May. This can be explained by some declarations from local farmers, stating that fields at low elevations have a higher probability to be cultivated with winter crops until April: this could be the main reason for the coexistence of fields sowed on early April and late May at elevations < 450 m above the sea, where medium temperatures are higher.

This result is consistent with the information provided by local farmers (interviewed by the authors in November 2021) who declared that maize is usually sowed twice per season, in April and May, according to the plant variety and the final use the product. The maize sowed in April is usually a high-quality product for the food market, while the plants sowed in May are those to produce mash corn for farm animals. The results obtained in this study fit well with the available sowing information described by previous studies in Northern Italy. Berti et al. [137] collected sowing periods over 6 sites in North-East Italy, from 2005 to 2007: local farmers declared that maize was mostly sown during late April in 2005

(sowing occurred between 27 April and 1 May in 3 of the 6 sites). Despite a slight temporal variability, this study states that most of the maize was sown in April also in 2006 and 2007. Even if the data were collected in the eastern part of Po Valley, the agricultural practices can be assumed as sufficiently uniform in the densely cultivated region of Northern Italy. Moreover, also the regional calendar provided by Azar et al. [142] considers April as the sowing month for maize in Northern Italy, and the second week of May as the reference beginning of the growing phase.

Although global sowing calendars can only be used as general reference information and not as actual data for validation, the results obtained in this study fit well with the large-scale SP for irrigated maize provided by the crop calendars from FAO [107] and MIRCA2000 [41]. The FAO calendar indicates April as main sowing month for irrigated maize, with high probability that a small part of irrigated croplands may be sowed later. The U.S. Department of Agriculture provides monthly information for crop-specific sowing dates worldwide [143]: this calendar suggests April as sowing period for maize in Italy.

The main limitation of this approach is the lack of information about actual sowing dates at the field scale, to perform a high-resolution validation: right now, results can only be compared with local declarations from farmers and large-scale calendars. As previously mentioned, local farmers were asked to answer a survey to get an overview of the maize cultivation practices in the pilot area, in order to partially fill this gap. The results of the survey are available in Appendix A, within the supplementary material of this study. Although this source is too scattered to be used for an actual validation, the information collected from farmers was a valuable source in giving confirmation of the results.

4.4 Concluding remarks

The sowing period has been proven to have an important impact on the yield of many of the most common crops, especially cereals. Moreover, the shifting of agricultural sowing periods is increasingly used as an adaptation strategy to climate change.

In this Chapter, the reliability of Earth Observation to retrieve maize sowing periods was tested, analyzing a pattern of 1154 fields within a 30 × 30 km area in Piedmont (North-West Italy) for year 2019. Radar and optical acquisitions from Sentinel-1 and Sentinel-2, respectively, were used to classify maize fields and to detect crop emergence through the soil, building up the spatial distribution of sowing periods at the field scale. For this reason, a SAR-based normalized index (named Polarimetric Ratio Index, *IPR*) was proposed in this study, in order to detect the geometric changes on ground surface induced by maize emergence.

Results show that in 2019 maize was sown within April and May: about 52% of maize hectares were sown between April 25th and 30th, and 31% from May 13th to the end of May. The late sowings are more frequent at higher elevations: a moderate correlation was found between emergence delay and elevation above the sea level (Pearson correlation coefficient, R = 0.41). The maize sowed in May at lower elevations is likely cultivated on those parcels where winter crops are harvested in late spring, according to a widespread agricultural practice in this area.

The comparison with actual data of local sowing practices highlights a good alignment with sowing periods occurring in the Po Valley in previous years (period 2005–2007). Results fit well with the sowing periods declared by local farmers within a survey conducted by the authors, in which the second half of April and May were indicated as the two main sowing periods. Results from this study are also well aligned to the most widely used comprehensive crop calendars, such as the global dataset of sowing periods proposed by FAO.

Although the combined use of SAR polarizations has been previously used for agricultural applications, the novelty of this approach relies on the use of a normalized SAR-based index, which allows filtering out the effect of bare soil and clearer detection of the signals induced by crop growth. Further analyses combining more satellite constellations and ground information for validation, could exploit the EO-based methodology proposed in this study to assess more precise sowing periods for various crops.

For the future, even temperate areas are expected to suffer lack of water and yield losses, because of changes in the precipitation regimes and withdrawable water for irrigation. Remote sensing is a very useful tool to support effective adaptation strategies to climate change, especially in those regions where new agricultural mindsets are increasingly required.

Chapter 5

Conclusions

The research work described in this thesis exploits the potential of Earth Observations for the assessment of agricultural evapotranspirative requirements. Satellite technology proved to be a valuable tool for retrieving climate information, providing reliable solutions for agricultural applications and improving the accuracy large-scale hydrological modelling. The global food security is seriously threatened by climate changes since agricultural production is exposed to increasingly severe droughts and lacks of available freshwater for irrigation.

This research aims to take advantage of EO-based re-analysis data to describe the global climate-driven agricultural requirements, highlighting critical impacts and statistically significant trends. The research has some innovative aspects, since the water-soil balance model described in Chapter 2 was coupled with daily gridded information of precipitation and evapotranspiration; to the best of our knowledge, this is the first global assessment of crop water requirements driven by actual daily climate data over a 50-year period. Moreover, a method for the estimation of crop sowing periods and growth monitoring based on optical and radar data is also described in this thesis.

Assessing the agricultural stress and the water needed for irrigation has never been more important, since the availability of freshwater is seriously challenged as result of climate change. Effective water management policies and adaptation strategies have never been more urgent to limit the exposure of agricultural production to climate change. The widespreading of the "agriculture 4.0" concept lays the foundation of the next food production mindset, which will probably be highly dependent on our capacity to use technological tools for the crop management, including the EO sensors. In addition to this, the SDGs from the UN Agenda 2030 clearly point out the importance of ensuring food security to face the unprecedented cotemporary population growth.

The first Chapter of the thesis introduces the research questions and points out the background of the research field. Objectives and limitations are presented and discussed, in order to clarify the strengths and the weaknesses of the results. Moreover, a brief review of the most used satellite sensors for agricultural applications is presented. Most of the satellites equipped for EO missions retrieve

optical and radar measurements, according to the purpose of each space mission. An additional review of EO-based products for agricultural and hydrological modelling has been included in Appendix A.

In Chapter 2, the hydrological model for the computation of crop water requirement is presented. The soil-water balance is driven by daily data of precipitation and reference evapotranspiration, computing the crop-specific assessment of actual evapotranspiration. The hydro-climatic variables were retrieved from ERA5 reanalysis dataset from the Climate Change Service of the Copernicus European Programme, which provides tents of hourly gridded climate variables. The model was tested by assessing the global irrigation requirements of 26 main crops for year 2000 and comparing results with previous studies and national data of withdrawals for irrigation. In this Chapter, the methods for the daily aggregation of ERA5 data are described, detailing the computing and the calibration of reference evapotranspiration; the procedure used to match the spatial resolution of ERA5 (0.25° x 0.25°) and MIRCA2000 (0.0833° x 0.0833°), i.e. the gridded crop dataset on which the assessment was based, is also discussed in this Chapter.

The irrigation requirement resulting from the model was found to be about 962 km^3 for year 2000, with a spatial variability mainly dependent on some key factors: the distribution of areas equipped for irrigation, the crop intensity (i.e. the indicator of multi-seasonal practices on the same areas), the kind of cultivated crops (e.g. rice has a high sensitivity to water stress and requires more irrigation compared to other cereals), and the lack of precipitation. The soil water balance also highlights that an important volume of rainfall (about 672 km^3) was lost as surplus over irrigated lands because of the seasonal distribution of wet days; this water is fed back to the hydrological cycle but does not contribute to satisfy the crop evapotranspiration needs. The distributed classification of irrigation requirement by classed of water risk highlights that South and East Asia are the regions most exposed to possible unavailability of water suitable for irrigation, in terms of quantity and quality. The estimations from this thesis were compared with national and sub-national data of withdrawals for irrigation: in both cases, good agreements were found, especially for the most densely cultivated nations; the comparison also pointed out very good alignment between our estimations and volumes of applied water and evapotranspirative demand estimated in California.

In Chapter 3, a comprehensive assessment of daily crop water requirements was performed to analyze significant trends of irrigation needs and water stress periods over the 1970-2019 period. The model described in Chapter 2 was used for this assessment, introducing some methodological updates to improve the accuracy of the estimations. First of all, a climate-based method for the assignment of soil moisture at the sowing date was introduced: in order to partially avoid

arbitrary assumptions, the gridded soil moisture data from ERA5 were used to define monthly mean values of soil water content, in order to initialize the growing season. A sensitivity analysis shows that final ET_a is 12% lower if the temporary crops are sown with wilting point conditions, compared with the opposite scenario at field capacity; a similar analysis shows that the difference is 3% for irrigation requirements, comparing the two sowing scenarios. Another improvement was the calibration of ET_0 over a multi-decade period, using a method improved from the one discussed in Chapter 2.

Results show that global irrigation requirements (I) changed heterogeneously from 1970 to 2019. Since the assessment was performed at the daily scale, it was possible to highlight significant trends of seasonal days requiring irrigation; the case of maize was analyzed in several sub-continental regions of the world, highlighting statistically significant increases of annual periods requiring irrigation in Europe, East and West Asia, Africa and Oceania; these trends are mainly driven by decreases of annual rates and frequencies of precipitation. The analysis of I annual rates shows that for more than 53% of irrigated croplands the irrigation needs have increased more than 10 mm/year over the 50-year period. Moreover, increments higher than 100 mm/year were found in Mediterranean Europe, Balkan peninsula, Ukraine, North-East China, the eastern part of Australia, Brazil, and the western part of U.S., comparing the mean rates of 1970s and 2010s decades. Crop-specific results show that most of the cereals cultivated in North America and Europe required more irrigation in 2010s than in 1970s (especially rice and wheat). The increase of irrigation requirements is progressively higher moving from North to South latitudes, particularly for cereals. India and Pakistan, however, show opposite trends and the irrigation requirements of the most cultivated crops generally decreased through the decades.

The assessment of actual evapotranspiration over rainfed croplands, where no irrigation inputs are supposed to avoid water stress during dry periods, the temporal analysis pointed out that 38.1% of areas are affected by statistically significant positive trends of annual water-stressed days; moreover, the length of stress periods has more than doubled from 1970s to 2010s on 6% of rainfed areas, while 16% of rainfed areas show a statistically significant increment of severe annual water stressed periods.

In Chapter 4, a synergic use of optical and radar data from the Sentinel constellation was used to retrieve actual maize sowing periods, and to monitor maize growing phases during year 2019. A 30 x 30 km pilot area was chosen in South Piedmont (Italy), characterized by temperate climate and an extensive network of irrigation channels and wells. Combining the local cadastral agricultural data and an NDVI-based classification, 1154 maize fields were identified and considered within the study. A radar-based index (Polarimetric

Ratio Index) was introduced to detect significant changes in the ground surface geometry of the fields, in order to identify the emerging periods of plants. The actual sowing periods were estimated according to the heath required by the seeds to germinate and break through the soil, considering the daily temperature measurements over the pilot area.

Results show a high reliability of local crop classifications, but only for the year to which the cadastral crop data refer; this is an effect of annual crop rotation practices. The analysis based on the Polarimetric Ratio Index shows that maize fields were sown between April and May in 2019. The 81% of sowings were concentrated in two periods: about 52% of maize was sowed between April 25th and 30th, 28% from May 13th to the end of May. Radar acquisitions turned out to be more sensitive to the dry biomass of maize in the final part of the growing season (August-October) than optical data. The actual sowing periods were found moderately correlated with the elevation above the sea level of the fields (R=0.41): apparently, maize is generally sowed later at higher elevations, which is consistent with the spatio-temporal distribution of optimum temperature conditions for planting. Moreover, the maize sowed in May and June at lower elevations is likely cultivated on those parcels where winter crops are cultivated up to late spring, according to the information retrieved from the local farmers (Appendix B).

Limitations

The limitations of this thesis are mainly due to the lack of information about the temporal variability of global crop distribution and growing calendars: most of the crop-specific information still refers to circa year 2000. Despite some authors provided information about temporal dynamics of agricultural areas, like the study by Siebert et al. [144] which describes the evolution of irrigated areas from 1900 to 2005, a few crop-specific information is actually available at large spatial scales: in particular, there is a lack of information of global datasets providing consistent information of crop distribution, multi-seasonal practices and growing calendars . Recent studies focused on this lack on information, providing gridded datasets of global crop-specific areas. For example, the SPAM2010 dataset [145] [146] describes the spatial distribution of agricultural areas of 42 major crops, both for rainfed and irrigated scenarios, including also gridded information of yield and agricultural production for circa year 2010; recently, the GAEZ+2015 dataset was published in order to provide updated information of irrigated and rainfed crop-specific areas, describing also multi-seasonal practices and sowing/harvesting calendars [147]. However, a coupled information of areas and growing calendars, which are very important for the assessment of water requirements, is rarely available.

Within the present analysis, the crop information from the MIRCA2000 dataset was used, detailing rainfed and irrigated scenarios, multi-seasonal practices and monthly calendars. The use of a fixed-in-time distribution of croplands (in this case, referred to circa year 2000) limits the possibility to assess the temporal variability of the water volumes required by agriculture over the world: for a volumetric analysis, the crop-specific cultivated area must be known, in addition to the rate of water requirements (expressed as water depth per unit of area). The lack of information about temporal evolution of croplands, limits the possibility to convert the water depth of evapotranspirative demand in a crop-specific volumetric requirement. However, the temporal variability of water requirement rates is a reliable indicator of the climate impact on agricultural evapotranspiration and can be used to analyze the role of climate change in the water stress variability in different regions of the world.

Another limitation is the lack of information about irrigation efficiencies. For year 2000 a good information of national and sub-national withdrawals for irrigation is also available. Yet, the comparison between the national withdrawals and the estimated requirements would also require some information about crop-specific irrigation efficiencies to validate the model accuracy. The efficiency is expressed as ratio between the irrigation ideally needed by crops and the volume of water withdrawn for irrigation. Without this information or some other distributed data of irrigation practices, the two quantities can only be compared in terms of orders of magnitude. However, some additional information was used in this thesis to partially fill the lack of efficiency information in some relevant areas. For example, the practice of "deficit irrigation" was checked for those nations where requirements were estimated higher than actual withdrawals. Some crops were also associated to very low efficiencies, explaining withdrawals extremely higher than requirements in those nations where these crops are widely cultivated (e.g., cultivations of rice in Japan determine a national mean efficiency lower than 0.1).

The analysis of local sowing practices is potentially a useful instrument to understand the dynamics of the crop planting, which is highly dependent on local policies and agricultural incentives (e.g. crop switch, annual crop rotation, change of single-crop variety) but also on the annual climate conditions. Moreover, a reliable tool for the estimation of local sowing periods could be an important source of information to check the reliability of large-scale calendars. The main limitation of the remote sensing-based analysis is the lack of information about actual sowing declarations from farmers or public authorities, which limits the possibility of validation at the field scale. In order to improve the applicability of the method proposed in Chapter 4, more crop-specific data should be collected at the field scale, in order to have a proper comprehension of the local pattern of planting periods.

Recommendations for future research

This thesis aims to contribute to the broad field of study that is the use of Earth Observation for large-scale hydrological assessments and agriculture monitoring. The use of reanalysis products to study the impact of climate variability on crop water requirements has proven to have a high potential for future studies. In fact, several future follow-up studies could be conduct on the basis of the model presented in this thesis and of the methods for the monitoring of crop growing phases.

In order to assess the temporal variability of volumetric irrigation requirements, a proper knowledge of how the crop-specific areas changed over the years. Recently, new large-scale agricultural datasets were published, providing new agricultural information for years after 2000 (e.g. irrigated and rainfed growing calendars, spatial distribution of multi-cropping practices, irrigated and rainfed yields). Future analyses could be performed in order to consider the volumetric variability of crop evapotranspiration and irrigation requirements, for which the temporal variability of crop areas is essential.

Future comprehensive assessments could be carried out using new re-analysis outputs, in order to improve the quality of the climate-drive estimations. Despite ERA5 proved to be a reliable dataset for large-scale agricultural and hydrological assessment, future comparisons of several re-analysis products could lead to the use of most recent releases of ERA5 (e.g. AgERA5, the product designed for agriculture which was recently released on the Climate Data Store of Copernicus) or to comparative assessments to evaluate the performance of climate data in different climatic regions and different regions of the world.

Due to the importance of water uses for agriculture to ensure future food security, the model presented in this thesis could be used to analyze possible future scenarios of climate-driven crop water requirements and related impacts on yields. The Copernicus Climate Data Store provides several datasets of large-scale projected climate data, considering different possible future carbon emissions. The model described in this thesis cold be a valuable instrument to assess the sensitivity of future crop yields to precipitation rates and frequency, temperatures and other climate variables, sowing and harvesting dates periods, presence of deficit irrigation practices and several other factors.

This research field has a great potential in terms of economic impacts. Agriculture is seriously threatened by climate change and technological services for mitigation and adaptation strategies are becoming increasingly popular also at the regional or sub-regional scale. Public authorities, farmers, insurance companies, are just some the many stakeholders which would benefit from the widespread of reliable EO-based tools. The model and the methodology proposed

in this thesis are currently being used for a sub-regional assessment of crop irrigation requirements in the Southern region of Piedmont, over the same pilot area discussed in Chapter 4. Regional data of crop distribution allows the analysis of agricultural water needs in terms of water volumes, in order to compare the estimates to the available water resources at the basin level. Moreover, a method for the detection of irrigation events over the same area is actually under development, based on the combined use of Sentinel-1 and Sentinel-2 information: within the Brobbio-Pesio district, actual daily information of irrigation volumes provided to the fields are actually available for some years, allowing a validation of the satellite-based estimations.

Finally, a strongest synergy between researchers, farmers and public authorities will be required in the future, in order to enhance the EO-based information. Some of the concepts and methods described in this thesis are currently at the basis of several projects aimed to provide commercial services, in order to transfer as much as possible research knowledge to develop operative tools for Agriculture 4.0.

Appendix A. List of main EO-based products

Table 10. List of main used precipitation datasets. The products are grouped according to the source of data (gauged-based, satellite-based) and a third group details the reanalysis EO-based products.

Precipitation dataset	Resolution	Frequency	Coverage	Period
Gauge-based Products				
CRU	0.5° x 0.5°	monthly	Global Land	1901 - present
GHCN-M	5° x 5°	monthly	Global Land	1900 - present
GPCC	0.5° x 0.5°	monthly	Global Land	1901 - 2013
	1° x 1°	monthly	Global Land	1902 - 2013
	2.5° x 2.5°	monthly	Global Land	1903 - 2013
GPCC-daily	1° x 1°	daily	Global Land	1988 - 2013
PREC/L	0.5° x 0.5°	monthly	Global Land	1948 - 2010
	1° x 1°	monthly	Global Land	1948 - present
	2.5° x 2.5°	monthly	Global Land	1948 - present
UDEL	0.5° x 0.5°	monthly	Global Land	1900 - 2014
CPC-Global	0.5° x 0.5°	daily	Global Land	1979 - 2015
Satellite-based Products				
GPCP	2.5° x 2.5°	monthly	Global	1979 - present
GPCP 1dd	1° x 1°	daily	Global	1996 - present
GPCP_PEN_v2.2	2.5° x 2.5°	5-daily	Global	1979 - 2014
CMAP	2.5° x 2.5°	monthly	Global	1979 - present
TRMM 3B42	0.25° x 0.25°	monthly	50°N - 50°S	1998 - present
TRMM 3B43	0.25° x 0.25°	daily/3-h	50°N - 50°S	1998 - present
GSMaP	0.1° x 0.1°	daily/1-h	60°N - 60°S	2002 - 2012
PERSIANN-CCS	0.04° x 0.04°	6-h/3-h/30-min	60°N - 60°S	2003 - present
PERSIANN-CDR	0.25° x 0.25°	daily/6-h/3-h	60°N - 60°S	1983 - present
CMORPH	8 km x 8 km	6-h/3-h/30-min	60°N - 60°S	2002 - present
GPM	0.1° x 0.1°	daily/3-h/30 min	60°N - 60°S	2015 - present
GPM+SM2RAIN	0.25° x 0.25°	daily	60°N - 60°S	2007 - 2018
MSWEB	0.1° x 0.1°	daily/3-h	Global	1979 - present
CHIRPS	0.05° x 0.05°	daily	50°N - 50°S	1981 - present
Re-Analysis Products				
NCEP 1	2.5° x 2.5°	monthly/daily/6-h	Global	1948 - present
NCEP 2	1.875° x 1.875°	monthly/6-h	Global	1979 - present
ERA Interim	0.75° x 0.75°	monthly/6-h	Global	1979 - present
ERA5	0.25° x 0.25°	monthly/1-h	Global	1950 - present

ERA5 Land	0.1° x 0.1°	monthly/1-h	Global Land	1950 - present
AgERA5	0.1° x 0.1°	daily	Global Land	1979 - present
20CRv2	2° x 2°	monthly/daily/6-h	Global	1871 - 2012
JRA-55	60 km	monthly/6-h/3-h	Global	1958 - present
MERRA	0.5° x 0.67°	daily	Global	1979 - present
MERRA Land	0.5° x 0.67°	monthly/daily/1-h	Global	1980 - present
CFSR	38 km	6-h	Global	1979 - 2010

Table 11. List of the most used global datasets of evapotranspiration. Datasets are grouped according to the type of ET (potential/reference or actual). Acronyms: PM: Penman-Monteith; SEBM: Surface Energy Balance Model; LSM: Land surface model; PT: Priestley-Taylor; SSF: Soil stress factor; SC: Surface Conductance; RS-SEB: Remotely sensed surface energy balance; SWB: Soil water balance; PML: Penman–Monteith–Leuning.

ET dataset	Resolution	Frequency	Period	Method
Global Reference & Potential ET				
CRU	0.5°	monthly	1901 - p	PM
ERA5	0.25°	1-h	1950 - p	SEBM
ERA5 Land	0.1°	1-h	1950 - p	SEBM
GLEAM3.3 PET	0.25°	daily	1981 - 2018	PT
MOD16 PET	0.5°	8 days	1981 - 2019	PM
PT-JPL	0.5°	monthly	1986 - 1995	PT
Singer et al. (2020) [148]	0.1°	1-h	1981 - p	PM
Global Actual ET				
ERA5	0.25°	1-h	1950 - p	SEBM
ERA5 Land	0.1°	1-h	1950 - p	SEBM
FLDAS	0.1°	monthly	1982 - p	LSM
GLDAS V20	0.1°	3-h	1948 - 2010	LSM
GLDAS V21	0.25°	3-h	2000 - p	LSM
GLEAM 3.3	0.2°	monthly	2003 - 2018	PT, SSF
GLEAM 3.3a	0.2°	monthly	1980 - 2018	PT, SSF
JRA-55	1.25°	3-h	1959 - p	SEBM
MERRA-2	0.5°	1-h	1980 - p	SEBM
MOD16A2 V105	1 km	8 days	2000 - 2014	PM, SC
MOD16A2 V6	500m	8 days	2001 - p	PM, SC
NTSG	8 km	monthly	1982 - 2013	Modified PM and PT
PML	500m	8 days	2002 - 2017	PML
SEBS	5 km	monthly	2001 - 2010	RS-SEB
SSEBop	1 km	monthly	2003 - p	PM
TerraClimate	0.25°	monthly	1958 - 2018	SWB

Table 12. List of the most used gridded datasets of global crop distribution.

Gridded crop dataset (source)	Variables	Crops	Coverage (spatial resolution)	Period (temporal resolution)
M3Crops (census)	Crop areas, yields	175	Global (0.0833°x0.0833°)	Circa 2000 (annual)
MIRCA2000 (census, model)	Crop areas, planting and harvesting months, irrigated and rainfed areas, crop intensities	26	Global (0.0833°x0.0833°)	Circa 2000 (monthly)
SPAM2010 (census, satellite and model)	Crop areas, yields, irrigated and rainfed areas	42	Global (0.0833°x0.0833°)	Circa 2010 (annual)
GAEZ (census, model)	Crop areas, yields, productions, non-crop-specific irrigated areas	23	Global (0.0833°x0.0833°)	Circa 2000 and 2010 (annual)
RiceAtlas (census)	Crop areas, production, planting and harvesting months	1	Global (2725 spatial units)	Circa 2010 (annual)
GFSAD30 (satellite, census)	Crop areas, irrigated and rainfed areas, crop intensities, crop change over 1990-2017	8	Global (30x30 m)	1990-2017 (monthly)
GDHY (census, satellite, model)	Yield	4	Global (0.5°x0.5°)	1982-2016 (seasonal)
SAGE (census)	Planting and harvesting dates	19	Global (0.0833°x0.0833°)	1990s or early 2000s
GAEZ+2015 (census, satellite, model)	Crop areas, planting and harvesting months, irrigated and rainfed areas, crop intensities	26	Global (0.0833°x0.0833°)	Circa 2015 (monthly)
GRIPC (census, satellite, model)	Rainfed and irrigated croplands, paddies extent	1	Global (0.0833°x0.0833°)	Circa 2015 (annual)

Appendix B. Survey among maize farmers in South Piedmont

In November 2021, five farmers from the Brobbio-Pesio irrigation district were asked to answer a survey about maize cultivation practices and use of irrigation water. This survey was performed to give consistency to the results discussed in Chapter 4.

Following are answers provided by the farmers to each question (e.g. F1: answer from Farmer 1).

Irrigation Practices

Question 1.   *Do you benefit from irrigation infrastructure for maize cultivation?*

      F1.   Yes, I use water provided by the Brobbio-Pesio irrigation channels.

      F2.   Yes, I use water provided by the Brobbio-Pesio irrigation channels.

      F3.   Yes, I use water provided by the Brobbio-Pesio irrigation channels.

      F4.   Yes, I use water provided by the Brobbio-Pesio irrigation channels and additional water from private wells.

      F5.   Yes, I use water provided by the Brobbio-Pesio irrigation channels.

Question 2.   *If the answer to Question 1 is "yes", what irrigation techniques are used?*

      F1.   Surface irrigation.

      F2.   Surface irrigation.

      F3.   Surface irrigation. I know that other consortia are switching to drop irrigation and pivot irrigation.

      F4.   Surface irrigation using water from the irrigation channels and drop irrigation using water withdrawn from wells.

      F5.   Surface irrigation.

Question 3.   *Maize fields are usually irrigated according to the authorization calendar (i) regardless of the availability of rainfall water; (ii) just in case precipitation was not optimal?*

F1.   Maize field are only irrigated during dry periods, according to the authorization calendars. If the soil moisture reaches optimum with rainfall, maize is not irrigated.

F2.   Maize fields are irrigated only during dry periods, according to the authorization calendars. The choice of irrigation days is based on the farmer's experience, not on soil moisture measurements or weather forecasts.

F3.   The authorization to use irrigation channels lasts five months, from May 1st to September 30th. Irrigation water is provided to maize fields according to the real need for water, during dry periods.

F4.   The fields which are irrigated with the irrigation channels is very gravelly: irrigation is provided during dry periods but also when forecast services predict lacks of precipitation.

F5.   Irrigation is provided according to the authorization calendars, but only during dry periods.

Question 4.   *What is the mean frequency of irrigation?*

F1.   Usually between 4 and 6 irrigation events per growing season. The frequency is higher during dry periods. For example, 4 waterings were carried out in 2020 and 8 waterings in 2021 (very dry year). The necessity of irrigation is evaluated by the farmer, without field measures or meteorological forecasts.

F2.   The irrigation frequency is usually 9-10 days for an average year, starting from late June. Maize fields can be irrigated up to 7-8 times per growing season during dry years (like 2021), while 2-3 irrigation events are enough during wettest years (like 2019).

F3.   The average frequency is 4-5 times per growing season, usually from July. August and September are the months with the highest irrigation frequency.

F4.   Irrigation is provided about every 15 days starting from late June. Drop irrigation is provided with very high frequency (every 2-3 days).

F5. For maize is optimal an irrigation event every 15-20 days. For an average year, 3-4 waterings are optimal. During dry years, like 2021, maize requires more irrigation and up to 5-6 waterings can be provided.

Maize sowing periods and cultivation practices

Question 5. *In which period of the year is maize usually sown?*

F1. Usually, maize is sown twice per year. First sowing between the 1oth and 30th of April; second sowing occurs between the end of May and the first half of June. The choice of the sowing date depends mainly on soil moisture and weather conditions: soil temperature must be equal or above 13°C, and there must be low risk of late frost.

F2. Maize is usually sown during the second half of April, or between May 15th and the first week of June. The period depends on the final product to be obtained: chopped maize or dry grain. The choice of sowing day is mainly driven by meteorological factors and soil temperature.

F3. According to the soil moisture and weather conditions, maize is sown from the beginning of April. The provider of seeds ensures farmers against late frost: if the plant growth is blocked by late frosts in April, a new sowing can be done for free.

F4. If the soil moisture and weather conditions are optimal, sowing period starts during the second half of April.

F5. Two growing seasons are usually planned. The first starts in April (usually during the last two weeks) and the second starts in late May.

Question 6. *In which period of the year is maize usually harvested?*

F1. Usually between September and October (e.g., October in 2021). The harvesting period depends on the intended use of maize, for which grains must reach optimum levels of moisture. A moisture of 30% - 35% is required for chopped maize; a moisture of 25% is required for dry grain at the sowing date (after that, grains are left to dry up to 12%).

F2. Chopped maize is usually harvested around September 15th. Dry grain maize is usually harvested around the middle of October.

F3. The most important factor is the optimum moisture of maize grains. Usually, the maize growing season lasts 120-130.

F4. From the second half of September to late October, according to the required moisture of maize seeds and on weather conditions.

F5. Chopped maize is usually harvested at the beginning of September. The harvesting period for dry grain maize is usually October.

Question 7.   *How are corn fields used during rest periods? (e.g. fallow lands, other crops)*

F1. Fields are usually cultivated with fodder grasses or winter wheat from autumn to spring. Typically, the rotation scheme for these months is: 1 year of winter wheat and then 3 consecutive years of fodder grasses. Maize is not cultivated in summer after winter wheat, because wheat is harvested in July.

F2. The crop rotation involves fodder grasses and barley (all cultivated in summer). The scheme is 5-6 years of fodder grasses, 1-2 years of maize, 1-2 years of barley.

F3. Maize fields are usually lying fallow during winter.

F4. Croplands are located at high elevations, close to the Alps. Nothing is cultivated during winter.

F5. Crop rotation is a summer practice. During winter, croplands are harvested with fodder grasses.

Question 8.   *Approximately, how long do the plants take to reach the maximum stage of growth from seed?*

F1. The maximum growing stage is reached by maize in the second half of July for those years when seeds are sown around April 15th.

F2. Between June 20th and the first week of July, according on the date of sown.

F3. The maximum stage of growth is usually reached in the first two weeks of July.

F4. The maximum stage of growth is usually reached in the week of July.

F5. According to the maize variety, the maximum growing phase is reached in mid-July.

Appendix B. Survey among maize farmers in South Piedmont

115

References

1. The World Bank. Annual freshwater withdrawals, agriculture (% of total freshwater withdrawal). Available online: https://data.worldbank.org/indicator/er.h2o.fwag.zs. (accessed on: March, 16th 2022).

2. The World Bank. Water in Agriculture. Available online: https://www.worldbank.org/en/topic/water-in-agriculture. (accessed on: May, 8th 2020).

3. FAO, *The irrigation challenge: increasing irrigation contribution to food security through higher water productivity from canal irrigation systems* **2003**. IPTRID Issue Paper 4, IPTRID Secretariat, Food and Agricultural Organization of the United Nations, Rome.

4. United Nations, Department of Economic and Social Affairs. Food security and nutrition and sustainable agriculture: Sustainable Development Goals Available online: https://sdgs.un.org/topics/food-security-and-nutrition-and-sustainable-agriculture. (accessed on March, 31th 2022)

5. UN Environment Programme, GOAL 6: Clean water and sanitation. Available online: https://www.unep.org/explore-topics/sustainable-development-goals/why-do-sustainable-development-goals-matter/goal-6. (accessed on April 1st, 2022).

6. Brouwer, C.; Heibloem, *M.* Irrigation water management: training manual no. 3: irrigation water needs - Chapter 3, *FAO* **1985**, *Rome*. Available online: https://www.fao.org/3/s2022e/s2022e00.htm

7. Allen, R.G.; Pereira, L.S.; Raes, D.; Smith, M. Crop Evapotranspiration-Guidelines for computing crop water requirements-FAO Irrigation and drainage paper 56 FAO **1998**, *300(9)*, D05109, *Rome*.

8. AgMIP, Agricultural Model Intercomparison and Improvement Project. Available online: https://agmip.org/agmipcharter2/. (accessed on March, 1st 2022).

9. Joint Research Centre, EU Science Hub - Earth Observation. Available online: https://joint-research-centre.ec.europa.eu/scientific-activities-z/earth-observation_en (accessed on August, 2nd 2022).

10. Liu, P. *The future of Food and Agriculture: Trends and Challenges*, FAO: Annual Report 296 **2017**, pp. 1-180, *Rome*.

11. Doorenbos, J.; Kassam, A., Yield Response to Water, *FAO Irrigation and Drainage Paper n.33*, FAO **1979**, *Rome*.

12. Skoet, J.; Lipper, L., *The state of food and agriculture 2016*, FAO **2016**, *Rome*. Available online: https://www.fao.org/3/i6030e/i6030e.pdf

13. Massari, C.; Modanesi, S.; Dari, J.; Gruber, A. et al., A Review of Irrigation Information Retrievals from Space and Their Utility for Users, *Remote Sens.* **2021**, *13(20)*, p. 4112.

14. Dari, J.; Brocca, L.; Quintana-Seguì, P.; Casadei S. et al., Double-scale analysis on the detectability of irrigation signals from remote sensing soil moisture over an area with complex topography in central Italy, *Adv. Water Resour.* **2022**, *161*, 104130.

15. Bazzi, H.; Baghdadi, N.; Ienco, D.; El Hajj, M. et al., Mapping Irrigated Areas Using Sentinel-1 Time Series in Catalonia, Spain,» *Remote Sens.* **2019**, *11(15)*, p. 1836.

16. Gao, F.; Anderson, M.; Daughtry, C.; Karnieli, A. et al., A within-season approach for detecting early growth stages in corn and soybean using high temporal and spatial resolution imagery, *Remote Sens. Environ.* **2020**, *242*, 111752.

17. Ayari, E.; Kassouk, Z.; Lili-Chabaane, Z.; Baghdadi, N. et al. Cereal crops soil parameters retrieval using L-band ALOS-2 and C-band Sentinel-1 sensors *Remote Sens.* **2021**, *13(7)*, 1393.

18. Le Page, M.; Jarlan, L.; El Hajj, M.; Zribi, M. et al. Potential for the Detection of Irrigation Events on Maize Plots Using Sentinel-1 Soil Moisture Products *Remote Sens.* **2020**, *12(10)*, 1621.

19. Ayari, E.; Kassouk, Z.; Lili-Chabaane, Z.; Baghdadi, N. et al., Investigation of Multi-Frequency SAR Data to Retrieve the Soil Moisture within a Drip Irrigation Context Using Modified Water Cloud Model, *Sensors* **2022**, *22(2)*, p. 580.

20. International Society of Precision Agriculture, *Precision Ag Definition*. Available online: https://www.ispag.org/about/definition. (accessed on May, 5th 2022).

21. Khanal, S.; Kc, K., Fulton, J. et al., Remote Sensing in Agriculture—Accomplishments, Limitations, and Opportunities, *Remote Sens.* **2020**, *12(22)*, p. 3783.

22. World Meteorological Organization, *OSCAR: Observing Systems Capability Analysis and Review Tool*. Available online: https://space.oscar.wmo.int/. (accessed on March, 20th 2022).

23. Orynbaikyzy, A.; Gessner, U.; Conrad, C., Crop type classification using a combination of optical and radar remote sensing data: A review, *Int. J. Remote Sens.* **2019**, *40(17)*, pp. 6553-6595.

24. El Hajj, M.; Baghdadi, N.; Bazzi, H.; Zribi, M. Penetration analysis of SAR signals in the C and L bands for wheat, maize, and grasslands *Remote Sens.* **2019**, *11(1)*, 31.

25. Sun, Q.; Miao, C.; Duan, Q. et al., A Review of Global Precipitation Data Sets: Data Sources, Estimation, and Intercomparisons, *Reviews of Geophysics* **2018**, *56(1)*, pp. 79-107.

26. Brocca, L.; Hahn, P.; Ciabatta, S.; Massari, C. et al., SM2RAIN-ASCAT (2007-2018): global daily satellite rainfall from ASCAT soil moisture, *Earth Syst. Sci. Data* **2019**, *11(4)*, pp. 1583-1601.

27. Buchhorn, M.; Smets, B.; Bertels, L.; De Roo, B. et al., *Copernicus Global Land Service: Land Cover 100m: Version 3 Globe 2015-2019. Product User Manual*, Copernicus Global Land service **2020**, European Commission Joint Research Centre (JRC).

28. Rolle, M.; Tamea, S.; Claps, P., ERA5-based global assessment of irrigation requirement and validation, *PLOS ONE* **2021**, 16(4): e0250979.

29. Döll, P.; Siebert, S., Global modeling of irrigation water requirements, *Water Resour. Res.* **2002**, *38(4)*, pp. 8.1-8.10.

30. De Fraiture, C. Integrated water and food analysis at the global and basin level. An application of WATERSIM, *Water Resources Management* **2007**, *21(1)*, pp. 185-198.

31. Rost, S.; Gerten, D.; Bondeau, A.; Lutch, W.; et al. Agricultural green and blue water consumption and its influence on the global water system, *Water Resour. Res* **2008**, *44(9)*, W09405.

32. Hanasaki, N.; Kanae, S.; Oki, T.; Masuda, K. et al. An integrated model for the assessment of global water resources, *Hydrol. Earth Syst. Sci.* **2008**, *12(4)*, pp. 1007-1025.

33. Siebert, S.; Döll, P. Quantifying blue and green virtual water contents in global crop production, *Journal of Hydrology* **2010**, *384(3-4)*, pp. 198-217.

34. Liu, J.; Yang, H. Spatially explicit assessment of global consumptive water uses in cropland: Green and Blue water, *Journal of Hydrology* **2010**, *384(3-4)*, pp. 187-197.

35. Mekonnen, M.; Hoekstra, A. The green, blue and grey water footprint of crops and derived crop products, *Hydrol. Earth Syst. Sci.* **2011**, *15(5)*, pp. 1577-1600.

36. Chiarelli, D.; Passera, C.; Rosa, L.; Davis, K. et al. The green and blue crop water requirement WATNEEDS model and its globan gridded outputs, *Sci. Data* **2020** *7(1)*, 273.

37. Hargreaves, G.H.; Samani, Z.A. Reference Crop Evapotranspiration from Temperature, *Appl. Eng. Agric.* **1985**, *1(2)*, pp. 96-99.

38. Tuninetti, M.; Tamea, S.; D'Odorico, P.; Laio, F.; Ridolfi, L. Global sensitivity of high-resolution estimates of crop water footprint, *Water Resour. Res.* **2015**, *51(10)*, pp. 8257-8272.

39. Chapagain, A.; Hoekstra, A. Water footprints of nations - volume 2, Appendices, *Value of Water Research Report Series no. 16*, **2004**.

40. FAO, *GAEZ, Global Agro-Ecological Zones* **2003**. Available online: http://www.fao.org/nr/gaez. (accessed on February 2019).

41. Portmann, F.; Siebert, S.; Döll, P., MIRCA2000—Global monthly irrigated and rainfed crop areas around the year 2000: A new high-resolution data set for agricultural and hydrological modeling. *Glob. Biogeochem. Cycles* **2010**, *24*, 10.1029/2008GB003435.

42. Cancela, J.J.; González, X.P.; Vilanova, M.; Mirás-Avalos, J.M. Water management using drones and satellites in agriculture, *Water* **2019**, *11(5)*, p. 874.

43. Salmon, J.; Friedl, M.; Frolking, S.; Wisser, D.; Douglas, E. Global rain-fed, irrigated and paddy croplands: A new high resolution map derived from remote sensing, crop inventories and climate data, *Int. J. Appl. Earth Obs. Geoinf.* **2015**, *38*, pp. 321-334.

44. Brocca, L.; Tarpanelli, A.; Filippucci, P.; Dorigo, W.; et al. How much water is used for irrigation? A new approach exploiting coarse resolution satellite soil moisture products, *Int. J. Appl. Earth Obs. Geoinf.* **2018**, *73*, pp. 752-766.

45. ESA, *Observing the Earth: Copernicus* **2018**. Available online: http://www.esa.int/Applications/Observing_the_Earth/Copernicus/Overview4.

46. ECMWF, *Fact sheet: Reanalysis*. Available online: https://www.ecmwf.int/en/about/media-centre/focus/2020/fact-sheet-reanalysis. (accessed on August 2022).

47. Copernicus Climate Change Service (C3S), *ERA5: Fifth generation of ECMWF atmospheric reanalyses of the global climate*, **2017**. Available online: https://cds.climate.copernicus.eu/cdsapp#!/home. (accessed on April, 3rd 2022).

48. Hersbach, H.; Bell, B.; Berrisford, P.; Hirahara, S. et al. The ERA5 global reanalysis, *Q. J. R. Meteorol. Soc.* **2020**, *146(730)*, pp. 1999-2049.

49. Muñoz-Sabater, J.; Dutra, E.; Agustí-Panareda, A. et al., ERA5-Land: A state-of-the-art global reanalysis dataset for land applications, *Earth Syst. Sci. Data* **2021**, *13(9)*, pp. 4349-4383.

50. Boogaard, H.; Schubert, J.; De Wit, A.; Lazebnik, J. e et al. Agrometeorological indicators from 1979 to present derived from reanalysis, version 1.0. *Climate Data Store (CDS), Copernicus European Programme* **2020**. Available online:

https://cds.climate.copernicus.eu/cdsapp#!/dataset/10.24381/cds.6c68c9bb?tab=overview. (accessed on August 2022).

51. Harris, I.; Osborn, T.J.; Jones P.; Lister, D. Version 4 of the CRU TS monthly high-resolution gridded multivariate climate dataset, *Scientific data* **2020,** *7(1)*, p. 109.

52. Heydari, M.M.; Heydari, M. Calibration of Hargreaves-Samani equation for estimating reference evapotranspiration in semiarid and arid regions, *Archives of Agronomy and Soil Science* **2014**, *60(5)*, pp. 695-713.

53. Hargreaves, H. *Simplified Coefficients for Estimating Monthly Solar Radiation in North America and Europe*. Departmental Paper, Dept. of Biol And Irrig. Engrg., Utah State University, *Logan, Utah* **1994**.

54. Van Velthuizen, H.; Huddleston, B.; Fischer, G.; Salvatore, M. et al. *Mapping biophysicalfactors that influenceagricultural productionand rural vulnerability*, Food & Agriculture Org. No. 11., *FAO* **2007**, *Rome*.

55. Liu, J. A GIS-based tool for modelling large-scale crop-water relations, *Environmental Modelling & Software* **2009**, *24(3)*, pp. 411-422.

56. Ahooghalandari, M.; Kiadani, M.; Jahromi, M. Developing equations for estimating reference evapotranspiration in Australia, *Water Resour. Manag.* **2016**, *30(11)*, pp. 3815-3828.

57. European Centre for Medium-range Weather Forecasts (ECMWF). *Part IV: Physical Processes. IFS Documentation–Cy41r2* **2016**, pp. 1-213.

58. FAO/IIASA/ISRIC/ISSCAS/JRC, Harmonized World Soil Database (version 1.2), *Rome*, **2012**.

59. AQUASTAT: FAO's global informationsystem on water and agriculture, *FAO* **2012,** Rome.

60. Castejón-Porce, G.; Espín-Sánchez, D.; Ruiz-Álvarez, V. et al. Runoff Water as A Resource in the Campo de Cartagena (Region of Murcia): Current Possibilities for Use and Benefits, *Water* **2018**, *10(4)*, p. 456.

61. Stuntebeck, T.; Komiskey, M.; Peppler, M. et al. Precipitation-runoff relations and water-quality characteristics at edge-of-field stations, Discovery Farms and Pioneer Farm, Wisconsin, *U.S. Geological Survey Scientific Investigations Report* **2011**, *2003(8)*.

62. Hofste, R.; Kuzma, S.; Walker, S.; Sutanudjaja, E.; et al., *Aqueduct 3.0: updated decision-relevant global water risk indicators*, World Resources Institute, **2019**.

63. Organization for Economic Co-operation and Development (OECD), *Water withdrawals (indicator)*. Available online: https://data.oecd.org/water/water-withdrawals.htm. (accessed on April 2020).

64. McCarthy, M. Regulated deficit irrigation and partial rootzone drying as irrigation management techniques for grapevines, Deficit Irrigation Practices, Water Reports 22, *FAO* **2000**, Rome.

65. Siebert S.; Döll P. The Global Crop Water Model (GCWM): Documentation and first results for irrigated crops, *Frankfurt Hydrology paper* **2008**, *7*, pp. 1-42.

66. Hutson, S.S.; Barber, N.L.; Kenny, J.F.; Linsey, K.S. et al. Estimated use of water in the United States in 2000, U.S Geological Survey **2004**, *1268*.

67. California Department of Water Resources (CDWR), Agricultural Land & Water Use Estimates **2020**. Available online: https://water.ca.gov/Programs/Water-Use-And-Efficiency/Land-And-Water-Use/Agricultural-Land-And-Water-Use-Estimates. (accessed on October, 24th 2020).

68. Rolle, M.; Tamea, S.; Claps, P. Climate-driven trends in agricultural water requirement: an ERA5-based assessment at daily scale over 50 years *Environ. Res. Lett.* **2022**, *17(4)*, 044017.

69. Rosenzweig, C.; Elliott, J.; Deryng, D.; Ruane A. et al. Assessing agricultural risks of climate change in the 21st century in a global gridded crop model intercomparison, *Proc. Natl. Acad. Sci. USA* **2014**, *11(9)*, pp. 3268-3273.

70. Ruane, A.; Phillips, M.; Müller, C.; Elliott, J. et al., Strong regional influence of climatic forcing datasets on global crop model ensembles, *Agric. For. Meteorol.* **2021**, *300*, 108313.

71. Lin, Y.; Feng, X.; Fu, B.; Chen, Y.; et al. Irrigation water consumption of irrigated cropland and its dominant factor in China from 1982 to 2015, *Adv. Water Resour.* **2020**, *143*, 103661.

72. Hersbach, H.; Bell, B.; Berrisford, P.; Biavati, G. et al. ERA5 hourly data on single levels from 1979 to present, *Copernicus Climate Change Service (C3S) Climate Data Store (CDS)* **2018**.

73. Bell, B.; Hersbach, H.; Berrisford, P.; Dahlgren, P. et al. ERA5 hourly data on single levels from 1950 to 1978 (preliminary version), *Copernicus Climate Change Service (C3S) Climate Data Store (CDS)* **2020**.

74. European Centre for Medium-range Weather Forecasts (ECMWF), *Global reanalysis: goodbye ERA-Interim, hello ERA5* (newsletter) **2019**. Available online: https://www.ecmwf.int/en/newsletter/159/meteorology/global-reanalysis-goodbye-era-interim-hello-era5. (accessed on March 2021).

75. European Centre for Medium-range Weather Forecasts (ECMWF), ERA5 back extension 1950-1978 (preliminary version): large bias in surface analysis over Australia prior to 1970. Available online: https://confluence.ecmwf.int/display/CKB/ERA5+back+extension+1950-1978+%28Preliminary+version%29%3A+large+bias+in+surface+analysis+over+Australia+prior+to+1970. (accessed on May 2021)

76. Schulzweida, U. CDO User Guide (Version 1.9.8), Zenodo **2019**. Available online: http://doi.org/10.5281/zenodo.3539275.

77. Hegerl, G.; Black, E.; Allan, R.; Ingram, W.; et al. Challenges in Quantifying Changes in the Global Water Cycle, *Bulletin of the American Meteorological Society* **2015**, *96(7)*, pp. 1097–1115.

78. Hengl, T.; Mendes de Jesus, J.; Heuvelink, G.; Ruiperez Gonzalez, et al., SoilGrids250m: Global gridded soil information based on machine learning, *PLOS ONE* **2017**, *12(2)*, e0169748.

79. Raes, D.; Steduto, P.; Hsiao, T.; Fereres, E. Reference Manual, Chapter 3, *AquaCrop Version 4.0*, FAO Land and Water Division **2012**, p. 35., *Rome*.

80. Seneviratne, S.; Nicholls, N.; Easterling, D. et al. Changes in climate extremes and their impacts on the natural, *Cambridge University Press* **2012**, Cambridge, UK, & New York, NY, USA.

81. Rajah, K.; O'Leary, T.; Turner, A.; Petrakis, G. et al. Changes to the temporal distribution of daily precipitation, *Geophys. Res. Lett.* **2014**, *41(24)*, pp. 8887-8894.

82. Masson-Delmotte, V.; Zhai, P.; Pirani, A.; Connors L. et al. Climate Change 2021: The Physical Science Basis. Contribution of Working Group I to the Sixth Assessment Report of the Intergovernmental Panel on Climate Change, *Cambridge University Press*. **2021**, Cambridge (UK).

83. Rogers, S.; Chen, D.; Jiang, H.; et al. An integrated assessment of China's South–North Water Transfer Project, *Geographical Research* **2020**, *58(1)*, pp. 49-63.

84. Costa, M.; Fleck, L.; Cohn. A. et al. Climate risks to Amazon agriculture suggest a rationale to conserve local ecosystems, *Front. Ecol. Environ*. **2019**, *17(10)*, pp. 584-590.

85. Leite-Filho, A.; Soares-Filho, B.; Davis, J. et al. Deforestation reduces rainfall and agricultural revenues in the Brazilian Amazon, *Nat. Commun.* **2021**, *12(1)*, 2591.

86. Bandyopadhyay, A.; Bhadra, A.; Raghuwanshi, N.; Singh, R., Temporal Trends in estimates of Reference Evapotranspiration over India, *J. Hydrol. Eng.* **2009**, *14(5)*, pp. 508-515.

87. Antón, R.; Virto, I.; González, J.; Hernández, I.; Enrique, A. et al., Extension of irrigation in semi-arid regions: What challenges for soil security? Perspectives from a regional-scale project in Navarre (Spain), *Global Soil Security. Towards More Science-Society Interfaces*, DA Eds **2018**, pp. 79-87.

88. Sloat, L.; Davis, S.; Gerber, J. et al., Climate adaptation by crop migration, *Nat. Commun.* **2020**, *11(1)*, pp. 1-9.

89. Li, M.; Shi, M.; Zhang, J.; Qi, Y.; Lei, Y., Quantifying the Space-Time Variations of Water Demands for Major Crops in Hebei Province, China,» *Atmosphere* **2022**, *13(9)*, p. 1399.

90. Oumarou Abdoulaye, A.; Lu, H.; Zhu, Y. et al. The global trend of the net irrigation water requirement of maize from 1960 to 2050, *Climate* **2019**, *7(10)*, p. 124.

91. Environmental European Agency, *Crop water demand.* Available online: https://www.eea.europa.eu/data-and-maps/indicators/water-requirement-2/assessment/#_edn8. (accessed on September, 10th 2022).

92. Rolle, M.; Tamea, S., Claps, P.; Ayari, E.; Baghdadi, N.; Zribi, M., Analysis of Maize Sowing Periods and Cycle Phases Using Sentinel 1&2 Data Synergy, *Remote Sens.* **2022**, *14(15)*, p. 3712.

93. Pasquel, D.; Roux, S.; Richetti, J.; Cammarano, D; Tisseyre, B.; Taylor, J.A., A review of methods to evaluate crop model performance at multiple and changing spatial scales. *Precis. Agric.* **2022**, *23*, pp. 1489–1513.

94. Urban, D.; Guan, K.; Jain, M. Estimating sowing dates from satellite data over the US Midwest: A comparison of multiple sensors and metrics. *Remote Sens. Environ.* **2018**, *211*, 400–412.

95. Irwin, S.; Good, D.; Newton; Early, J., Planting and 2015 Corn Yield Prospects: How Much of an Increase? *Farmdoc Dly*. **2015**, *5*, 169-184.

96. Ortiz-Monasterio, R.; Dhillon, J.I.; Fisher, R.A., Date of sowing effects on grain yield and yield components of irrigated spring wheat cultivars and relationships with radiation and temperature in Ludhiana, India. *Field Crop. Res.* **1994**, *37*, pp. 169–184.

97. Howden, S.; Soussana, J.; Tubiello, F. Adapting agriculture to climate change. *Proc. Natl. Acad. Sci. USA* **2007**, *104*, pp. 19691–19696.

98. Dharmarathna, W.; Herath, S.; Weerakoon, S., Changing the planting date as a climate change adaptation strategy for rice production in Kurunegala district, Sri Lanka. *Sustain. Sci.* **2014**, *9*, pp. 103–111.

99. Alexandrov, V.; Eitzinger, J.; Cajic, J.; Oberforster, M., Potential impact of climate change on selected agricultural crops in north-eastern Austria. *Glob. Chang. Biol*. **2002**, *8*, pp. pp. 373–389.

100. Baldwin, B.; Cossar, R., Castor yield in response to planting date at four locations in the south-central United States. *Ind. Crops Prod*. **2009**, *29*, pp. pp. 316–319.

101. Shah, H.; Siderius, C.; Hellegers, P., Limitations to adjusting growing periods in different agroecological zones of Pakistan. *Agric. Syst.* **2021**, *192*, 103184.

102. Colliander, A.; Reichle, R.; Crow, W.; Cosh, M.H.; Chen, F.; Chan, S.; Das, N.N.; Bindlish, R.; Chaubell, J.; Kim, S.; et al., Validation of soil moisture data products from the NASA SMAP mission. *IEEE J. Sel. Top. Appl. Earth Obs. Remote Sens.* **2021**, *15*, pp. 364–392.

103. Weiss, M.; Jacob, F.; Duveiller, G., Remote sensing for agricultural applications: A meta-review. *Remote Sens. Environ.* **2020**, *236*, 111402.

104. Quaadi, N.; Jarlan, L.; Ezzahar, L.; Zribi, M.; Zribi, M.; Khabba, S.; Bouras, E.; Bousbih, S.; Frison, P.L., Monitoring of wheat crops using the backscattering coefficient and the interferometric coherence derived from Sentinel-1 in semi-arid areas. *Remote Sens. Environ.* **2020**, *251*, 112050.

105. Nasrallah, A.; Baghdadi, N.; El Hajj, M.; Darwish, T., Sentinel-1 Data for Winter Wheat Phenology Monitoring and Mapping. *Remote Sens*. **2019**, *11*, 2228.

106. Pascale, C.; Dubois, P.; Van Zyl, J.; Engman, T., Measuring soil moisture with imaging radars. *IEEE Trans. Geosci. Remote Sens.* **1995**, *33*, pp. 915–926.

107. Frenken, K.; Gillet, V. *Irrigation Water Requirement and Water Withdrawal by Country*; FAO: Rome, Italy, 2012.

108. Zhang, M.; Abrahao, G.; Cohn, A.; Campolo, J.; Thompson, S. A MODIS-based scalable remote sensing method to estimate sowing and harvest dates of soybean crops in Mato Grosso, Brazil. *Heliyon* **2021**, *7*, e07436.

109. Rezaei, E.; Ghazaryan, G.; González, J.; Cornish, N.; Dubovyk, O.; Siebert, S. The use of remote sensing to derive maize sowing dates for large-scale crop yield simulations. *Int. J. Biometeorol*. **2021**, *65*, pp. 565–576.

110. Lobell, D.; Sibley, A.; Ortiz-Monasterio, I.J. Extreme heat effects on wheat senescence in India. *Nat. Clim. Chang.* **2012**, *2*, pp. 186–189.

111. Bousbih, S.; Zribi, M.; Lili-Chabaane, Z.; Baghdadi, N.; El Hajj, M.; Gao, Q.; Mougenot, B. Potential of Sentinel-1 Radar Data for the Assessment of Soil and Cereal Cover Parameters. *Sensors* **2017**, *17*, pp. 2617.

112. Copernicus European Programme, Land Service. CORINE Land Cover: CLC_2018 v.2020_20u1. Available online: https://land.copernicus.eu/pan-european/corine-land-cover (accessed on 11 October 2021).

113. Regione Piemonte. GEO-Piemonte: Modello Digitale del Terreno da CTRN 1:10000 (Passo 10 m)—STORICO. Available online: https://www.geoportale.piemonte.it/geonetwork/srv/ita/catalog.search#/metadata/r_piemon:3 ffe6b7b-9abe-4459-8305-e444e8eb197c (accessed on 20 November 2021).

114. Braca, G.; Bussettini, M.; Lastoria, B.; Mariani, S.; Piva, F. Il bilancio idrologico GIS based a scala nazionale su griglia regolare—BIGBANG: Metodologia e stime. Rapporto sulla disponibilità naturale della risorsa idrica Rapp. *ISPRA* **2021**, *339*, pp. 1–181.

115. ISTAT. Agricultura. Available online: https://www.istat.it/it/agricoltura?dati (accessed on 25 November 2021).

116. ISTAT. 6° Censimento Agricoltura 2010: Data Warehouse. Available online: http://dati-censimentoagricoltura.istat.it/Index.aspx (accessed on 14 October 2021).

117. Regione Piemonte. Bonifica e Irrigazione (SIBI). Available online: https://www.regione.piemonte.it/web/temi/agricoltura/agroambiente-meteo-suoli/bonifica-irrigazione-sibi (accessed on November 13th 2021)

118. Regione Piemonte. Sistema Informativo Risorse Idriche (SIRI). Available online: http://www.regione.piemonte.it/siriw/cartografia/mappa.do;jsessionid=E4D50E350BDDEF87B8B00E2144523402.part212node11 (accessed on 13 November 2021).

119. ESA Sentinels. Sentinel-1, Level-1 GRD Products. Available online: https://sentinels.copernicus.eu/web/sentinel/technical-guides/sentinel-1-sar/products-algorithms/level-1-algorithms/ground-range-detected (accessed on 16 December 2021).

120. Gorelick, N.; Hancher, M.; Dixon, M.; Ilyushchenko, S.; Thau, D.; Moore, R. Google Earth Engine: Planetary-scale geospatial analysis for everyone. *Remote Sens. Environ.* **2017**, *202*, pp. 18–27.

121. Google Earth Engine. Sentinel-1 Algorithms, Google 2022. Available online: https://developers.google.com/earth-engine/guides/sentinel1 (accessed on 20 May 2022).

122. Engman, E. Applications of microwave remote sensing of soil moisture for water resources and agriculture. *Remote Sens. Environ*. **1991**, *35*, pp. 213–226.

123. Zribi, M.; Baghdadi, N.; Holah, N.; Fafin, O.; Guérin, C. Evaluation of a rough soil surface description with ASAR-ENVISAT radar data. *Remote Sens. Environ.* **2005**, *95(1)*, pp. 67-76.

124. Evans, D.; Farr, T.; Zyl, J. Estimates of surface roughness derived from synthetic aperture radar (SAR) data. *IEEE Trans. Geosci. Remote Sens.* **1992**, *30*, pp. 382–389.

125. Veloso, A.; Mermoz, S.; Bouvet, A.; Le Toan, T.; Planells, M.; Dejoux, J.F.; Ceschia, E. Understanding the temporal behavior of crops using Sentinel-1 and Sentinel-2-like data for agricultural applications. *Remote Sens. Environ.* **2017**, *199*, pp. 415–426.

126. Rouse, J.; Haas, R.; Schell, J.; Deering, D. *Monitoring the Vernal Advancement and Retrogradation (Green Wave Effect) of Natural Vegetation*; No. NASA-CR-132982; Texas A and M Univ., College Station. Remote Sensing Center: Texas, USA, **1973**.

127. Theia. Value-Adding Products and Algorithms for Land Surfaces. Available online: https://www.theia-land.fr/en/homepage-en/ (accessed on 1-15 November 2021).

128. El Hajj, M.; Baghdadi, N.; Zribi, M.; Bazzi, H. Synergic Use of Sentinel-1 and Sentinel-2 Images for Operational Soil Moisture Mapping at High Spatial Resolution over Agricultural Areas. *Remote Sens.* **2017**, *9*, 1292.

129. THISME. THeia and Irstea Soil MoisturE catalog. Available online: https://thisme.cines.teledetection.fr/home (accessed on 20-31 October 2021).

130. Regione Piemonte. GEO-Piemonte: Mosaicatura Catastale di Riferimento Regionale. Available online: https://www.geoportale.piemonte.it/cms/progetti/progetto-mosaicatura-catastale (accessed on 12 October 2021).

131. Regione Piemonte. Anagrafe Agricola Unica—Data Warehouse e Open Data. Available online: http://www.sistemapiemonte.it/fedwanau/elenco.jsp (accessed on 14 October 2021).

132. Regione Piemonte. Norme Tecniche di Produzione Integrata: Difesa, Diserbo e Pratiche Agronomiche **2018**. Available online: https://www.regione.piemonte.it/web/sites/default/files/media/documenti/2018-11/norme_tecniche_piemonte_2018.pdf (accessed on 5 February 2022).

133. Muth, L.; Diamond, D.; Lelis, J. *Uncertainty Analysis of Radar Cross Section Calibration at Etcheron Valley Range*; Technical Note (NIST TN) 1534; National Institute of Standards and Technology: Gaithersburg, MD, USA, **2004**.

134. Swan, J.B.; Schneider, E.C.; Moncrief, J.F.; Paulson, W.H.; Peterson, A.E. Estimating corn growth, yield, and grain moisture from air growing degree days and residue cover. *Agron. J.* **1987**, *79*, pp. 53–60.

135. Darby, H.; Lauer, J. Plant Physiology: Critical Stages in the Life of a Corn Plant. *Tech. Rep.* **2004**. Available online: http://corn.agronomy.wisc.edu/Management/pdfs/CriticalStages.pdf (accessed on 17 February 2022).

136. Abendroth, L.J.; Elmore, R.W.; Boyer, M.J.; Marlay, S.K. *Corn Growth and Development*, 1st ed.; Iowa State University, University Extension: Ames, IA, USA, **2011**.

137. Berti, A.; Maucieri, C.; Bonamano, A.; Borin, M. Short-term climate change effects on maize phenological phases in northeast Italy. *Italy J. Agron.* **2019**, *14*, pp. 222–229.

138. Corn Agronomy. Corn Development. Available online: http://corn.agronomy.wisc.edu/Management/L011.aspx (accessed on 25 February 2022).

139. Arpa Piemonte. Annali Meteorologici ed Idrologici. Available online: https://www.arpa.piemonte.it/rischinaturali/accesso-ai-dati/annali_meteoidrologici/annali-meteo-idro/annali-meteorologici-ed-idrologici.html (accessed on 21 February 2022).

140. Schneider, E.C.; Gupta, S.C. Corn emergence as influenced by soil temperature, matric potential, and aggregate size distribution. *Soil Sci. Soc. Am. J.* **1985**, *49*, pp. 415–422.

141. Evans, J. *Straightforward Statistics for the Behavioral Sciences*, 1st ed.; Thomson Brooks/Cole Publishing Co: Belmont, CA, USA, **1996**.

142. Azar, R.; Villa, P.; Stroppiana, D.; Crema, A.; Boschetti, M.; Brivio, P.A. Assessing in-season crop classification performance using satellite data: A test case in Northern Italy. *Eur. J. Remote Sens.* **2016**, *49*, pp. 361–380.

143. U.S. Department of Agriculture, Foreign Agricultural Service. IPAD Crop Calendars. Available online: https://ipad.fas.usda.gov/ogamaps/cropcalendar.aspx (accessed on 2 March 2022).

144. Siebert, S.; Kummu, M.; Porkka, M.; Döll, P. et al., A global data set of the extent of irrigated land from 1900 to 2005. *Hydrology and Earth System Sciences* **2015**, *19(3)*, pp. 1521-1545.

145. Lu, M.; Wu, M.; You, L. A cultivated planet in 2010–Part 1: The global synergy cropland map. *Earth Syst. Sci. Data* **2020**, *12(3)*, pp. 1913-1928.

146. Yu, Q.; You, L.; Wood-Sichra U. et al., A cultivated planet in 2010–Part 2: the global gridded agricultural-production maps, *Earth Syst. Sci. Data* **2015**, *12(4)*, pp. 3545-3572.

147. D. Grogan, S. Frolking, D. Wisser e et al., Global gridded crop harvested area, production, yield, and monthly physical area data circa 2015, *Sci. Data* **2022**, *9(1)*, pp. 1-16.

148. Singer, M.; Asfaw, D.; Rosolem R. et al., Hourly potential evapotranspiration at 0.1° resolution for the global land surface from 1981-present, *Sci. Data* **2020**, *8(1)*, pp.1-13.